UNIVERSIDAD DE CHILE
FACULTAD DE CIENCIAS FÍSICAS Y MATEMÁTICAS
DEPARTAMENTO DE ASTRONOMÍA

STUDYING THE MULTI-SCALE GAS DYNAMICS OF DISK GALAXIES THROUGH NUMERICAL SIMULATIONS

TESIS PARA OPTAR AL GRADO DE DOCTOR EN CIENCIAS, MENCIÓN ASTRONOMÍA

JOSÉ MAURICIO UTRERAS CONTRERAS

PROFESOR GUÍA:
DR. ANDRÉS FELIPE ESCALA ASTORQUIZA

MIEMBROS DE LA COMISIÓN:
DR. GUILLERMO ALBERTO NEVILLE BLANC MENDIBERRI
DR. GUIDO ALEJANDRO GARAY BRIGNARDELLO
DR. ERIC LOUIS JOSEPH EMSELLEM
DR. RICARDO RODRIGO MUÑOZ VIDAL

SANTIAGO DE CHILE
2020

Resumen

En los discos galácticos, la rotación galáctica establece el movimiento global del gas, su energía y su momentum pueden transferirse hacia las escalas espaciales de las nubes moleculares. Además, en el medio interestelar, los movimientos aleatorios y no circulares surgen de la inyección de energía producto de la formación estelar, interacciones entre nubes, inestabilidades gravitacionales y termales, entre otros procesos. En esta tesis, nuestro objetivo es comprender hasta qué punto la dinámica del gas a pequeña escala se ve afectada por los movimientos a gran escala de la galaxia. Abordamos esta pregunta utilizando una cantidad inexplorada de mecánica de fluidos: la circulación de un fluido Γ, una medida macroscópica de rotación local, definida como la integral de línea del campo de velocidad alrededor de una trayectoria cerrada. Estudiamos cómo las contribuciones relativas de la rotación galáctica y los movimientos locales no circulares a la circulación del gas cambian en función de la escala. Como laboratorio de pruebas de nuestra técnica, utilizamos simulaciones numéricas de discos galácticos utilizando el código de refinamiento de malla adaptativa Enzo, junto con recetas de formación estelar y su inyección energética. Medimos la distribución de circulación a diferentes escalas para el conjunto de galaxias tipo disco simuladas. Modelamos el campo de velocidad del disco galáctico como la suma de la rotación galáctica y un campo aleatorio Gaussiano. Las distribuciones de Γ provenientes de la rotación galáctica y un campo aleatorio gaussiano tienen comportamientos diferentes a través de escalas espaciales. El campo aleatorio Gaussiano está parametrizado por una ley de potencia quebrada en el espacio de Fourier, con una transición en la escala λ_c, similar a la forma del espectro de potencia de energía para fluidos bidimensionales. Definimos la escala espacial λ_{eq} como la escala donde la rotación galáctica y los movimientos no circulares contribuyen igualmente a Γ. Para nuestras galaxias simuladas, la dinámica de los gases a escala de nubes moleculares suele estar dominada por movimientos no circulares, pero en el centro de los discos galácticos la rotación galáctica sigue siendo relevante. Nuestro modelo muestra que la transferencia de rotación desde grandes escalas se rompe en la escala λ_c y esta transición es necesaria para reproducir la distribución de circulación. Encontramos que λ_{eq}, y por lo tanto la estructura del campo de velocidad del gas, se establece por las condiciones locales de estabilidad gravitacional e inyección de energía producto de la formación estelar.

Abstract

In galactic disks, galactic rotation sets the bulk motion of gas, and its energy and momentum can be transferred towards the scales of molecular clouds. Additionally, in the interstellar medium, random and non-circular motions arise from stellar feedback, cloud-cloud interactions, instabilities, among other processes. In this thesis, our aim is to comprehend to which extent small scale gas dynamics is affected from the large scale motions of the galaxy. We approach this question using an unexplored quantity of fluid mechanics: the fluid circulation Γ, a macroscopic measure of local rotation, defined as line integral of velocity field around a closed path. We study how the relative contributions of galactic rotation and local non-circular motions to the circulation of gas change as a function of scale. As a test-bed of our technique we use numercial simulations of galactic disks using the Adaptive Mesh Refinement code Enzo, coupled with recipes of star formation and stellar feedback. We measure the circulation distribution at different scales for the set of simulated disk galaxies. We model the velocity field of the galactic disk as the sum of galactic rotation and a Gaussian random field. The distributions of Γ coming from galactic rotation and a Gaussian random field have different behaviors across spatial scales. The Gaussian random field is parametrized by a broken power law in Fourier space with a break at the scale λ_c, similar to the shape of energy power spectrum for two-dimensional fluids. We define the spatial scale λ_{eq} as the scale where galactic rotation and non-circular motions contribute equally to Γ. For our simulated galaxies, the gas dynamics at the scale of molecular clouds is usually dominated by non-circular motions, but in the center of galactic disks galactic rotation is still relevant. Our model shows that the transfer of rotation from large scales breaks at the scale λ_c and this transition is necessary to reproduce the circulation distribution. We find that λ_{eq}, and therefore the structure of the gas velocity field, is set by the local conditions of gravitational stability and stellar feedback.

Agradecimientos

Primero, quiero agradecer a mi familia, las personas más importantes para mi y que siempre confiaron que podría lograr lo que sea. Cuando perdía la motivación o no sentía que esto terminaría me acordaba de ustedes y volvía a tener energías para finalizar esta etapa. Agradezco sobretodo a mi mamá que ha creído en mi desde que era muy pequeño. Lo único que me importa es que estén orgullosos de mi y espero nunca defraudarlos.

Quiero agradecer también a Alexander, Nicole y Natalia, mis más queridos amigos, a quienes solía visitar frecuentemente y olvidaba el estrés del doctorado. Además siempre había algo interesante de que conversar y fueron quienes me enseñaron a amar a los gatos. Por sobretodo, siempre demostraban creer mucho en mí, más que yo de lo que era capaz.

Finalmente quiero agradecer a todas las personas que conocí en Calán, especialmente a las personas que conocí en la oficina y con quienes compartimos años de discusiones, risas, juegos y chismes de todo tipo: Elise, Coni, Matías, Pola, Paula, Vachail, Priyanjali y en especial la Mari. Todos ustedes hacían que hubiese una buena razón para ir a Calán además que siento que me hicieron mejorar como persona. También quiero agradecer a los chicos del laboratorio con quienes compartí mucho el último tiempo que estuve en Calán, Lander, Cata, Franco, Camilo, David, Pablo y Rocío quien me apoyo mucho en los momentos más complicados. A Ricardo Muñoz por esas esporádicas conversaciones en los pasillos y que me hacía sentir como un colega más. También a David Azócar por su apoyo dentro y fuera de Calán. A Marta por esas conversaciones cada vez que iba a su oficina a pedirle algo o cuando iba a dejar quequitos. Finalmente a Andrés Escala y a Guillermo Blanc que tuvieron que lidiar conmigo por mucho tiempo. Siento que no pude aprender todo lo que pude de ustedes pero siempre sentí que confiaban mucho en lo que era capaz de hacer. Agradezco mucho a Andrés por preocuparse y motivarme a finalizar lo que he empezado.

Table of Contents

List of Tables

List of Figures

Chapter 1

Introduction

The structure of the gas velocity field is crucial for understanding how galaxies and molecular clouds evolve. For example, the dynamical state of gas is one of the key elements in star formation theories, e.g. invoking turbulence at the scale of molecular clouds (Padoan et al. 2012; Semenov et al. 2016), or galactic rotation as a particular parameter controlling star formation at galactic scales (Elmegreen 1997; Silk 1997; Kennicutt 1998; Tan 2000; Krumholz et al. 2012; Utreras et al. 2016; Jeffreson & Kruijssen 2018; Meidt et al. 2018). The common picture of star formation involves self-gravity and sources of energy acting against self-gravity. Galactic rotation is one of those energy sources, acting at the largest spatial scales, where ordered motions make up the bulk of the kinetic energy. However, while its importance is evident on large scales, it is not clear down to which spatial scales galactic rotation remains dynamically relevant. At the scales of molecular clouds or stellar cores, gas can be dynamically less coupled with galactic rotation and local non-circular motions start to dominate.

1.1. Star formation

In the study of star formation in galaxies, a substantial amount of work has focused on the role of galactic rotation and the velocity dispersion of gas. These two physical quantities control the stability of gas. Galactic rotation works at galactic scales, and its influence is often parameterized by the Toomre parameter Q (Toomre 1963). The classical form of this parameter involves the stability of a razor-thin disk of gas with

$$Q = \frac{\kappa c_s}{\pi G \Sigma_{\rm gas}}, \tag{1.1}$$

where c_s is the gas sound speed, κ is the epicyclic frequency given by $\kappa^2 = 4\Omega^2\left(1 + \frac{1}{2}\frac{\partial \ln \Omega}{\partial \ln R}\right)$, $\Sigma_{\rm gas}$ is the gas surface density, and G is the gravitational constant. This ideal case illustrates how galactic rotation delivers support against collapse, in particular to perturbations of size $\lambda > \lambda_{\rm rot} \equiv 4\pi^2 G \Sigma_{\rm gas}/\kappa^2$, setting a maximum size of collapsing fragments (Escala & Larson 2008). Following this line of thought, it is natural to expect that galactic rotation might reduce the level of star formation in disk galaxies. In particular, Utreras et al. (2016) showed that at galactic scales, the efficiency of star formation $\epsilon_{\rm SF}$, for simulated galactic disks, appears to be proportional to $\exp(-t_{\rm ff}/t_{\rm orb})$, where $t_{\rm ff}$ is the initial free-fall time, and $t_{\rm orb} = 2\pi/\Omega$ is the orbital time. This is shown in the top left panel of Figure 1.1. This expression is similar to the result of Li et al. (2005), where $\epsilon_{\rm SF} \propto \exp(-4.2Q)$. We show this result in the top right panel of Figure 1.1. However, other studies suggest that galactic rotation can increase the rate of star formation (Tasker & Tan 2009; Krumholz et al. 2012). On the other hand, velocity dispersion or turbulence, σ_v, is thought to act at galactic scales, through the modification of the Toomre parameter by $Q = \frac{\kappa \sigma_v}{\pi G \Sigma_{\rm gas}}$, or through the virial parameter, $\alpha_{\rm vir}$, at the scale of molecular clouds. The virial parameter measures the balance between gravitational potential energy W and kinetic energy K, and it is given by $\alpha_{\rm vir} = 2K/W$. In simulations of turbulent molecular clouds, Padoan et al. (2012) found that the efficiency of star formation is proportional to $\exp(-t_{\rm ff}/t_{\rm cr})$, where $t_{\rm cr}$ is the cloud crossing time, and $t_{\rm ff}/t_{\rm cr} \propto \alpha_{\rm vir}$. This anti-correlation between $\alpha_{\rm vir}$ and $\epsilon_{\rm ff}$ has been observed in M51 (Leroy et al. 2017) and in low-pressure atomic-dominated regions in nearby galaxies (Schruba et al. 2019). We display the result from Padoan et al. (2012) in Figure 1.1. If we change $t_{\rm cr}$ by $t_{\rm orb}$, or $\alpha_{\rm vir}$ by Q, this efficiency has a similar functional form compared to the results of Utreras et al. (2016) and Li et al. (2005). At different scales, different physical parameters control gas dynamics, and their functional forms are expected to be dimensionless combinations of such parameters (Escala 2015).

At galactic scales, for thin galactic disks, typical circular velocities, $v_{\rm rot}$, are larger than the velocity dispersion of clouds. In this regime, the motion of gas is dominated by rotation and its stability is given by Q. Then, we expect that other dimensionless quantities such as $\epsilon_{\rm SF}$ must be functions of Q and Ωt^*, where t^* is a characteristic timescale, such as the free-fall time. At the scales of clouds, gas dynamics is less coupled to galactic rotation and the relevant parameters are self-gravity and kinetic energy. It is then expected to find that $\alpha_{\rm vir}$ must play a role at these scales.

In summary, star formation shows that there are two distinct regimes for gas dynamics, one dominated by large scale galactic motions and other ruled by the non-ordered motions at the size of molecular clouds. However, there is no clear boundary between these two regimes. At intermediate scales both rotation and turbulence must be equally relevant setting the evolution of gas dynamics. Moreover, we do not know whether rotation can still influence the motion of clouds of gas, and if so, how this changes across a galaxy.

1.2. Rotation in clouds

At the scale of molecular clouds, a significant body of observational and theoretical research has been devoted to study the balance between gravitational potential energy W and kinetic energy K, commonly described by the virial parameter $\alpha_{\rm vir} = 2K/W$ (Padoan et al. 2017; Leroy et al. 2017; Sun et al. 2018). CO measurements in the PHANGS-ALMA survey made by Sun et al. (2018) show that $\alpha_{\rm vir}$ varies weakly from cloud to cloud, with $\alpha_{\rm vir} \sim 1.5 - 3.0$, expected values for marginally bound clouds or free-falling gas. A common assumption is that at the scale of molecular clouds, most of the kinetic energy K comes from

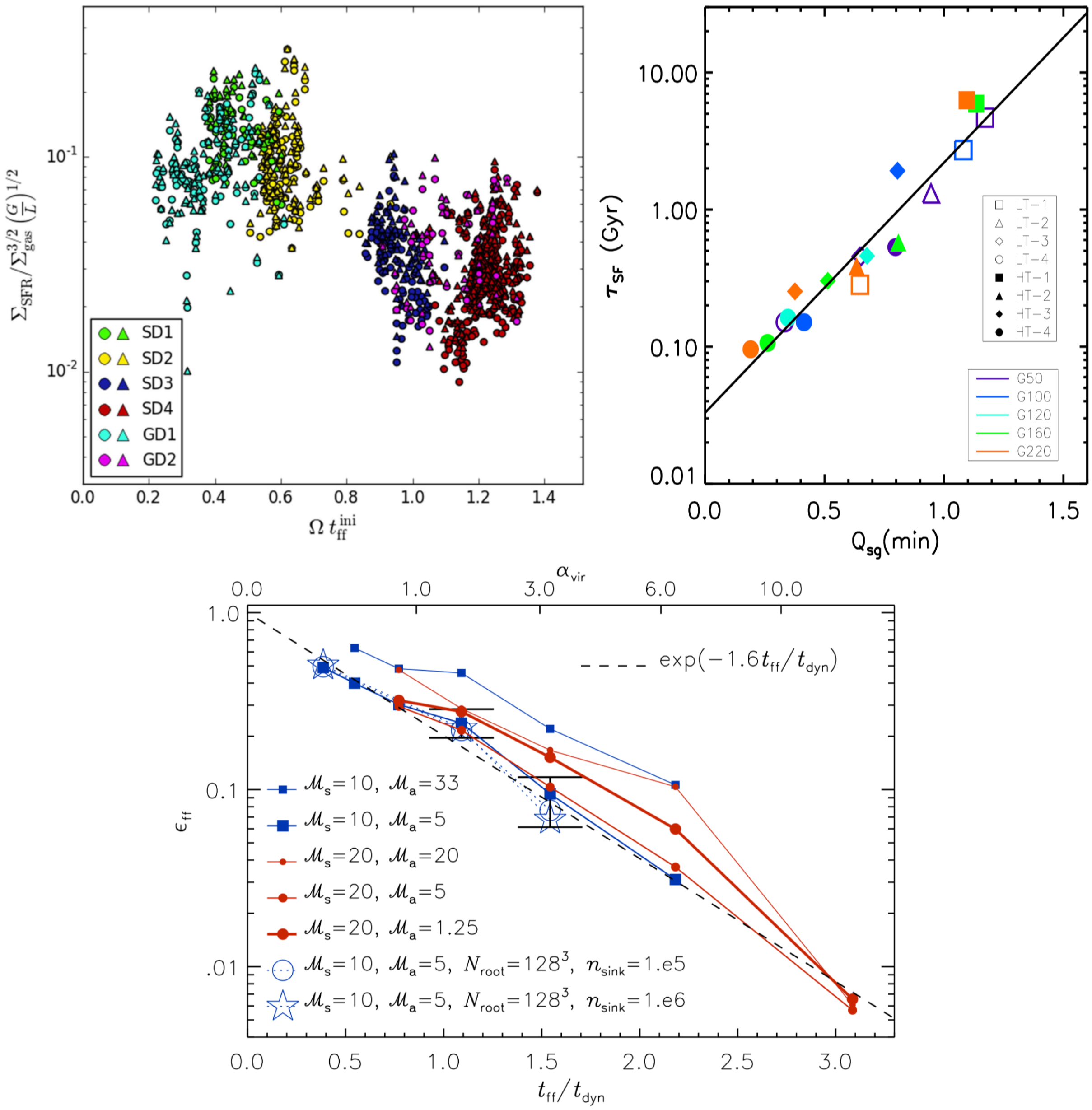

Figure 1.1: Star formation efficiency versus dimensionless parameters. *Top Left:* Star formation efficiency per free-fall time as a function of Ω times the initial free-fall time $t_{\rm ff}$ (Utreras et al. 2016). *Top Right:* Star formation timescale $\tau_{\rm SF}$ as a function of initial $Q_{\rm sg}$(min) (Li et al. 2005). *Bottom:* Efficiency per free-fall time as a function of $t_{\rm ff}/t_{\rm dyn}$, where $t_{\rm dyn}$ is the turbulent crossing time in a turbulent medium (Padoan et al. 2012).

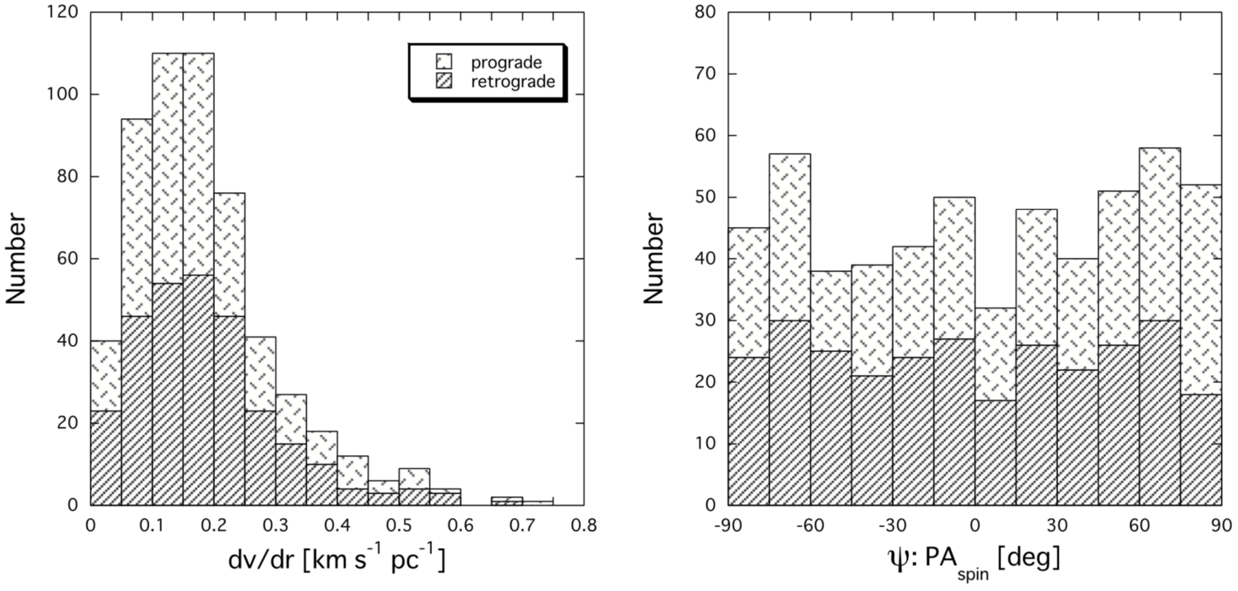

Figure 1.2: Distribution of velocity gradients (left) and position angles of spin (right) of Milky Way molecular clouds relative to the Galactic plane (Koda et al. 2006). The direction perpendicular to the Galactic Plane is $\psi = 0°$. Prograde and retrograde spins are indicated with different patterns.

non-circular turbulent motions. This assumption is supported by measurements of velocity gradients of molecular clouds in nearby galaxies. Studying our galaxy, Koda et al. (2006) estimated that the fractions of clouds with prograde or retrograde rotation with respect to the Galaxy's spin are similar. We show the distribution of velocity gradients and spin orientations found by Koda et al. (2006) in Figure 1.2. Another studied galaxy in this subject is M33. By measuring velocity gradients, Rosolowsky et al. (2003) found that, if clouds do rotate, nearly 40 % of them are counter-rotating with respect to their<galaxy. Additionally, they found that within a scale of approximately 500 pc, the spin of molecular clouds is more aligned with respect to other clouds in that region, as shown in Figure 1.3. This shows that there is a type of substructure of 500 pc in the gas velocity field.

More recently, Braine et al. (2018) confirmed that in M33 molecular clouds rotate, and that their rotation is too low to play a role in the gravitational stability of these objects. We show the distributions of velocity gradients and specific angular momentum from Braine et al. (2018) in Figure 1.4. The distribution of angular momentum in M33 is almost centered at zero with a small tendency to negative values (prograde rotation). This shows that the orientation of galactic rotation has a small effect on the rotation of molecular clouds in M33. On the other hand, these clouds have local angular velocities similar to the galactic angular speed.

These observed distributions are expected for clouds dominated by non-circular motions which have randomly aligned spins. In the field of simulations, Tasker & Tan (2009) found about 30 % of clouds with retrograde rotation in a simulated Milky Way like galaxy, even

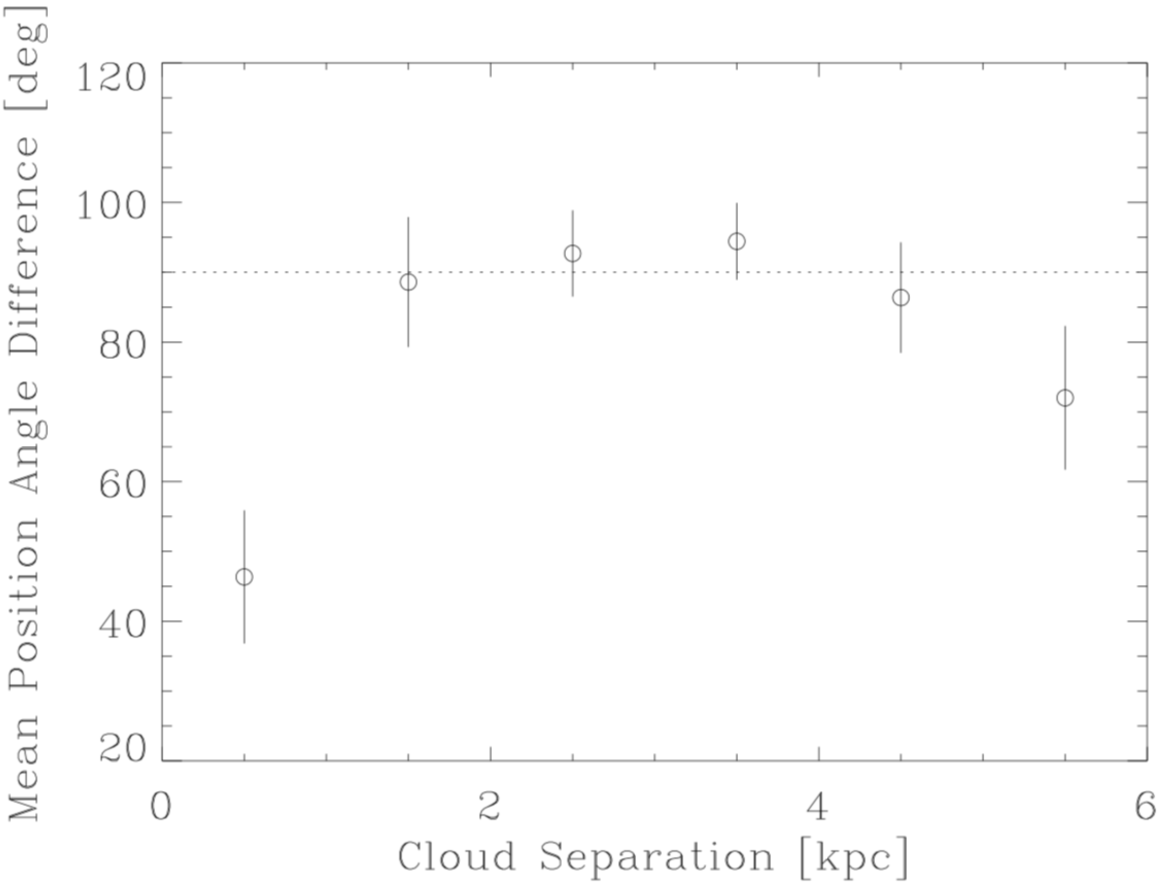

Figure 1.3: Correlation between the position of molecular clouds and their separation Rosolowsky et al. (2003). There is a trend that clouds at small distances tend to ave their velocit gradients aligned with each other. The mean in each bin is weighted according to the uncertainty in the measurements and the error bars the error in the mean.

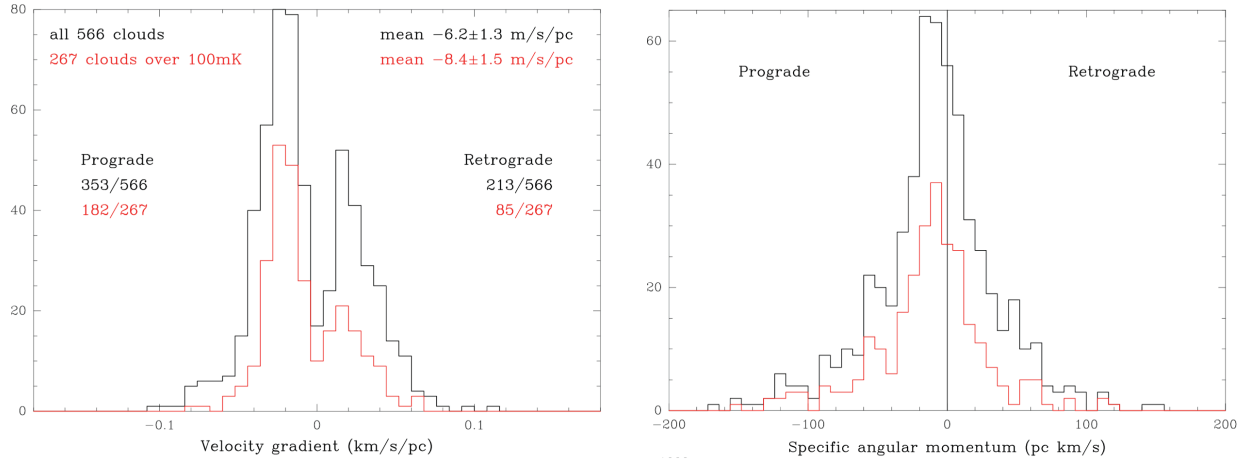

Figure 1.4: *Left:* Histogram of cloud velocity gradients for the entire sample in black and for only the brighter clouds in CO in red, from (Braine et al. 2018). Prograde rotation is given a negative sign here because the galaxy rotation velocity increases with decreasing declination. *Right:* Specific angular momenta of the M33 clouds. Red lines indicate data for CO-strong clouds.

in the absence of stellar feedback. Figure 1.5 shows the distributions of the angle between cloud angular momentum vectors and the galactic rotation axis. The top panel shows how the distribution changes during the course of the simulation, getting more random at later times. The bottom panel shows that after 140 Myr the simulated disk reaches a quasi-steady state and clouds have similar distributions in their spin independently of their age. Tasker & Tan (2009) argued that as time progresses, cloud-cloud interactions inject turbulence at the scale of these interactions. At later times, new clouds are born in a more disordered velocity field. However, non-ordered or non-circular motions are also originated by gravitational instabilities, torques from non-axisymmetric potentials, gas accretion, and stellar feedback (Goldbaum et al. 2015; Krumholz et al. 2018). These energy sources inject turbulence and induce non-circular motions that cascade towards small and large scales (Kraichnan 1967; Bournaud et al. 2010).

Ward et al. (2016) run a simulation similar to the work of Tasker & Tan (2009). However, they found a small fraction of retrograde clouds, only a 13 %. This discrepancy might be originated from the fact that the simulation of Ward et al. (2016) is more gravitational stable, injecting less turbulence.

1.3. Rotation versus Velocity dispersion

Observations (Larson 1981; Heyer et al. 2009; Shetty et al. 2012), and simulations of turbulent ISM (Kritsuk et al. 2013) show that the velocity dispersion of gas, σ_v, is strongly correlated with the scale ℓ. This correlation, $\sigma_v(\ell) \propto \ell^b$, is one of the so called Larson relations, which usually varies between $b \in [0.2, 1.1]$ (Shetty et al. 2012), while turbulent models show

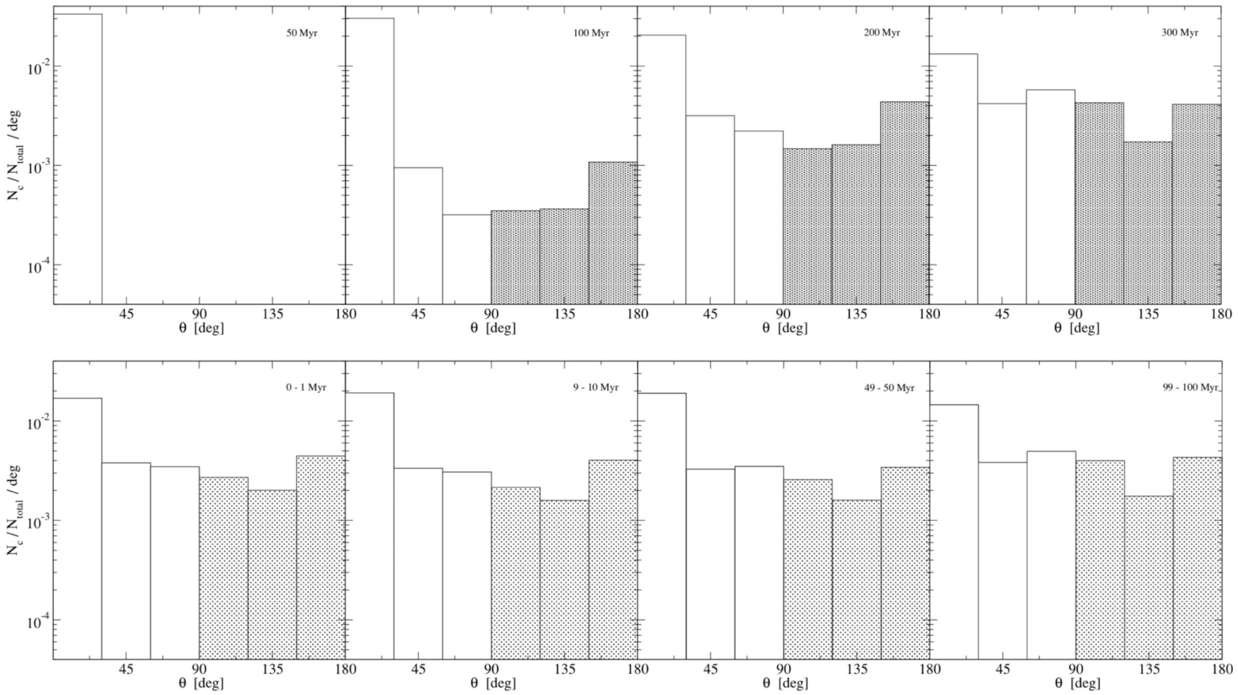

Figure 1.5: *Top* :Distribution of the angle, θ, between cloud angular momentum vectors and the galactic rotation axis at different times during the course of the simulation. The shaded bars indicated retrograde rotation, and this population grows with time as more and more clouds experience collisions and close interactions. *Bottom:* θ for clouds born after t = 140 Myr in the fully fragmented stage of evolution. The shaded bars indicated retrograde rotation. The fraction of retrograde clouds is about 25 % of the total and nearly independent of cloud age. Figures from Tasker & Tan (2009).

$b = 0.5$ (Kritsuk et al. 2013). On the other hand, we expect that galactic rotation drives velocity dispersions of the order of $\sigma_v^{\rm rot} \approx \Omega\ell$ before gas starts to collapse. In short, we have to different types of velocity fields with $\sigma_v \propto \ell^b$ with $b \lesssim 1$ and $\sigma_v^{\rm rot} \propto \ell$. We expect that at some particular scale ℓ^*, $\sigma_v(\ell^*) \approx \sigma_v^{\rm rot}(\ell^*)$.

This last point is similar to the discussion in Meidt et al. (2018) which compares motions induced by the gravitational potential of the galaxy and the velocity dispersion of gas. Meidt et al. (2018) calculate that for a spatial scale R_c

$$\begin{aligned} 3\sigma_{\rm gal,iso}^2 &= 3(\kappa R_c)^2, \\ 3\sigma_{\rm gal}^2 &= 2(\kappa R_c)^2 + (\nu R_c)^2, \end{aligned}$$

where, the subscript iso indicates if motions are isotropic, κ is the epicyclic frequency and ν the vertical frequency about the galactic plane. Meidt et al. (2018) present the hypothesis that the observed velocity dispersion of gas clouds, σ_v, is a combination of motions induced by self-gravity, $\sigma_{\rm sg}$ and the potential through the epicyclic frequency, $\sigma_v^2 = \sigma_{\rm sg}^2 + \kappa R_c^2$. Furthermore, they argue that clouds in nearby galaxies show signatures of motion driven by the galactic potential. Under these assumptions, if $R_c > \sigma_v/\kappa$, where σ_v is the velocity dispersion of gas, the Coriolis force is still relevant in the dynamics of molecular clouds.

This work shows that there may be a transition scale between large scale motions, or motions driven by the large scale galactic potential, and cloud scale turbulence, which in part could be also generated by torques exerted by the gravitational potential. Since κ and σ_v vary with galactocentric radius, we might expect that this transition scale changes across a galaxy. For example, at the center of galaxies we expect that galactic rotation has a high influence on the dynamics of clouds. Simulations of the Galactic Center (Kruijssen et al. 2019) show that molecular clouds are dominated by strong shear and tidal deformations. Moreover, shear motions from galactic rotation might set the cloud lifetimes in certain conditions (Jeffreson & Kruijssen 2018).

1.4. Vorticity and power spectrum

One way to estimate the role of galactic rotation is to measure its impact in the local rotation of gas, i.e. the rotation measured with respect to an inertial reference frame. Local rotation is defined by the vorticity vector $\vec{\omega} = \nabla \times \vec{v}$, which is extensively studied in the field of fluid mechanics (Ruppert-Felsot et al. 2005; Musacchio & Boffetta 2017; Couston et al. 2019). Vorticity has an important role in the dynamics of two-dimensional fluids, which is relevant since we may think of disk galaxies as quasi-two dimensional fluids. In two-dimensions, the evolution of the vorticity field is given by:

$$\frac{\partial \omega}{\partial t} + (\vec{v} \cdot \nabla)\omega = \nu \nabla^2 \omega + \nabla \vec{f}, \tag{1.2}$$

where ν is the viscosity and $\vec{f}$ is the eternal force applied on the fluid. For inviscid fluids with $\vec{f} = -\nabla\phi$, the equation is reduced to $\frac{D\omega}{Dt} = 0$, i.e. fluid cells conserve their vorticity. In this

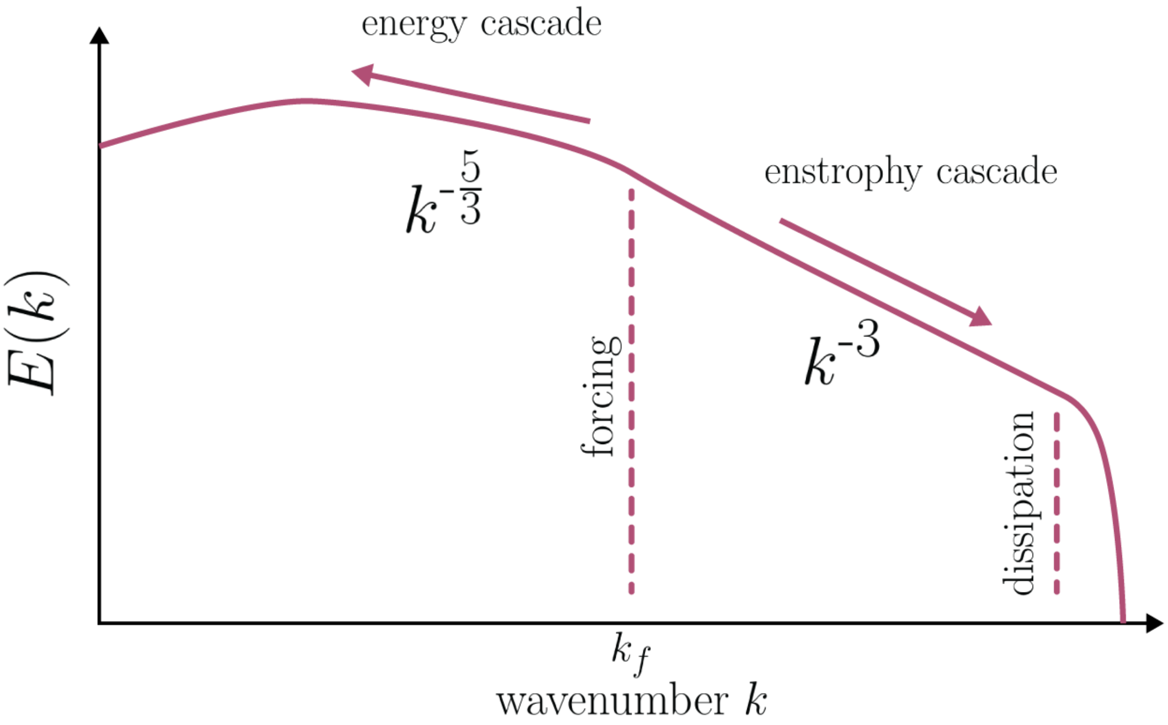

Figure 1.6: Illustration of two-dimensional power spectrum.

scenario, two conserved quantities appear, energy and enstrophy:

$$E = \frac{1}{2}\int_{\mathcal{D}} \vec{v}^2 \mathrm{d}A \ ; \ Z = \frac{1}{2}\int_{\mathcal{D}} \omega^2 \mathrm{d}A. \tag{1.3}$$

Kraichnan (1967) showed that these two invariant quantities give rise to a double cascade in the kinetic energy spectrum $E(k)$. The theory predicts an inverse energy cascade $E(k) \propto k^{-5/3}$ where kinetic energy is transferred to large scales, and a direct enstrophy cascade with $E(k) \propto k^{-3}$. In the presence of a forcing $\vec{f}$, the inverse cascade occurs in $k < k_f$ where k_f is the wavenumber of the forcing scale. The direct cascade transfers enstrophy from k_f to $k > k_f$.

In particular, for two dimensional fluids, we can find long-lived vortex structures in the vorticity field, usually called coherent structures. These substructures might be the origin of the correlations in the spin of neighbor clouds (Rosolowsky 2005). Moreover, these structures are related with the forcing scale in two dimensional fluids. The size of coherent structures is of the order of the forcing scale $\ell_f = 1/k_f$ (Paret & Tabeling 1998; Musacchio & Boffetta 2017). We show an example of these structures in Figure 1.7 that corresponds to a snapshot of a rotating turbulent flow experiment (Ruppert-Felsot et al. 2005). In the field of astronomy, it has been suggested that the power spectrum has a break around $k_z = 1/H$ where H is the disk scale height (Bournaud et al. 2010). Apparently, this break can be observed in the spectrum of the gas surface density $\Sigma(k)$ (Combes et al. 2012), although this is not supported by recent studies (Koch et al. 2020). We might argue that, if a forcing scale exists in real galaxies it might be related with the disk scale height. However, Musacchio & Boffetta (2017)

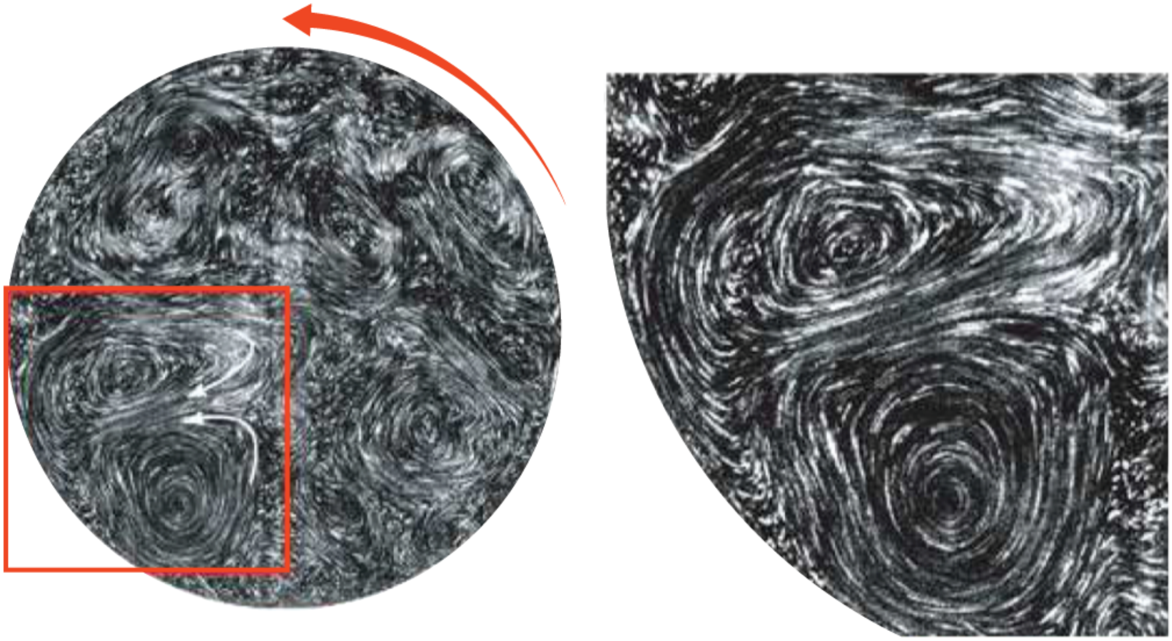

Figure 1.7: Snapshot of a rotating turbulent flow experiment (Ruppert-Felsot et al. 2005). *Left:* Particle image field in a horizontal plane 4 cm below the lid of the tank. *Right:* Close-up of the boxed region (18.7 cm x 18.7 cm) showing a cyclone (circular closed particle streaks) and an anti-cyclone (elliptical closed particle streaks to the upper-left of the cyclone).

show that the effect of the disk scale height is an additional energy cascade for $k > k_z$ as shown in Figure 1.8.

Then, if we could analyze the vorticity of gas in a galaxy we might be able to find these scales. However, the measurement of ω is limited by the uncertainties in the velocity field, and as discussed in section 1.3, we expect that these scales change for different environments in a galaxy. The power spectrum gives a description of the whole domain making this <type of analysis more complicated.

Our aim is to create a framework that allows us to obtain the contributions from these two types of motion to the local rotation. Since non-ordered motions have multiple sources, we need to adopt a statistical approach. A first order approximation is to consider non-circular motions as a Gaussian random field, described by a generating function in Fourier space $\mathcal{V}(k)$, where k is the wavenumber. If we know $\mathcal{V}(k)$ we also know the magnitude of non-circular motions as a function of spatial scale. Ultimately, $\mathcal{V}(k)$ let us know at which scales galactic rotation is still relevant.

We employ a quantitative measure of the local rotation of gas, the circulation of a fluid Γ. We define a 2-component model for gas motions with a smooth function for large scales and a generating function $\mathcal{V}(k)$ to model the non-circular motions. The velocity field arising from $\mathcal{V}(k)$ behaves as a Gaussian random field. We compare the contributions from each component to the total measured circulation. In this framework, on galactic scales the contribution of

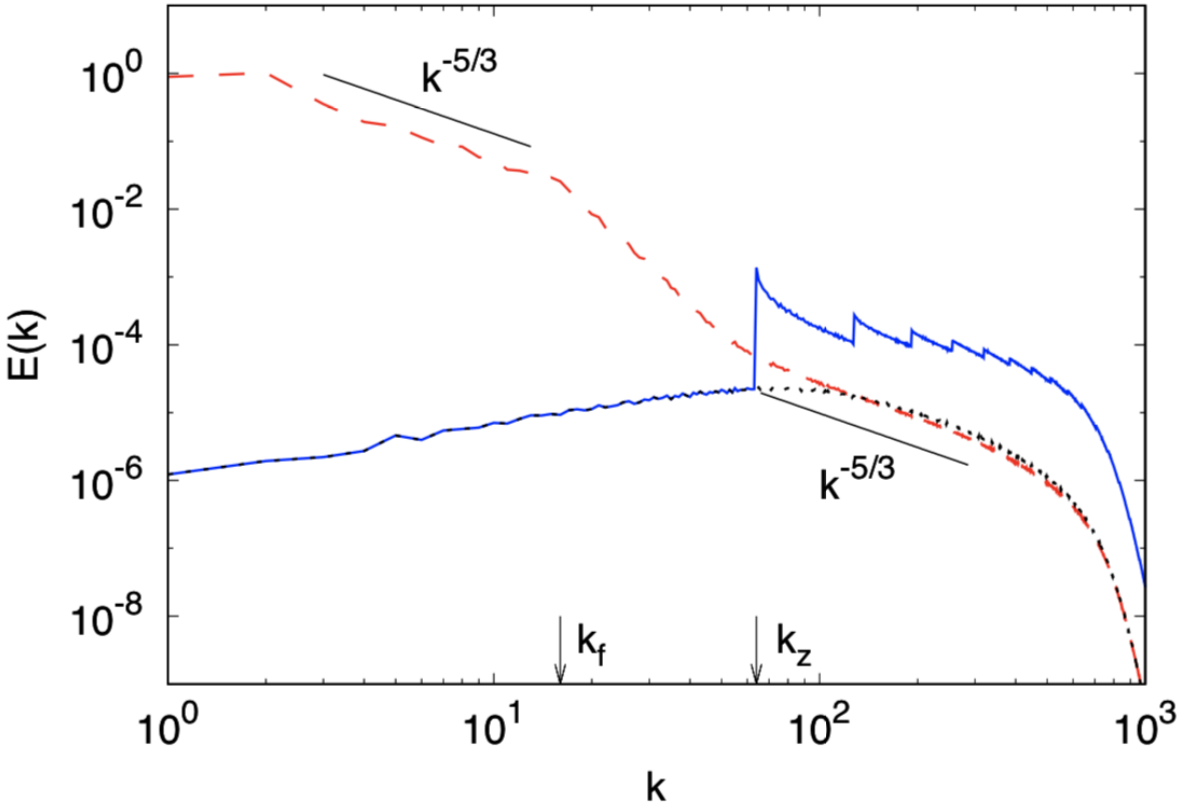

Figure 1.8: Energy spectrum $E_{2\mathrm{D}}(k)$ of the 2D mode $v_{2\mathrm{D}}$ represented by the red dashed line, and 3D mode $v_{3\mathrm{D}}$ shown by the blue solid line (Musacchio & Boffetta 2017). The black-dotted line shows the 2D spectrum of the vertically-averaged vertical velocity v_z.

non-circular motions to the circulation is negligible compared to the large scale ordered rotation. On the smallest scales the circulation field is given mostly by $\mathcal{V}(k)$. In other words, changes in the behavior of the observed distribution of Γ at different scales illustrates how the dynamics transitions from circular to non-circular motions. With this in mind, we can define a spatial scale λ_{eq} at which large scale rotation and non-circular motions contribute equally to the measured circulation of gas.

To test if circulation is a useful tool to find the transition scale between galactic rotation and non-circular motions, we use hydrodynamical simulations of galactic disks with different initial conditions. Numerical simulations are an excellent testbed for the study of circulation since they provide the full velocity field, and allow us to look for observable signature by changing different physical parameters, such as rotation or self-gravity.

Chapter 2

Vorticity and Circulation

In this chapter we introduce the concepts of vorticity and circulation of a fluid and some of their properties.

2.1. Vorticity

When we study the motion of fluids there are several properties of interest, such as its bulk motion, shear stresses, compression, and its local spin. One of the most useful notions in fluid dynamics is the vorticity vector, $\vec{\omega}$. The vorticity is a measure of the local rotation, and its direction is parallel to the spin of a fluid element. In absolute terms, the vorticity measures two times the local rotation of a fluid. The vorticity is given by the curl of the velocity field

$$\vec{\omega} = \nabla \times \vec{v} = \left(\frac{\partial v_z}{\partial y} - \frac{\partial v_y}{\partial z} \right) \hat{x} + \left(\frac{\partial v_x}{\partial z} - \frac{\partial v_z}{\partial x} \right) \hat{y} + \left(\frac{\partial v_y}{\partial x} - \frac{\partial v_x}{\partial y} \right) \hat{z}. \tag{2.1}$$

To make this concept clearer let us imagine a fluid with a circular velocity field $\vec{v} = v(R)\hat{\phi}$, where $\hat{\phi}$ is the azimuthal unit vector in cylindrical coordinates. In cylindrical coordinates, the vorticity is

$$\begin{aligned} \vec{\omega} &= \left(\frac{1}{R} \frac{\partial v_z}{\partial \phi} - \frac{\partial v_\phi}{\partial z} \right) \hat{R} + \left(\frac{\partial v_R}{\partial z} - \frac{\partial v_z}{\partial R} \right) \hat{\phi} + \frac{1}{R} \left(\frac{\partial (R v_\phi)}{\partial R} - \frac{\partial v_R}{\partial \phi} \right) \hat{z} \qquad (2.2) \\ &= \frac{v_\phi(R)}{R} \left(1 + \frac{\partial \ln v_\phi(R)}{\partial \ln R} \right) \hat{z}. \qquad (2.3) \end{aligned}$$

In the top row of Figure 2.2 we show the velocity vector field for different choices of $v_\phi(R)$: solid body rotation ($v_\phi \propto R$), a flat velocity curve ($v_\phi = v_0$), and $v_\phi \propto 1/R$. The vector field is computed on a circular path of radius R and its center is at a position $x = 10R$ and $y = 0$ in Cartesian coordinates. In the bottom row, we show the residual velocity field after subtracting the velocity of the center of the circle. Regions of gas in a field with solid

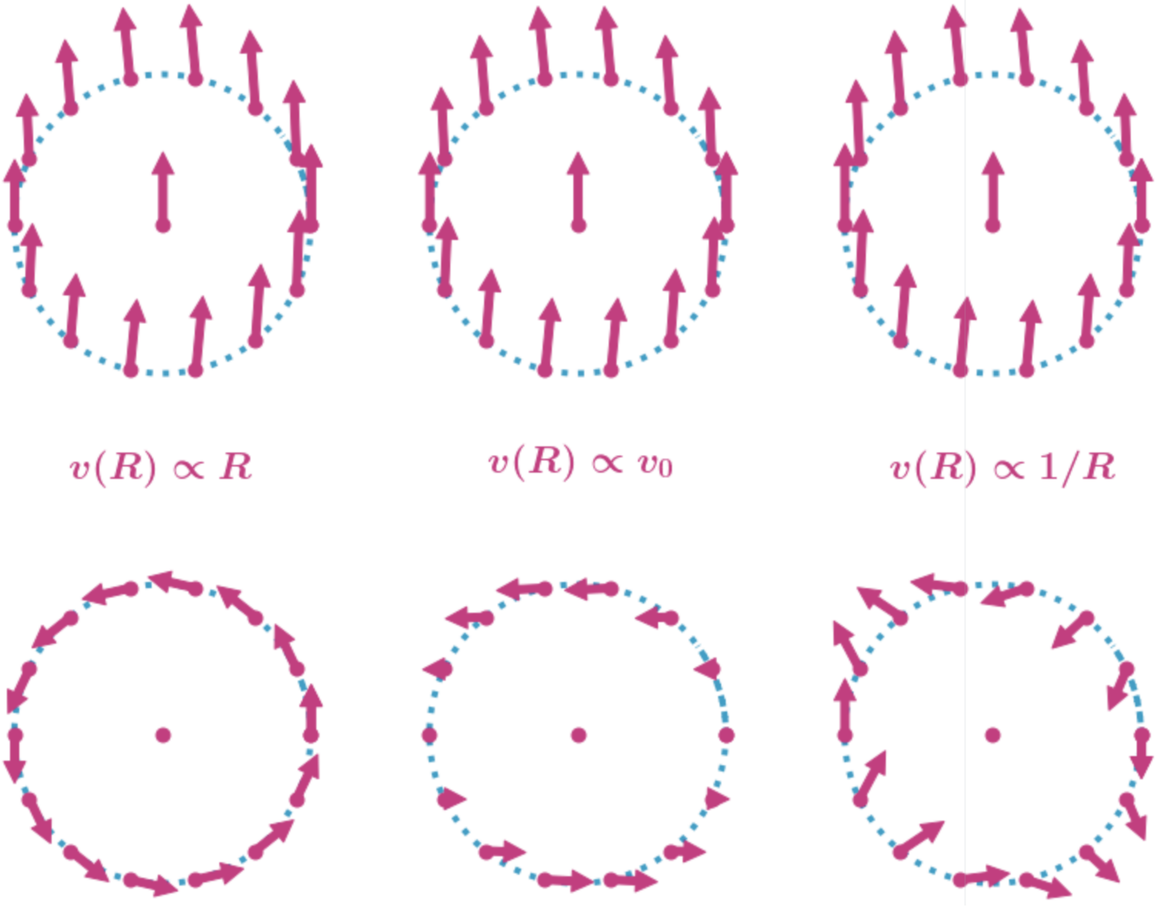

Figure 2.1: Velocity vector field for different circular velocity profiles, $v_\phi(R)$: solid body rotation $v_\phi \propto R$, a flat velocity curve $v_\phi = v_0$, and $v_\phi \propto 1/R$. *Top*: Vector field around a circular path of radius R. The center of the circles is located at (x, y)=$(10R, 0)$. *Bottom*: residual velocity field after subtracting the velocity at the center of the circle.

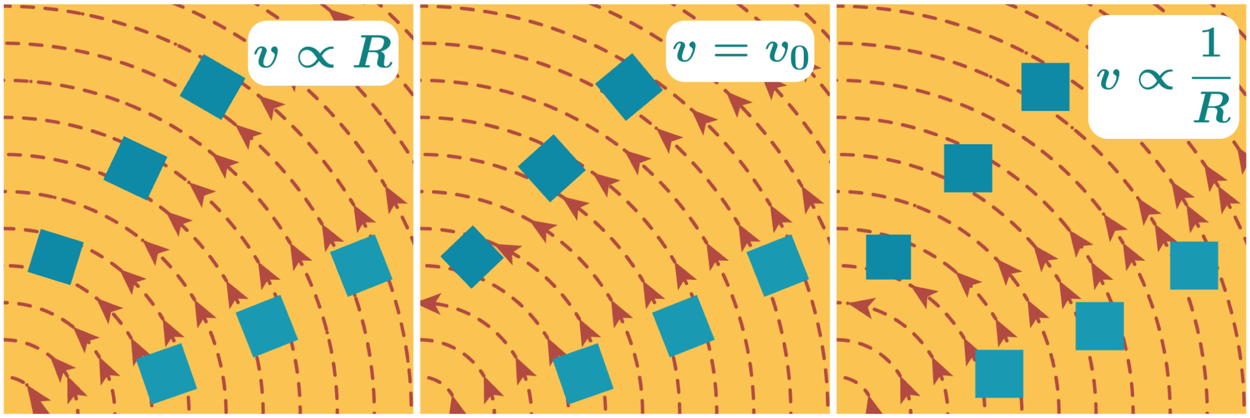

Figure 2.2: Illustration of the local rotation of fluid elements for different azimuthal velocity fields. Blue squares represent the fluid elements in two different positions in their path *Left*: Solid body rotation, $v \propto R$. The local rotation of any fluid element (blue squares) is equal to the galactic angular velocity Ω. *Middle*: Flat velocity curve, $v = v_0$. The local rotation of fluid elements $\Omega/2$. *Right*: Irrotational flow, $v \propto 1/R$. For this flow the local rotation of a fluid element is zero.

body rotation rotate around their center. For flat velocity curves, gas experiences local shear motions. Finally, for $v_\phi \propto 1/R$ we can see that gas is stretched and compressed, but it does not appear to be rotating.

Now, let us compute the vorticity field for each of these examples. In the case of solid body rotation $\vec{\omega} = 2\Omega\hat{z}$, where $\Omega(R) = v_0/R$, and patches of gas experience a local rotation of $\omega/2 = \Omega$ with respect to a local inertial reference frame. For a flat velocity curve $\vec{\omega} = \Omega\hat{z}$, and the local rotation is half the galactic rotation $\Omega/2$. We notice from equation 2.2 that there is a critical case when $v(R) \propto 1/R$. For such a velocity field, $\vec{\omega} = 0$ and fluid elements experience no local rotation with respect to an inertial reference frame. This kind of fluid is called irrotational. We illustrate the net rotation of fluid elements on each of these fields in Figure 2.2.

One important aspect of vorticity and irrotational fields comes from the Helmholtz's theorem: the vector velocity can be decomposed as the sum $\vec{v} = \vec{v}_i + \vec{v}_s$, where $\vec{v}_i$ is the irrotational component ($\nabla \times \vec{v}_i = 0$) and $\vec{v}_s$ is the solenoidal component ($\nabla \cdot \vec{v}_s = 0$). In general, the Helmoltz decomposition states that a vector field can be decomposed as $\vec{v} = -\nabla\Phi + \nabla \times \vec{A}$, where $\vec{v}_i = -\nabla\Phi$ and $\vec{v}_s = \nabla \times \vec{A}$. Then,

$$\vec{\omega} = \nabla \times \vec{v} = \nabla \times \vec{v}_s = -\nabla^2 \vec{A}, \tag{2.4}$$

the vorticity field only has information of the solenoidal component of the velocity field, that can be recovered solving the Poisson equation $\nabla^2 \vec{A} = -\vec{\omega}$ with the proper border conditions. Motions such as compression or stretching ($\nabla\vec{v} \neq 0$) do not contribute to the vorticity field.

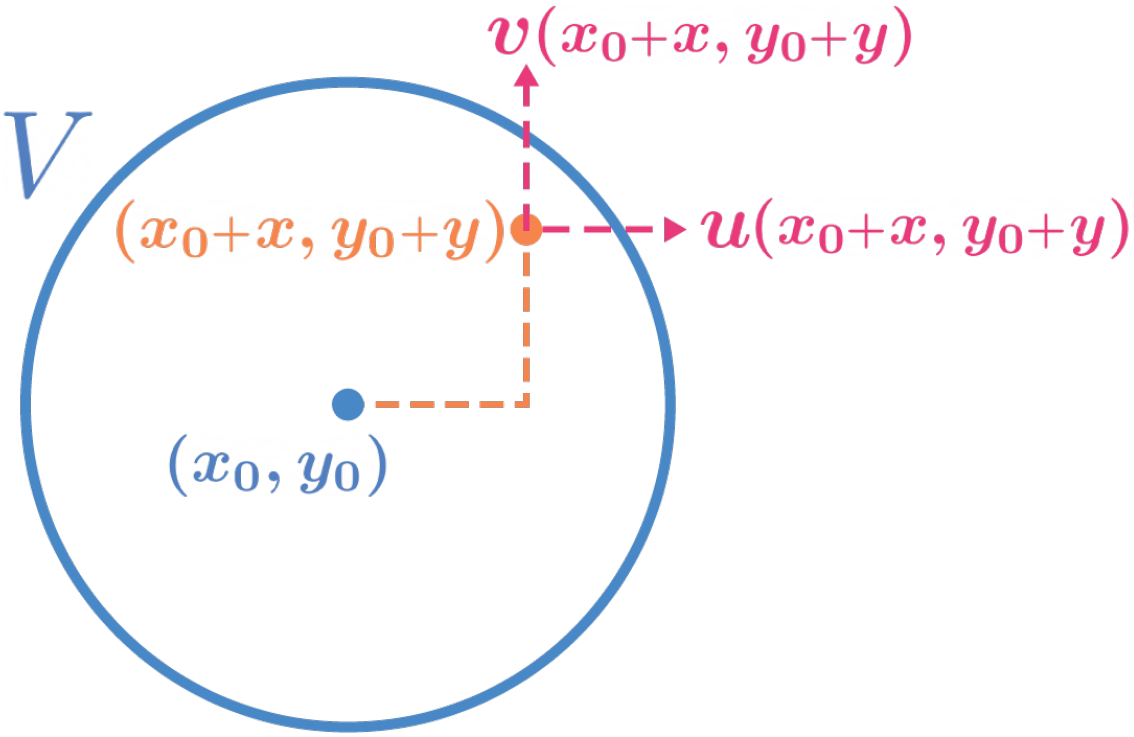

Figure 2.3: Illustration of a fluid circular element centered at (x_0, y_0) with a two dimensional velocity field $\vec{v}(x, y) = u(x, y)\hat{\imath} + v(x, y)\hat{\jmath}$

2.1.1. Angular momentum and gravitational stability

There is an insightful relation between vorticity and the angular momentum of an infinitesimal fluid element. First, let us imagine a fluid element V which center of mass is located at $\vec{r}_0 = (x_0, y_0, z_0)$ with a velocity $\vec{v} = (u, v, w)$. Figure 2.3 illustrates the fluid element in two dimensions.

Now, we expand the velocity field around the point $\vec{r}_0$.

$$u(x_0 + x, y_0 + y, z_0 + z) = u(x_0, y_0, z_0) + \frac{\partial u}{\partial x}(\vec{r}_0)x + \frac{\partial u}{\partial y}(\vec{r}_0)y + \frac{\partial u}{\partial z}(\vec{r}_0)z + ... \tag{2.5}$$

$$v(x_0 + x, y_0 + y, z_0 + z) = v(x_0, y_0, z_0) + \frac{\partial v}{\partial x}(\vec{r}_0)x + \frac{\partial v}{\partial y}(\vec{r}_0)y + \frac{\partial v}{\partial z}(\vec{r}_0)z + ... \tag{2.6}$$

$$w(x_0 + x, y_0 + y, z_0 + z) = w(x_0, y_0, z_0) + \frac{\partial w}{\partial x}(\vec{r}_0)x + \frac{\partial w}{\partial y}(\vec{r}_0)y + \frac{\partial w}{\partial z}(\vec{r}_0)z + ... \tag{2.7}$$

Now we can measure the angular momentum vector with respect to the center of mass of V

$$\vec{L}_{\vec{r}_0} = \int \rho\, \vec{r} \times \vec{v}\, \mathrm{d}\vec{r} \tag{2.8}$$

$$= \int \rho \left[y \left(\frac{\partial w}{\partial x} x + \frac{\partial w}{\partial y} y + \frac{\partial w}{\partial z} z \right) - z \left(\frac{\partial v}{\partial x} x + \frac{\partial v}{\partial y} y + \frac{\partial v}{\partial z} z \right) \right] \tag{2.9}$$

$$+ \int \rho \left[z \left(\frac{\partial u}{\partial x} x + \frac{\partial u}{\partial y} y + \frac{\partial u}{\partial z} z \right) - x \left(\frac{\partial w}{\partial x} x + \frac{\partial w}{\partial y} y + \frac{\partial w}{\partial z} z \right) \right] \tag{2.10}$$

$$+ \int \rho \left[x \left(\frac{\partial v}{\partial x} x + \frac{\partial v}{\partial y} y + \frac{\partial v}{\partial z} z \right) - y \left(\frac{\partial u}{\partial x} x + \frac{\partial u}{\partial y} y + \frac{\partial u}{\partial z} z \right) \right]. \tag{2.11}$$

$$\tag{2.12}$$

Since the origin of the reference frame is the center of mass, the terms xy, xz and yz are zero after integration. We have dropped the symbol $(\vec{r}_0)$ from the derivatives.

$$\vec{L}_{\vec{r}_0} = \int \rho \vec{r} \times \vec{v} \mathrm{d}\vec{r} = \int \rho \left[y^2 \frac{\partial w}{\partial y} - z^2 \frac{\partial v}{\partial z} \right] \hat{x} + \int \rho \left[z^2 \frac{\partial u}{\partial z} - x^2 \frac{\partial w}{\partial x} \right] \hat{y} \tag{2.13}$$

$$+ \int \rho \left[x^2 \frac{\partial v}{\partial x} - y^2 \frac{\partial u}{\partial y} \right] \hat{z} \tag{2.14}$$

$$= \left[I_{22} \frac{\partial w}{\partial y} - I_{33} \frac{\partial v}{\partial z} \right] \hat{x} + \left[I_{33} \frac{\partial u}{\partial z} - I_{11} \frac{\partial w}{\partial x} \right] \hat{y} + \left[I_{11} \frac{\partial v}{\partial x} - I_{22} \frac{\partial u}{\partial y} \right] \hat{z}, \tag{2.15}$$

I_{11}, I_{22}, and I_{33} are the components of the moment of inertia tensor $\mathbb{I}$. If the three components of the moment of inertia are equal $I_{11} = I_{22} = I_{33} = I$, then

$$\vec{L}_{\vec{r}_0} = \mathbb{I} \cdot \vec{\omega}. \tag{2.16}$$

From equation 2.16 we can see that there is a close relation between vorticity and the local angular momentum of gas. Angular momentum gives support against compression or collapse due to self-gravity. In this context, an important astrophysical parameter is the Toomre parameter Q (Toomre 1964). The Toomre parameter tells us whether radial perturbations in an axisymmetric disk are stable against gravitational collapse and fragmentation. The sources of stability are the rotation of gas, sound speed and velocity dispersion. In its usual form, Q is given by

$$Q = \frac{\kappa c_s}{\pi G \Sigma_{\mathrm{gas}}}, \tag{2.17}$$

where G is the gravitational constant, κ is the epicyclic frecuency, c_s is the sound speed, and Σ_{gas} is the gas surface density. The epicyclic frequency κ takes into account the rotation of gas, and its given by

$$\kappa^2(R) = 4\Omega(R)^2 \left(1 + \frac{\partial \ln \Omega(R)}{\partial \ln R} \right) = 2 \frac{v_\phi^2(R)}{R^2} \left(1 + \frac{\partial \ln v_\phi(R)}{\partial \ln R} \right) = 2\Omega(R)\omega_{\mathrm{rot}}(R), \tag{2.18}$$

where we have used equation 2.2, and ω_{rot} is the vorticity originated from the circular velocity $v_\phi(R) = R\Omega(R)$. This implies that for an irrotational fluid $\kappa = 0$ and the Toomre parameter $Q = 0$. Any perturbation larger than the thermal Jeans scale, $\lambda_{\mathrm{J}} \equiv c_s^2/\pi G \Sigma_{\mathrm{gas}}$, is gravitationally unstable and is not supported by rotation. It is noteworthy that in an irrotational fluid its angular velocity $\Omega \neq 0$ and its shear $\frac{\partial \Omega}{\partial r} \neq 0$. We may be tempted to study the vorticity field of real astrophysical fluids, unfortunately, vorticity is a local quantity, defined for an infinitesimal fluid element. For finite regions of space, there is another measure of rotation called circulation and its related to ω.

2.2. Circulation of a fluid Γ

A scalar quantity that measures the rotation for finite and two-dimensional regions of fluids is called **circulation** Γ (Pedlosky 1992). Circulation is defined as the line integral of the velocity field along a closed path,

$$\Gamma = \oint_{\delta S} \vec{v} \cdot \mathrm{d}\vec{l}. \tag{2.19}$$

An important property of Γ is that it is an additive quantity. For example, if we dived a region S into subregions S_1 and S_2

$$\Gamma = \oint_{\delta S} \vec{v} \cdot \mathrm{d}\vec{l} = \oint_{\delta S_1} \vec{v} \cdot \mathrm{d}\vec{l} + \oint_{\delta S_2} \vec{v} \cdot \mathrm{d}\vec{l} = \Gamma_1 + \Gamma_2 \tag{2.20}$$

The mutual boundary of S_1 and S_2, that divides the region, is integrated in different directions for Γ_1 and Γ_2, and does not contribute to their sum.

For a continuous velocity field, we can apply Stokes' theorem, which relates the line integral along a closed path to the surface integral over the area enclosed by it. This allows us to make the connection between Γ and $\vec{\omega}$:

$$\Gamma = \oint_{\delta S} \vec{v} \cdot \mathrm{d}\vec{l} = \int_S \vec{\nabla} \times \vec{v} \ \cdot \ \mathrm{d}\vec{S} = \int_S \vec{\omega} \cdot \mathrm{d}\vec{S}. \tag{2.21}$$

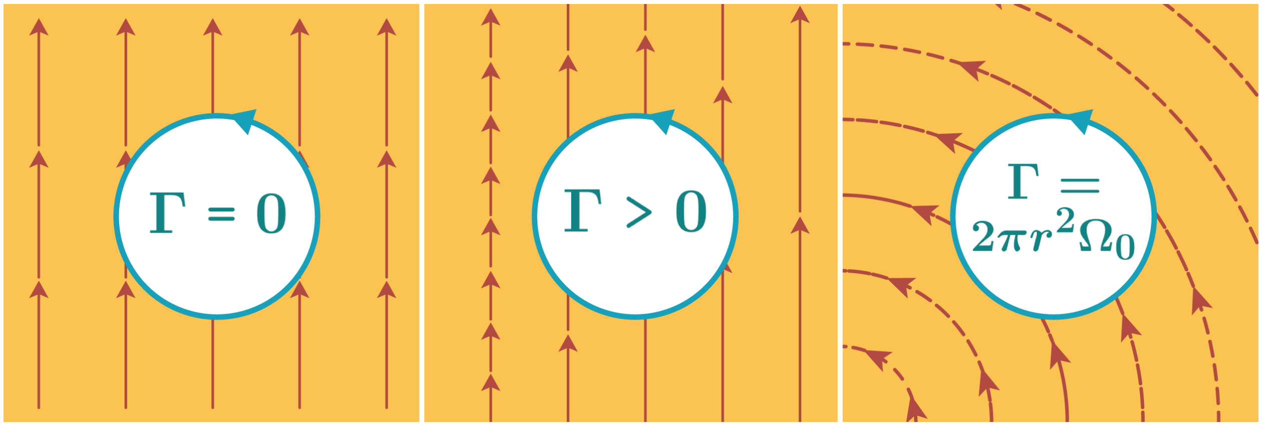

Figure 2.4: Illustration of the circulation in a closed region for different velocity fields. *Left*: Constant velocity field, $v_x = 0$ and $v_y = v_0$. *Middle*: Shear across the x-axis, $v_x = 0$ and $v_y \propto x$. *Right*: Solid body rotation with angular velocity Ω_0. The length of the arrows represents the magnitude of the velocity field.

We can think of circulation as the area-weighted integral of the vorticity field. For a two dimensional fluid, the vorticity may also be seen as the circulation per unit area for an infinitesimal fluid element. Figure 2.4 illustrates the circulation around a circular path for different velocity fields. A fluid with a constant velocity v_0 has $\Gamma = 0$, as it is constant in both magnitude and direction, and the line integral cancels out due to the change of direction

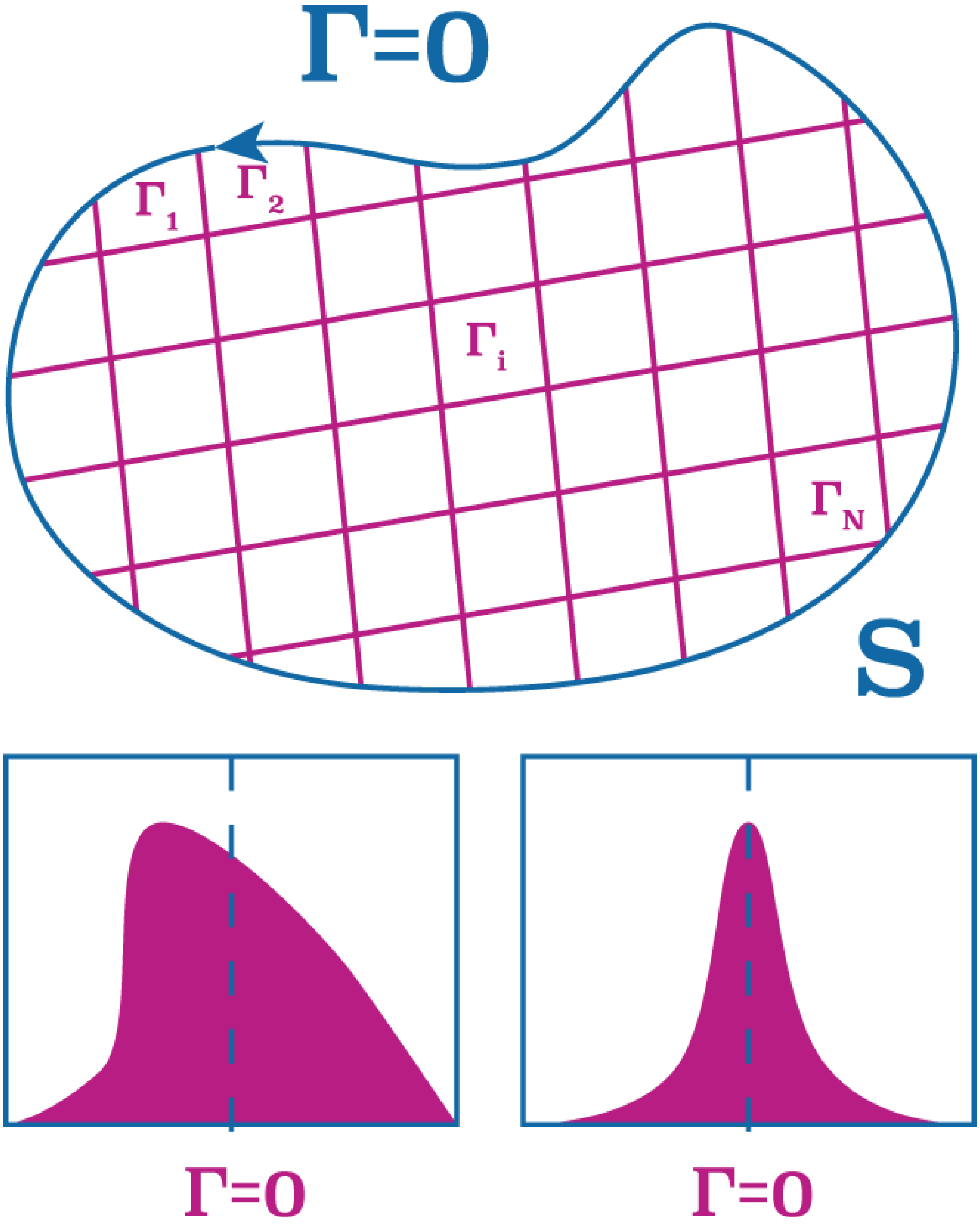

Figure 2.5: Region S with circulation $\Gamma = 0$. At smaller scales the circulation field can have different distributions that are consistent with $\Gamma = 0$.

of the path with respect to the velocity field. In other words, bulk displacements make no contribution to Γ. A shear velocity field of the form $\vec{v} = (0, \Omega_0 x)$ has $\omega = \Omega_0$ and $\Gamma = \pi r^2 \Omega_0$. The last example in Figure 2.4 shows solid body rotation, $\vec{v} = (-\Omega_0 y, \Omega_0 x)$, with $\omega = 2\Omega_0$ and $\Gamma = 2\pi r^2 \Omega_0$.

However, realistic velocity fields are not completely smooth and behave differently at different scales. For instance, we might find that over a region S the circulation is $\Gamma = 0$. But this does not imply that $\omega = 0$ over the whole region. Since the circulation is an additive quantity, if we divide S into N small sub-regions s_i, and $\Gamma = 0$, then

$$\Gamma_S = \int_S \vec{\omega} \cdot \mathrm{d}\vec{S} = \int_{s_1 + \ldots + s_N} \vec{\omega} \cdot \mathrm{d}\vec{S} = \sum_{\mathrm{i}=1}^{N} \Gamma_{s_i} = 0. \tag{2.22}$$

The sum of all Γ_i gives zero. There are infinite ways to distribute the values of Γ_i to get $\Gamma = 0$ (see Figure 2.5). The exact distribution of the circulation at this smaller scale will depend on the nature of the velocity field. This implies that only a multi-scale measurement of the circulation can characterize the velocity field.

To have a full picture of the rotation of a fluid, we need to compute the circulation of gas at each point in the fluid on regions of different sizes. By doing this, we can create distributions of circulation at different spatial scales. Since Γ can grow with the size of different scales, let us define the normalized circulation γ:

$$\gamma = \frac{\int_S \vec{\omega} \cdot \mathrm{d}\vec{S}}{\int_S \mathrm{d}S} = \frac{\Gamma}{A}, \tag{2.23}$$

where A is the area of S. For solid body rotation with angular velocity Ω_0, $\gamma = 2\Omega_0$ for any fluid patch, and the distribution of γ will be a Dirac delta function $\delta(\omega - 2\Omega_0)$. In the case of a rotating fluid with added random motions the distribution of γ will be broader at small scales and will get narrower as we increase the size of the region in question, since we are adding more random numbers and then dividing by a larger area.

We already know how to compute the vorticity for smooth circular velocity fields using equation 2.2. But we need to find a way to describe vorticity fields with a random nature. We cannot use pure white noise, since for discrete fields its distribution at different scales depends only on the maximum resolution of the field, and a field of this characteristics has no physical meaning. In the next section, we introduce the concept of Gaussian Random fields that allow us to represent random velocity fields with parameters that we can associate with different physics.

Chapter 3

Circulation and numerical tools

3.1. Gaussian Random Fields

In this thesis, we model the two dimensional velocity field as the sum of two components with different properties: the first being an axisymmetric and smooth velocity field, $v_{\rm rot} = R\Omega(R)$, which is given by galactic rotation. The second field corresponds to a Gaussian random field (GRF), $v_{\rm nc}$. GRFs are fields which follow a Gaussian distribution. In this paper, we will use a continuous GRF which is defined by a generating function in Fourier space that specifies the contribution from each spatial scale to the random velocity field (Lang & Potthoff 2011). This kind of random fields are widely used in cosmology to model the primordial perturbations of the density field (Pranav et al. 2019).

In this section we explain the properties of GRFs which come mostly from the work of Lang & Potthoff (2011). We also extend its properties to the measurements of circulation at different spatial scales.

3.1.1. Definition of Gaussian Random Fields

Let $\mathbb{W}(\vec{r})$ be a Gaussian white noise field, with mean value $\mathbb{E}(\mathbb{W}(\vec{x})) = \mu = 0$, and covariance $\mathbb{E}(\mathbb{W}(\vec{r})\mathbb{W}(\vec{p})) = \delta(\vec{r} - \vec{p})$, where $\delta(\vec{r})$ is the Dirac delta function. From $\mathbb{W}(\vec{r})$ we can create a random Gaussian field $v(\vec{r})$ by the equation:

$$v(\vec{r}) = \mathcal{F}^{-1}\left(\mathcal{V}(\vec{k})\mathcal{F}(\mathbb{W})(\vec{k})\right)(\vec{r}) = \int \mathrm{e}^{2\pi \mathrm{i}(\vec{k},\vec{r})}\mathcal{V}(\vec{k})\ \mathrm{d}\vec{k} \int \mathrm{e}^{-2\pi \mathrm{i}(\vec{k},\vec{p})}\ \mathbb{W}(\vec{p})\mathrm{d}\vec{p}, \tag{3.1}$$

where $(\cdot,\cdot)$ represents the dot product, $\mathcal{V}(\vec{k})$ is an even and positive function in Fourier space, $\mathcal{F}$ is the Fourier transform operator, and $\mathcal{F}^{-1}$ is the inverse Fourier transform:

$$\hat{f}(\vec{k}) = \mathcal{F}(f)(\vec{k}) = \int \mathrm{e}^{-2\pi \mathrm{i}(\vec{k},\vec{r})} f(\vec{r})\mathrm{d}\vec{r} \quad \& \quad f(\vec{r}) = \mathcal{F}^{-1}(\hat{f})(\vec{r}) = \int \mathrm{e}^{2\pi \mathrm{i}(\vec{k},\vec{r})}\hat{f}(\vec{k})\mathrm{d}\vec{k}. \tag{3.2}$$

The covariance $C_v(\vec{r},\vec{p})$ and variance $\sigma_v^2(\vec{r}) = C_v(\vec{r},\vec{r})$ of the GRF $v(\vec{r})$ are given by:

$$C_v(\vec{r},\vec{p}) = \int \mathrm{e}^{-2\pi \mathrm{i}(\vec{k},\vec{r}-\vec{p})}\mathcal{V}^2(\vec{k})\mathrm{d}\vec{k} \quad \& \quad \sigma_v^2(\vec{r}) = \int \mathcal{V}^2(\vec{k})\mathrm{d}\vec{k}. \tag{3.3}$$

The statistical properties of the GRF $v(\vec{r})$ are contained in the function $\mathcal{V}(\vec{k})$, while $\mathbb{W}(\vec{r})$ sets one of the random realizations of this field. In terms of physics, the $\mathcal{V}(\vec{k})$ field is related to the kinetic energy power spectrum $E(k)$. For a velocity field $v(\vec{r})$ with mean value $\langle v(\vec{r})\rangle = 0$, the mean kinetic energy per unit mass is

$$\frac{1}{2}\langle v(\vec{r})^2\rangle = \int_0^\infty E(k)\mathrm{d}k = \frac{1}{2}\sigma_v^2 = \frac{1}{2}\int \mathcal{V}^2(\vec{k})\mathrm{d}\vec{k}. \tag{3.4}$$

In this work, we analyze the velocity field in two dimensions, and we assume a symmetric function $\mathcal{V}(\vec{k}) = \mathcal{V}(k)$. With these two points the relation from above is reduced to $E(k) = 2\pi\mathcal{V}^2(k)k$.

3.1.2. Vector fields, vorticity and circulation

Equation 3.1 shows how to create a GRF $v(\vec{r})$ that is a scalar function. For a two dimensional velocity field, we need to define two components $v_x(\vec{r})$ and $v_y(\vec{r})$. We assume that these two random fields are uncorrelated, which is a major assumption and possibly unphysical in some scenarios. Once we have both fields we can compute the vorticity field $\vec{\omega}(\vec{r})$.

The vorticity field is given by the curl of the velocity field, $\vec{\omega}(\vec{r}) = \nabla \times \vec{v}(\vec{r})$. The Fourier transform of the curl operator corresponds to $\mathcal{F}(\nabla\times\vec{v})(\vec{k}) \to -2\pi\mathrm{i}\vec{k}\times\hat{\vec{v}}(\vec{k})$. We are only interested in the z-component of the vorticity field, which we refer as ω. Then, the Fourier transform of ω is $\hat{\omega}(\vec{k}) = -2\pi\mathrm{i}(k_x\hat{v}_y(\vec{k}) - k_y\hat{v}_x(\vec{k}))$. If v_x and v_y are defined by $\mathcal{V}(k)$, then ω will be defined by the function $\mathcal{W}(k) = 2\pi\mathcal{V}(k)k$. Then, the vorticity field is given by

$$\omega(\vec{r}) = \mathcal{F}^{-1}\left(\mathcal{W}(\vec{k})\mathcal{F}(\mathbb{W}(\vec{r}))\right) = \int \mathrm{e}^{2\pi\mathrm{i}(\vec{k},\vec{r})}\ \mathcal{W}(\vec{k})\ \mathrm{e}^{-2\pi\mathrm{i}(\vec{k},\vec{r'})}\ \mathbb{W}(\vec{r'})\ \mathrm{d}\vec{k}\mathrm{d}\vec{r'}. \tag{3.5}$$

The variances of the velocity fields and the vorticity fields are related by:

$$\frac{\sigma_\omega^2}{\sigma_v^2} = \frac{\int \mathcal{W}(k)^2k\mathrm{d}k}{\int \mathcal{V}(k)^2k\mathrm{d}k} = 4\pi^2\frac{\int \mathcal{V}(k)^2k^3\mathrm{d}k}{\int \mathcal{V}(k)^2k\mathrm{d}k} = \frac{1}{4\pi^2}\frac{\int \mathcal{W}(k)^2k\mathrm{d}k}{\int \mathcal{W}(k)^2\frac{1}{k}\mathrm{d}k}. \tag{3.6}$$

Now we have a relation between $\omega(x,y)$ and the function that sets the statistical properties of the velocity field $\mathcal{V}(k)$. For our calculations, we use the function $\mathcal{W}(k)$ to compute the properties of random fields. To translate our calculations to the parameters of the velocity field we use $\mathcal{W}(k) = 2\pi\mathcal{V}(k)k$.

What follows from here is to compute the normalized circulation $\gamma(\vec{r},\ell)$ for a square region of size ℓ centered at $\vec{r} = (x, y)$:

$$\gamma(\vec{r},\ell) = \frac{1}{\ell^2}\int_{x-\frac{\ell}{2}}^{x+\frac{\ell}{2}}\int_{y-\frac{\ell}{2}}^{y+\frac{\ell}{2}} \omega(\vec{r''})\mathrm{d}\vec{r''}. \tag{3.7}$$

Replacing equation 3.5 in 3.7

$$\gamma(\vec{r},\ell) = \frac{1}{\ell^2}\int_{x-\frac{\ell}{2}}^{x+\frac{\ell}{2}}\int_{y-\frac{\ell}{2}}^{y+\frac{\ell}{2}} \mathrm{d}\vec{r''}\int \mathrm{e}^{2\pi\mathrm{i}(\vec{k},\vec{r''})}\mathcal{W}(\vec{k})\mathrm{e}^{-2\pi\mathrm{i}(\vec{k},\vec{r'})}\mathbb{W}(\vec{r'})\mathrm{d}\vec{k}\mathrm{d}\vec{r'}. \tag{3.8}$$

To get rid of x and y in the limits of the integrals we apply the variable change $\vec{r''} \to \vec{r}+\vec{r''}$ and we get

$$\gamma(\vec{r},\ell) = \frac{1}{\ell^2}\int_{-\frac{\ell}{2}}^{\frac{\ell}{2}}\int_{-\frac{\ell}{2}}^{\frac{\ell}{2}} \mathrm{d}\vec{r''}\int \mathrm{e}^{2\pi\mathrm{i}(\vec{k},\vec{r})}\mathrm{e}^{2\pi\mathrm{i}(\vec{k},\vec{r''})}\mathcal{W}(\vec{k})\mathrm{e}^{-2\pi\mathrm{i}(\vec{k},\vec{r'})}\mathbb{W}(\vec{r'})\mathrm{d}\vec{k}\mathrm{d}\vec{r'}. \tag{3.9}$$

Now, we can integrate the term $\mathrm{e}^{2\pi\mathrm{i}(\vec{k},\vec{r''})}\mathrm{d}\vec{r''}$ over the square region

$$\int_{-\frac{\ell}{2}}^{\frac{\ell}{2}}\int_{-\frac{\ell}{2}}^{\frac{\ell}{2}} \mathrm{e}^{2\pi\mathrm{i}(\vec{k},\vec{r''})}\mathrm{d}\vec{r''} = \int_{-\frac{\ell}{2}}^{\frac{\ell}{2}} \mathrm{e}^{2\pi\mathrm{i}k_x x''}\mathrm{d}x''\int_{-\frac{\ell}{2}}^{\frac{\ell}{2}} \mathrm{e}^{2\pi\mathrm{i}k_y y''}\mathrm{d}y'' = \frac{\sin(\pi k_x\ell)}{\pi k_x}\frac{\sin(\pi k_y\ell)}{\pi k_y}, \tag{3.10}$$

$$\gamma(\vec{r},\ell) = \frac{1}{\ell^2}\int \mathrm{e}^{2\pi\mathrm{i}(\vec{k},\vec{r})}\mathcal{W}(\vec{k})\frac{\sin(\pi k_x\ell)\sin(\pi k_y\ell)}{\pi^2 k_x k_y}\mathrm{e}^{-2\pi\mathrm{i}(\vec{k},\vec{r'})}\mathbb{W}(\vec{r'})\mathrm{d}\vec{k}\mathrm{d}\vec{r'}. \tag{3.11}$$

We can see that $\gamma(\vec{r},\ell)$ has the form $\mathcal{F}^{-1}\left(M(\vec{k})\mathcal{F}(\mathbb{W}(\vec{r}))\right)$ with

$$M(\vec{k}) = \frac{1}{\ell^2}\mathcal{W}(\vec{k})\ \frac{\sin(\pi k_x\ell)\sin(\pi k_y\ell)}{\pi^2 k_x k_y}. \tag{3.12}$$

Then, $\gamma(\vec{r},\ell)$ is a two dimensional GRF with a variance given by:

$$\sigma^2_{\gamma,\ell} = \int M(\vec{k})^2\mathrm{d}\vec{k} = \frac{1}{\ell^4}\int \mathcal{W}(\vec{k})^2\ \frac{\sin(\pi k_x\ell)^2\sin(\pi k_y\ell)^2}{\pi^4 k_x^2 k_y^2}\ \mathrm{d}k_x\mathrm{d}k_y \tag{3.13}$$

3.1.3. Examples and numerical tests of Gaussian Random Fields

We have derived equations showing how the variance of the probability density distribution of γ, pdf(γ), changes with spatial scale ℓ. In this thesis, we deal with discrete velocity fields and therefore we need to test the applicability of our equations to velocity and vorticity maps with different parameters. We start by showing how the velocity and vorticity maps change with different generating functions $\mathcal{V}(k)$. For the first examples we choose $\mathcal{V}(k)$ to be of the form:

$$\mathcal{V}(k) = \begin{cases} \mathcal{V}_0 k^{-n} & \text{if } k_{\min} \leq k < k_{\max} \\ 0 & \text{elsewhere} \end{cases} \tag{3.14}$$

We start by looking how the fields change with the exponent of the power law n, with values $n \in 1, 2, 3$. We create maps with dimensions 1024×1024 with $k_{\max} = 256/L$ and $k_{\min} = 2/L$. Since this exercise is only to illustrate the structure of the different fields with arbitrary units, we normalize each field, velocity and vorticity, by its standard deviation.

Figure 3.1 shows the velocity and vorticity fields for different values of n. Higher exponents mean that most of the structure of the fields is contained at low wavenumbers k, i.e. at larger scales. As the exponent grows we see how the structure of each field is dominated by large structures. For $n = 1$ in the velocity fields we see a mixture of large scale structure plus variations at the small scales. An exponent $n = 1$ for $\mathcal{V}(k)$ implies an exponent $n = 0$ for $\mathcal{W}$, which means that the vorticity field is almost pure white noise. Something noteworthy is the similitude between the structure of the vorticity fields with velocity fields at the previous row. The cause of this resemblance is that their corresponding generating functions $\mathcal{V}(k)$ and $\mathcal{W}(k)$ are the same power law.

To illustrate that the relation $\mathcal{W}(k) \propto \mathcal{V}(k)k$ does hold for discrete fields, we show the profiles of $\tilde{v}_x(k)$, $\tilde{v}_y(k)$ and $\tilde{\omega}_z(k)$, which are the Fourier transforms of the velocity and vorticity fields. Figure 3.2 shows the profiles in Fourier space for $\mathcal{V}(k) \propto n^{-2}$.

For the following examples and tests we use the same model of $\mathcal{V}(k)$ used to analyze the simulations, a broken power law:

$$\mathcal{V}(k) = \begin{cases} \mathcal{V}_0 k^{-n_1} & \text{if } k_{\min} \leq k < k_{\mathrm{c}} \\ \mathcal{V}_0 k_c^{-n_1+n_2} k^{-n_2} & \text{if } k_c \leq k \leq k_{\max} \\ 0 & \text{elsewhere} \end{cases} \tag{3.15}$$

This function has a new important parameter, the transition wavenumber k_c. We show how the GRFs change for different values of k_c in Figure 3.3. We set $n_1 = 1$ and $n_2 = 3$ and choose values for $k_{\mathrm{c}} \in (256/L, 32/L, 4/L)$, where L is the length size of the image.

The generating function of the vorticity field is then

$$\mathcal{W}(k) = \begin{cases} \mathcal{W}_0 k^{-n_1+1} & \text{if } k_{\min} \leq k < k_{\mathrm{c}} \\ \mathcal{W}_0 k_c^{-n_1+n_2} k^{-n_2+1} & \text{if } k_c \leq k \leq k_{\max} \\ 0 & \text{elsewhere} \end{cases} \tag{3.16}$$

with $\mathcal{W}_0 = 2\pi\mathcal{V}_0$.

Our first test consists in computing the standard deviation of the velocity and vorticity

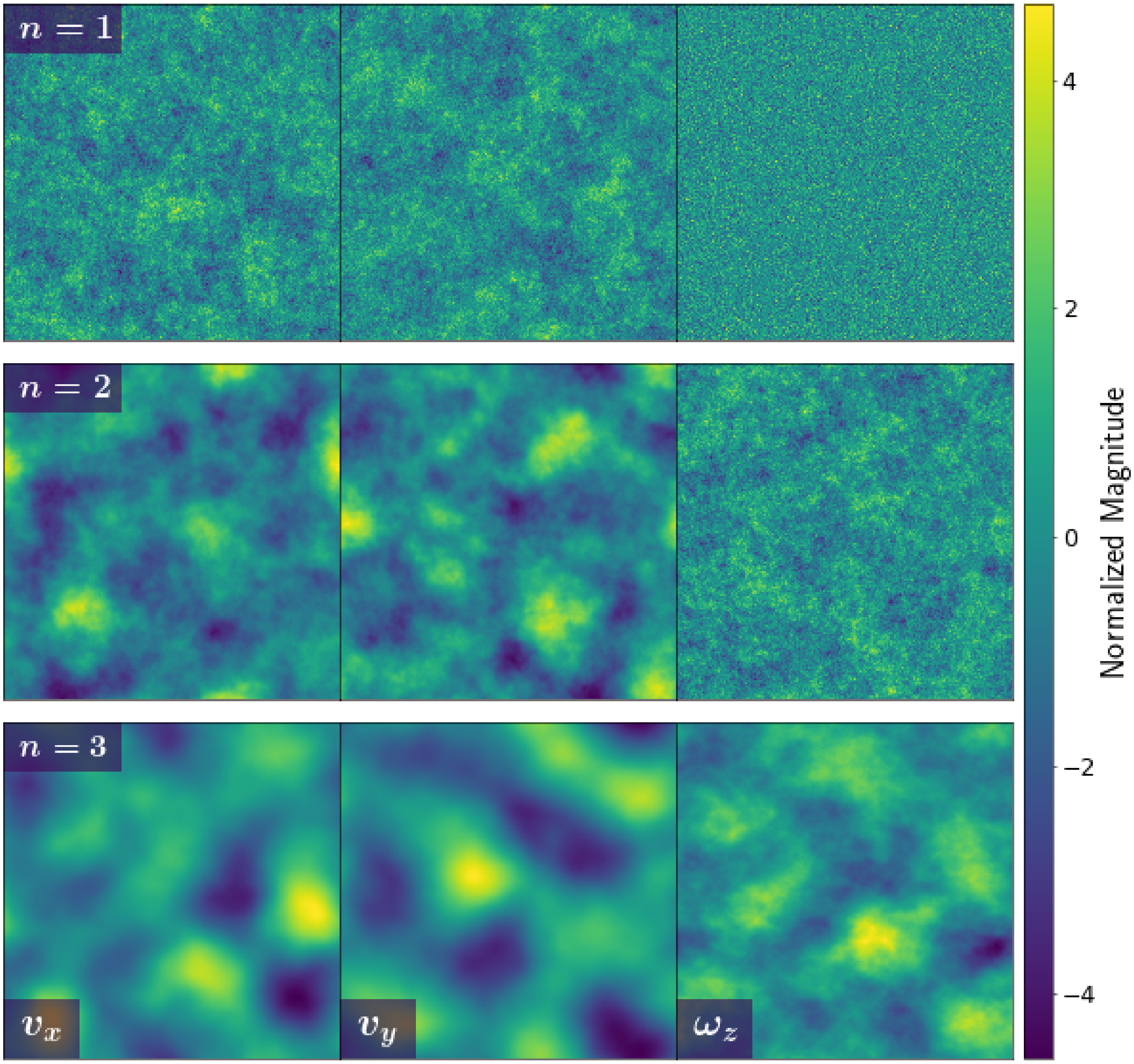

Figure 3.1: Velocity and vorticity maps for different functions $\mathcal{V}(k) \propto k^{-n}$. From left to right we show the fields $v_x(x, y)$, $v_y(x, y)$ and $\omega_z(x, y)$. From top to bottom the exponent n takes the values 1, 2 and 3. Each field has been normalized by its standard deviation, i.e. the fields correspond to v_x/σ_{vx}, v_y/σ_{vy} and ω_z/σ_ω

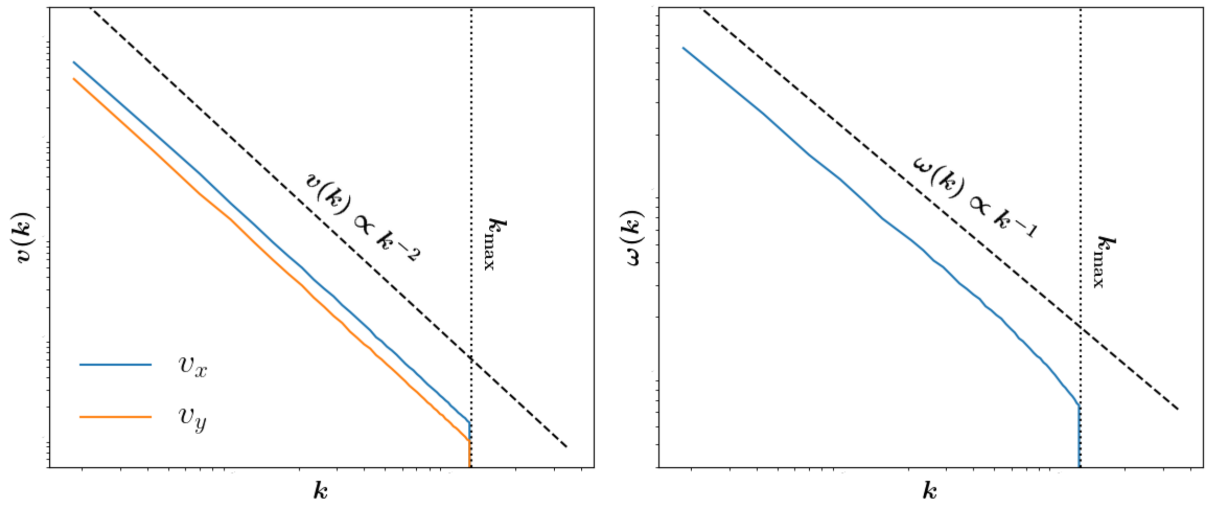

Figure 3.2: Profiles of the Fourier transforms of the velocity and vorticity fields as a function of wavenumber k. *Left*: Profiles of $\tilde{v}_x(k)$ a $\tilde{v}_y(k)$ as a function of k shown by the blue and orange lines respectively. The black dashed lines illustrates the proportionality $\tilde{v} \propto k^{-n} = k^{-2}$. *Right*: Profile of $\tilde{\omega}_z(k)$ as a function of k. The black dashed lines illustrates the proportionality $\tilde{\omega} \propto k^{-n+1} = k^{-1}$.

fields, i.e., σ_v and σ_ω from equations 4.8 and 3.16. Let us start with the velocity field:

$$\sigma_v^2 = \int \mathcal{V}^2(\vec{k})\mathrm{d}\vec{k} = 2\pi\mathcal{V}_0^2 \left[\int_{k_{\min}}^{k_{\mathrm{c}}} k^{-2n_1} k\mathrm{d}k + k_{\mathrm{c}}^{-2n_1+2n_2} \int_{k_{\mathrm{c}}}^{k_{\max}} k^{-2n_2} k\mathrm{d}k\right]. \tag{3.17}$$

For convenience we rewrite equation 3.17 as $\sigma_v^2 = 2\pi\mathcal{V}_0^2\mathcal{I}(n_1, n_2)$

$$\mathcal{I}(n_1,n_2) = \begin{cases} \dfrac{k_{\mathrm{c}}^{2-2n_1} - k_{\min}^{2-2n_1}}{2-2n_1} + k_{\mathrm{c}}^{2(n_2-n_1)} \dfrac{k_{\max}^{2-2n_2} - k_{\mathrm{c}}^{2-2n_2}}{2-2n_2} & \text{if } n_1 \neq 1 \ ; \ n_2 \neq 1 \\ \ln\left(\dfrac{k_{\mathrm{c}}}{k_{\min}}\right) + k_{\mathrm{c}}^{2(n_2-n_1)} \dfrac{k_{\max}^{2-2n_2} - k_{\mathrm{c}}^{2-2n_2}}{2-2n_2} & \text{if } n_1 = 1 \ ; \ n_2 \neq 1 \\ \dfrac{k_{\mathrm{c}}^{2-2n_1} - k_{\min}^{2-2n_1}}{2-2n_1} + k_{\mathrm{c}}^{2(n_2-n_1)} + \ln\left(\dfrac{k_{\max}}{k_{\mathrm{c}}}\right) & \text{if } n_1 \neq 1 \ ; \ n_2 = 1 \\ \ln\left(\dfrac{k_{\max}}{k_{\min}}\right) & \text{if } n_1 = 1 \ ; \ n_2 = 1 \end{cases} \tag{3.18}$$

With this definition we can write $\sigma_\omega^2 = 2\pi\mathcal{W}_0^2\mathcal{I}(n_1-1, n_2-1) = 8\pi^3\mathcal{V}_0^2\mathcal{I}(n_1-1, n_2-1)$. And now we can relate σ_v and σ_ω through the equation

$$\sigma_\omega = 2\pi\sigma_v\sqrt{\frac{\mathcal{I}(n_1-1, n_2-1)}{\mathcal{I}(n_1, n_2)}}. \tag{3.19}$$

Equation 3.19 is key to our work since what we actually do is to compute properties of the circulation field for different functions $\mathcal{W}(k)$ and we link its parameters to parameters

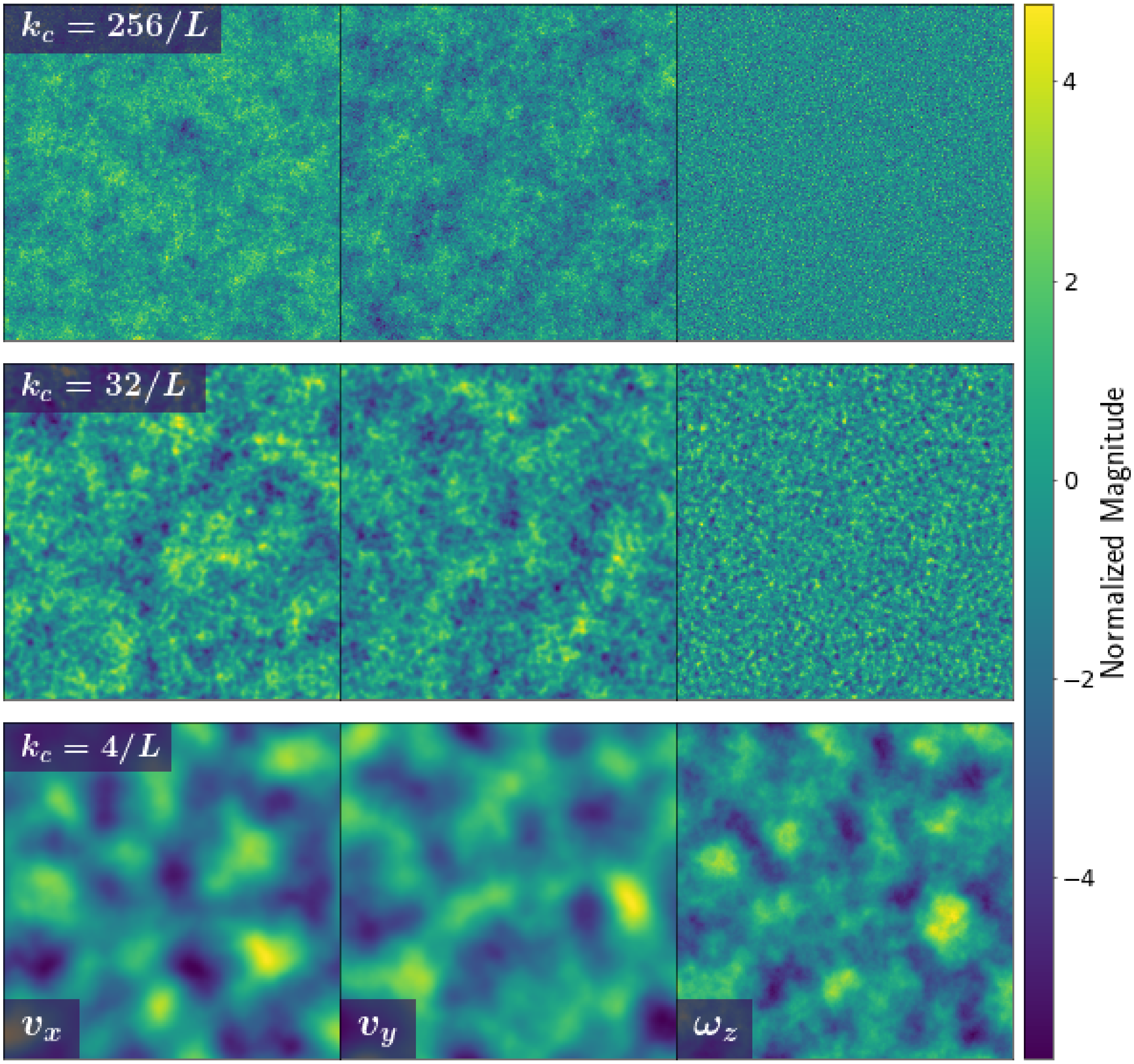

Figure 3.3: Two dimensional maps of v_x, v_y, and ω_z for different values of k_c. The velocity maps are generated using equation 4.8, with $n_1 = 1$ and $n_2 = 3$. From top to bottom k_c takes the values $256/L$, $32/L$, and $4/L$.

of $\mathcal{V}(k)$. We may want to test whether discrete velocity fields are able to reproduce equation 3.19, however discrete fields only have information down to the resolution level. For example, if we want to compute the dispersion of the vorticity field we have to compute $\sigma^2_{\gamma,\ell}$ from equation 3.13, with ℓ equal to the grid size of the discrete field. The same applies to the velocity field. Therefore, the next step in our tests is to check equation 3.13.

3.1.4. How to compute $\sigma^2_{\gamma,\ell}$

Now that we have already define the basis of GRFs and its application to velocity and vorticity fields, we continue with the actual application of GRFs to our work. For a given vorticity map, obtained from $\mathcal{V}(k)$, we compute the normalized circulation $\gamma(\vec{r},\ell)$ for different spatial scales ℓ. From these measurements, we compute its variance $\sigma^2_{\gamma,\ell}$ and we compare it to the values obtained from equation 3.13. We do this for different combinations of n_1, n_2, k_c and σ_v. Finally, we have to choose an algorithm to calculate equation 3.13 for a given set of parameters.

To integrate equation 3.13 we use one of the methods of Montecarlo integration. Given a function $f(x)$ and a probability density function $p(x)$ we can write the integral of $f(x)$ as

$$I = \int_V f(x)\mathrm{d}x = \int_V p(x)\frac{f(x)}{p(x)}\mathrm{d}x = E_p\left[\frac{f(x)}{p(x)}\right], \tag{3.20}$$

where $E_p[x]$ is the expected value of x that follows the distribution $p(x)$. Thus, if we choose random numbers $(x_1, ..., x_N)$ from the distribution $p(x)$

$$I = \lim_{N\to\infty} \frac{1}{N}\sum_{\mathrm{i}=1}^{N} \frac{f(x_\mathrm{i})}{p(x_\mathrm{i})}. \tag{3.21}$$

This method is useful for functions that are too steep, replacing $f(x)$ by a flatter function $f(x)/p(x)$ and sampling values of x more efficiently.

To compute equation 3.13 we choose $p(k) = \mathcal{W}^2(k)k/2\pi A$, where A is a normalization constant. To draw samples of k from $p(k)$ we need to define the cumulative density distribution $P(k)$

$$P(k) = \int_{k_{\min}}^{k} p(k')\mathrm{d}k' = \frac{1}{2\pi A}\int_{k_{\min}}^{k} \mathcal{W}^2(k')k'\mathrm{d}k' \ ; \ P(k_{\max}) = 1. \tag{3.22}$$

The normalization of $p(k)$ implies that $A = \int \mathcal{W}(k)\mathrm{d}\vec{k} = \sigma^2_\omega$. To obtain a random number following the distribution $p(k)$ we need to compute $k = P^{-1}(\xi)$, where ξ follows the uniform distribution $\mathcal{U}(0,1)$. Since $\mathcal{W}(k)$ is a broken power law that changes in k_c (equation 3.16), we need to define the point $\xi_c = P(k_\mathrm{c})$ to properly invert $P(k)$. We begin by replacing the exponents of the power law by $m_1 = n_1 - 1$ and $m_2 = n_2 - 1$. With these substitutions $\mathcal{V}(k)$ and $\mathcal{W}(k)$ have the same form. Now we can use what we have already calculated for $\mathcal{V}(k)$ in equation 3.18.

For simplicity we start by making some definitions

$$\begin{aligned} f_1 &= \frac{k_\mathrm{c}^{2-2m_1}}{2-2m_1} - \frac{k_\mathrm{min}^{2-2m_1}}{2-2m_1} \quad &;\quad f_2 &= \frac{k_\mathrm{c}^{2(m_2-m_1)}}{2-2m_2}\left[k_\mathrm{max}^{2-2m_2} - k_\mathrm{c}^{2-2m_2}\right] \\ g_1 &= \ln(k_\mathrm{c}/k_\mathrm{min}) \quad &;\quad g_2 &= k_\mathrm{c}^{2(m_2-m_1)}\ln(k_\mathrm{max}/k_\mathrm{c}) \end{aligned}$$

Now we can express A and ξ_c in terms of f_1, f_2, g_1 and g_2

$$\begin{aligned} &\text{if } m_1 \neq 1 \;;\; m_2 \neq 1 \quad ;\; A = f_1 + f_2 \;;\; \xi_c = f_1/A \\ &\text{if } m_1 = 1 \;;\; m_2 \neq 1 \quad ;\; A = g_1 + f_2 \;;\; \xi_c = g_1/A \\ &\text{if } m_1 \neq 1 \;;\; m_2 = 1 \quad ;\; A = f_1 + g_2 \;;\; \xi_c = f_1/A \\ &\text{if } m_1 = 1 \;;\; m_2 = 1 \quad ;\; A = g_1 + g_2 \;;\; \xi_c = g_1/A \end{aligned} \tag{3.23}$$

	$\xi \leq \xi_c$	$\xi > \xi_c$
$m_1 \neq 1; m_2 \neq 1$	$k = (k_\mathrm{min}^{2\text{-}2m_1} + (2\text{ - }2m_1)A\xi)^{\frac{1}{2\text{-}2m_1}}$	$k = (k_\mathrm{c}^{2\text{-}2m_2} + (2\text{ - }2m_2)k_\mathrm{c}^{2(m_1\text{-}m_2)}A(\xi\text{ - }\xi_c))^{\frac{1}{2\text{-}2m_2}}$
$m_1 = 1; m_2 \neq 1$	$k = k_\mathrm{min}\exp(\xi A)$	$k = (k_\mathrm{c}^{2\text{-}2m_2} + (2\text{ - }2m_2)k_\mathrm{c}^{2(m_1\text{-}m_2)}A(\xi\text{ - }\xi_c))^{\frac{1}{2\text{-}2m_2}}$
$m_1 \neq 1; m_2 = 1$	$k = (k_\mathrm{min}^{2\text{-}2m_1} + (2\text{ - }2m_1)A\xi)^{\frac{1}{2\text{-}2m_1}}$	$k = k_\mathrm{c}\exp(A(\xi\text{ - }\xi_c)k_\mathrm{c}^{2(m_1\text{-}m_2)})$
$m_1 = 1; m_2 = 1$	$k = k_\mathrm{min}\exp(\xi A)$	$k = k_\mathrm{c}\exp(A(\xi\text{ - }\xi_c)k_\mathrm{c}^{2(m_1\text{-}m_2)})$

Knowing how to distribute k according to $p(k)$ we can calculate equation 3.13 :

$$\sigma_{\gamma,\ell}^2 = \frac{\sigma_\omega^2}{\pi^4\ell^4 N}\sum_{i=1}^{N}\frac{\sin^2(\pi k_{x,i}\ell)\sin^2(\pi k_{y,i}\ell)}{k_{x,i}^2 k_{y,i}^2}. \tag{3.24}$$

We use $k_{x,i} = k_i\cos\phi_i$ and $k_{y,i} = k_i\sin\phi_i$ where ϕ_i is a random variable with a distribution $\mathcal{U}(0, 2\pi)$. In the limit $\ell \to 0$ we have $\gamma \to \omega$ from equation 3.7 and $\sigma_\gamma \to \sigma_\omega$ from equation 3.24. Since one of our main parameters is the velocity dispersion σ_v, we use equation 3.19 to rewrite equation 3.24 as:

$$\sigma_{\gamma,\ell}^2 = 4\pi^2\sigma_v^2\frac{\mathcal{I}(n_1-1, n_2-1)}{\mathcal{I}(n_1, n_2)}\sum_{i=1}^{N}\frac{\sin^2(\pi k_{x,i}\ell)\sin^2(\pi k_{y,i}\ell)}{k_{x,i}^2 k_{y,i}^2}. \tag{3.25}$$

This is the equation we use to compute numerically $\sigma_{\gamma,\ell}^2$ as a function of n_1, n_2, σ_v and k_c, where k is sampled from the probability density function $p(k)$.

We now test how well equation 3.25 is able to reproduce the dispersion of γ in a set of discrete velocity fields with different values for n_1, n_2 and k_c. Since one velocity map is only one realization of a GRF, we create 40 pairs of velocity maps (v_x, v_y) for each set of parameters. For these examples we use the following configurations: the exponents take one of these three pairs of values $(n_1 = 1, n_2 = 2)$, $(n_1 = 1, n_2 = 3)$, and $(n_1 = 2, n_2 = 3)$, while k_c takes the values $(16/L, 45/L, 128/L)$, where L is the size of the square velocity maps. We show the comparison between the numerical integration of equation 3.25 and the values measured in discrete fields in Figure 3.4.

Figure 3.4 shows how our numerical integration of the dispersion of γ, σ_γ^a, nicely follows the measured dispersion σ_γ^m. Below each plot we show the fractional error of σ_γ^a as a function of ℓ. We can observe how the uncertainty of σ_γ^m grows with ℓ, and how the error notably increases when $\ell > L/4$.

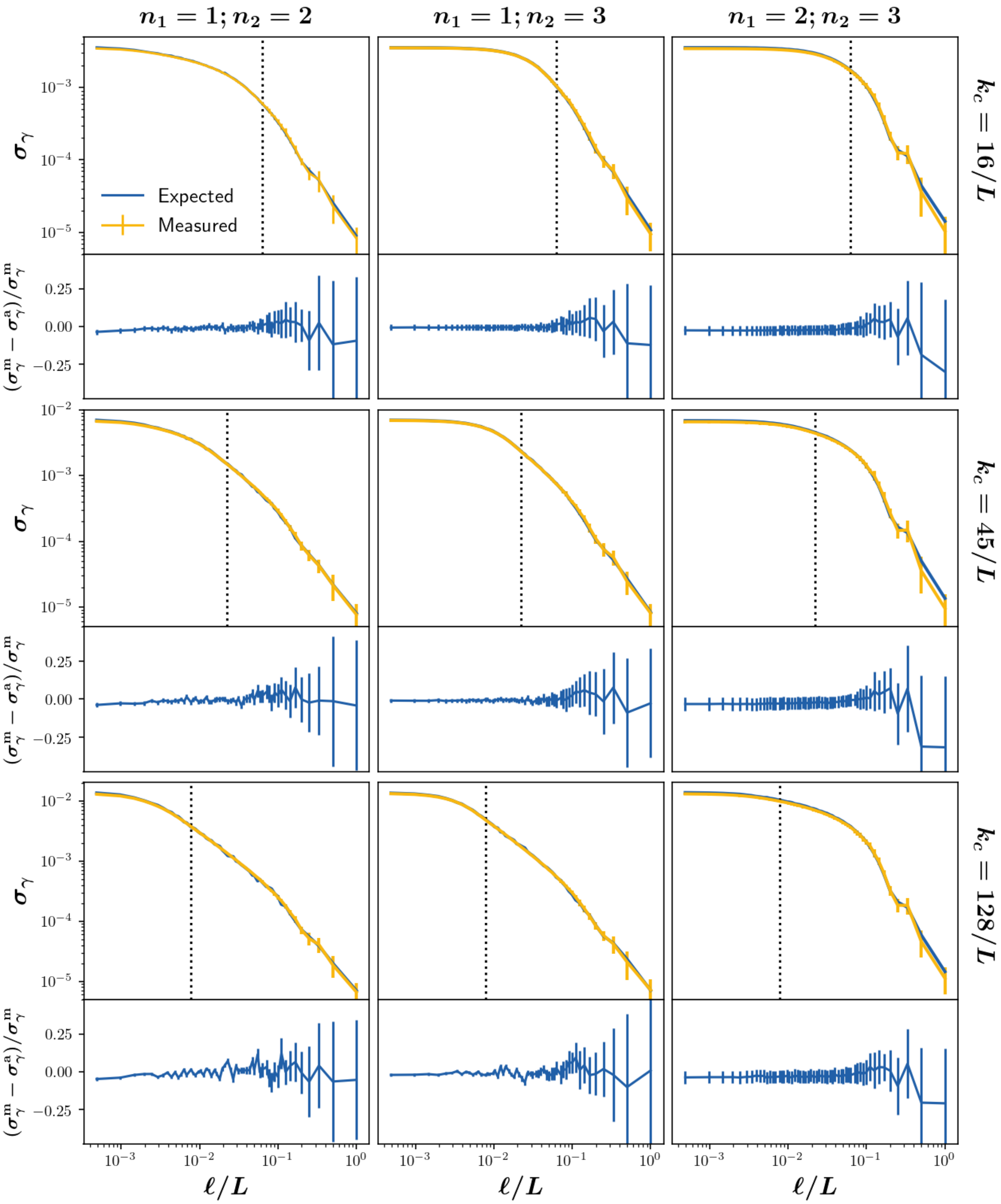

Figure 3.4: Dispersion σ_γ as a function of scale ℓ. The blue solid line shows the dispersion of γ obtained from equation 3.25, while the yellow line shows σ_γ obtained from 40 realizations of GRFs. *From left to right:* the exponents (n_1, n_2) take the values (1,2), (1,3), and (2,3). *From top to bottom:* increasing k_c with values $16/L$, $45/L$, and $128/L$ where L is the spatial size of the velocity maps.

3.1.5. Toy Models

Now that we have established how to compute σ_γ numerically, we create toy models to show clearly how the parameters of $\mathcal{V}(k)$, n_1, n_2, k_c, and σ_v, affect σ_γ at different scales ℓ. We create velocity maps with size $L = 1$ and resolution L/N, with $N = 10^4$. To aid our eyes to compare the effects of changing parameters we normalize $\sigma_\omega = 1$. The function $\mathcal{V}(k)$ is defined by equation 4.8.

We show the dispersion in γ_ℓ as a function of ℓ for different combinations of parameters in Figure 3.5. The dispersion is calculated by the integral 3.25. In the top panel we vary $k_{\rm max}$ from 10 to 10^4, while $n_1 = n_2 = 0$ which represents white noise. The parameter $k_{\rm max}$ displaces the curve as a function of scale. In the middle panel we vary $n_1 = n_2 = n$ from -0.5 to 3.0 while $k_{\rm min} = 1$ and $k_{\rm max} = 500$ are fixed. Fields with exponents between -0.5 and 1 show similar profiles. There is a notorious degeneracy between curves with low exponents. Finally, in the bottom panel, we vary k_c from $k_{\rm min}$ to $k_{\rm max}$ while $k_{\rm min} = 1$, $k_{\rm max} = 500$, n_1=1.0, n_2=2.5 are fixed values. Changing k_c has a similar behavior to changing $k_{\rm max}$, at least for the exponents used here.

The next step is to illustrate the differences between the circulation that is originated from a GRF and the circulation from a circular velocity field. We begin by creating circular velocity fields that follow

$$\vec{v}_{\rm rot}(R) = R\Omega(R)\hat{\phi} \quad ; \quad \Omega(R) \propto (R + r_0)^{-\beta},$$
$$\omega_{\rm rot}(R) \propto (R + r_0)^{-\beta-1}[(2 - \beta)R + 2r_0].$$

Circular velocity fields are computed over a 2000×2000 grid with a size $L = 1$, and we choose $r_0 = 1/2000$, i.e. equal to the size of a resolution element. We start by computing the circulation from the circular velocity fields, $\gamma_{\rm rot}$, with $\beta \in (0, 0.5, 1, 1.5)$. We show the 16th, 50th and 84th percentiles of the circulation $\gamma_{\rm rot}$ in the top-left panel of Figure 3.6. We have normalized the values of $\gamma_{\rm rot}$ such that the mean value of $\gamma_{\rm rot}$ equals 1 at the highest resolution. For solid rotation, β=0, the distribution of $\gamma_{\rm rot}$ is single-valued. For other values of β, each percentile converges to an specific value at small ℓ. Since $\Omega(R)$ is a decreasing function of R, each percentile corresponds to $\gamma_{\rm rot}$ measured along a unique radius in the field. It is important to notice that for these models $\gamma_{\rm rot}$ is always positive. Variations at large scale are due to low sampling, e.g, at $\ell = L/2$ there are only 4 elements.

Now we create different Gaussian random vorticity fields, that can be added to $\gamma_{\rm rot}$. These models are described by $\mathcal{V}(k)$ in equation 4.8, and its parameters are shown in Table 3.1. From these random vorticity fields we obtain $\gamma_{\rm nc}$ for each model. We normalize $\gamma_{\rm nc}$ fields such that their variance $\sigma_\gamma^2 = 1$ at the highest resolution. Models 1 and 2 show similar distributions as a function of ℓ. As seen before in Figure 3.6, at low values of the exponent n the distribution of $\gamma_{\rm nc}$ does not depend strongly on n. Model 3, a single power law from $k \in [4, 64]$, lies close to model 5 which corresponds to a broken power law with $k_c = 64$. The only difference between these two models is the behavior of $\mathcal{V}(k)$ for values of $k > 64$: for Model 3, at $k > 64$,

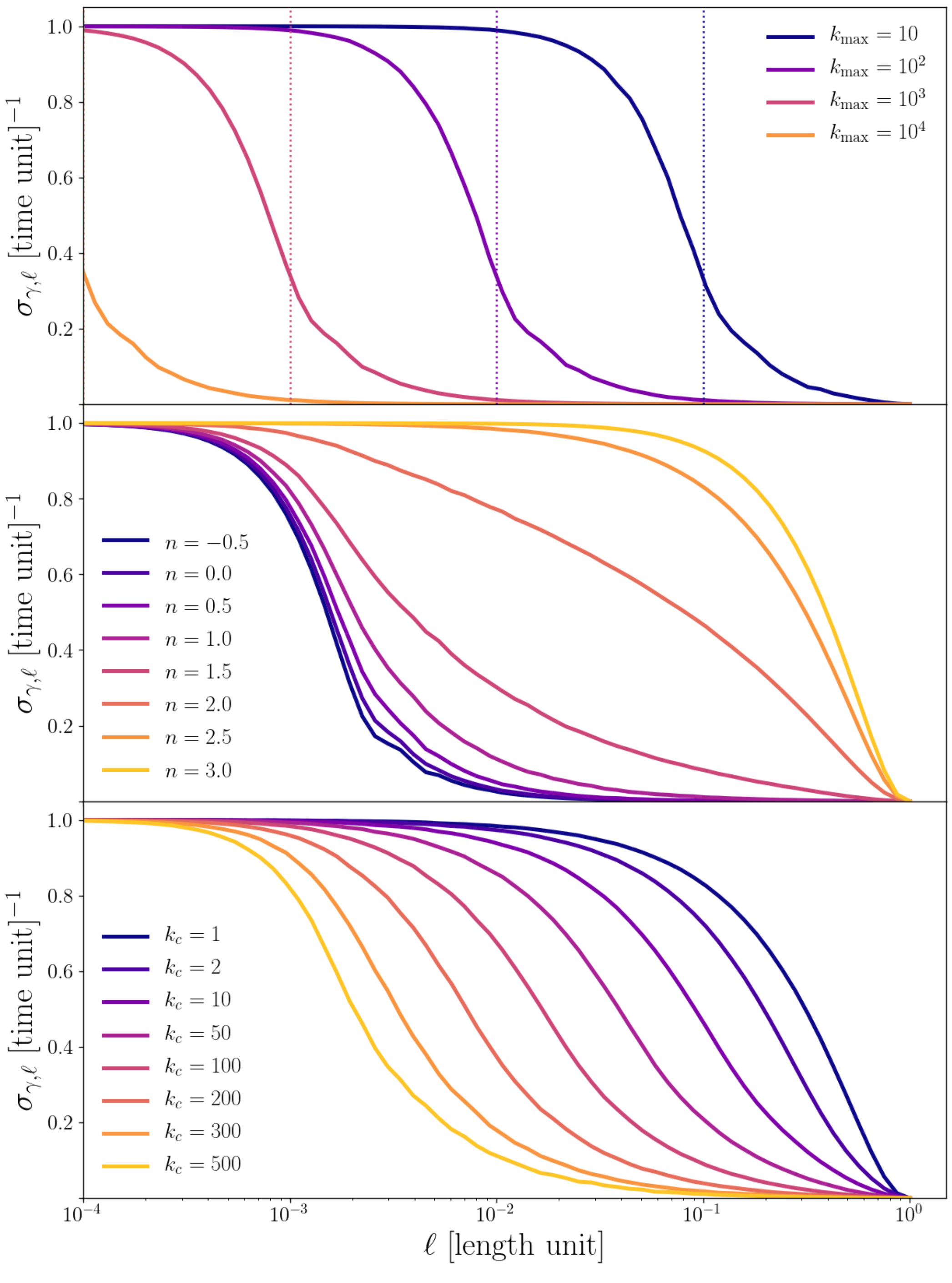

Figure 3.5: Dispersion of the distribution of $\gamma(\vec{r}, \ell)$ as a function of spatial scale. *Left*: The parameters n_1 and n_2 are fixed to zero, and $k_{\text{min}} = 1$. The parameter k_{max} is varied between the values $k_{\text{max}} \in [10, 10^2, 10^3, 10^4]$. *Middle*: We fix the parameters $k_{\text{min}} = 1$ and $k_{\text{max}} = 500$. The parameters n_1 and n_2 are equal to $n_1 = n_2 = n$, which corresponds to a function $\mathcal{V}(k)$ with a single power-law. The parameter n takes values from the set $[-0.5, 0.0, 0.5, 1.0, 1.5, 2.0, 2.5, 3.0]$. *Right*: The fixed parameters are $k_{\text{min}} = 1$, $k_{\text{max}} = 500$, n_1=1.0, n_2=2.5. We vary the parameter $k_c \in [1, 2, 10, 50, 100, 200, 300, 500]$

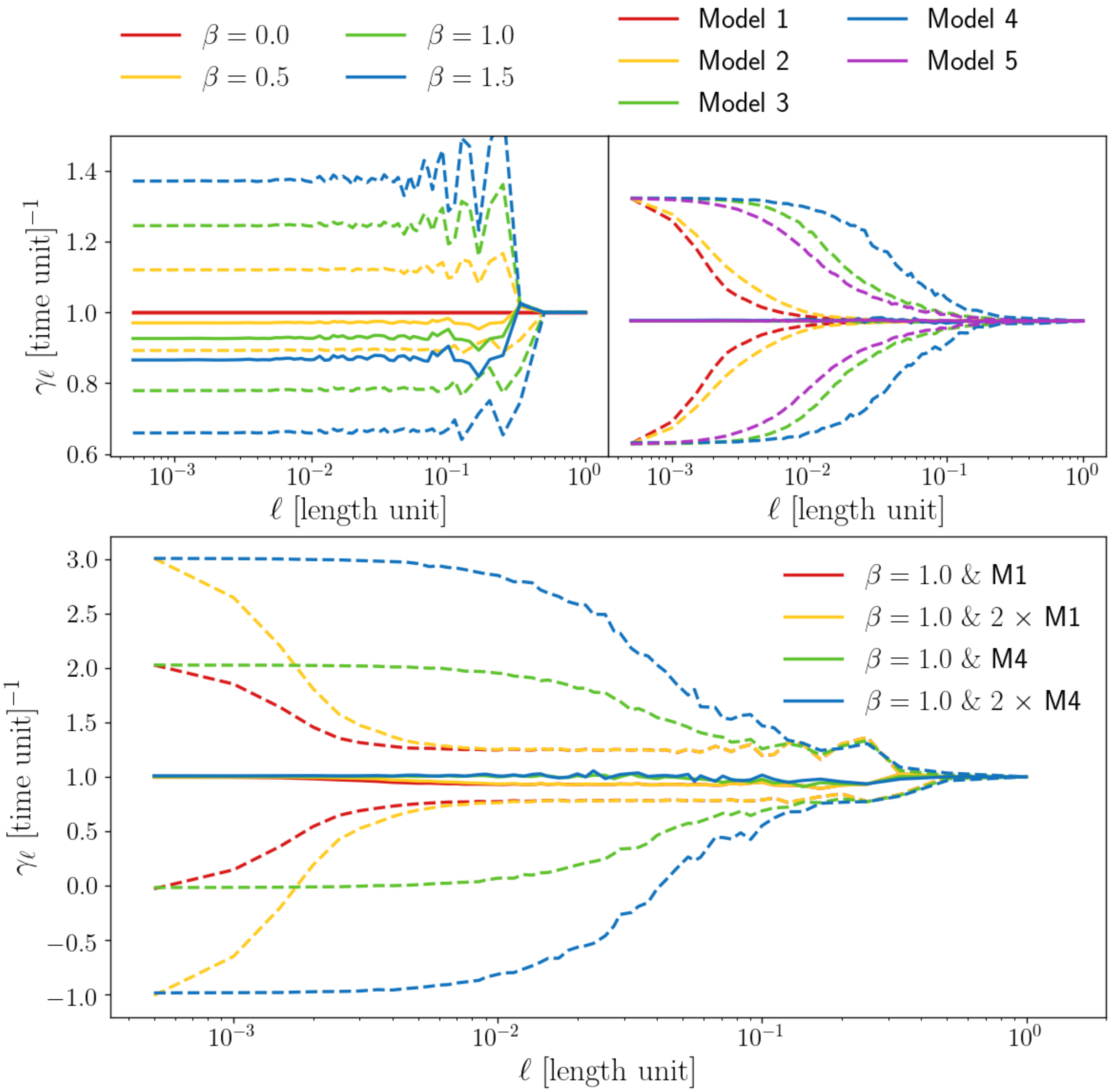

Figure 3.6: Percentiles of γ for coherent galactic rotation, $\gamma_{\rm rot}$, and for random velocity fields, $\gamma_{\rm nc}$ and different toy models. Each field has been computed in a 2000×2000 grid. *Left*: Solid lines show median values for $\gamma_{\rm rot}$ as a function of the scale ℓ, while dashed lines correspond to the 16th and 84th percentiles. *Middle*: Percentiles of $\gamma_{\rm nc}$ as a function of ℓ, for different models of Gaussian random fields defined in Table 3.1. Dashed lines show the 16th and 84th percentiles which correspond to 1σ uncertainties for $\gamma_{\rm nc}$. Solid lines show the median values of $\gamma_{\rm nc}$. *Right*: Percentiles of toy models for $\gamma_{\rm rot} + \gamma_{\rm nc}$. The model of $\gamma_{\rm rot}$ has $\beta = 1$ for the four lines. The red and green lines correspond to $\gamma_{\rm rot}$ plus Model 1 and Model 4 respectively. Yellow and blue lines have the same models for $\gamma_{\rm nc}$ but with twice the magnitude.

Table 3.1: Toy Models

Model	n_1	n_2	k_{min}	k_{max}	k_c
1	0.0	-	4	500	-
2	1.0	-	64	500	-
3	1.0	-	4	64	-
4	1.0	3.0	4	500	16
5	1.0	3.0	4	500	64

$\mathcal{V}(k) = 0$ which is equivalent to $n_2 = \infty$, while for model 5, $\mathcal{V}(k) \propto k^{-3}$. This shows that functions $\mathcal{V}(k)$ with high values of n_2 are similar to single power laws with $k_{\text{max}} = k_c$. The bottom panel of Figure 3.6 shows the distribution of 4 different composite models using a velocity field with $\beta = 1.0$ plus models 1 and 4 times a factor 1 or 2. Since model 1 changes mostly at small scales, for most of spatial scales the circulation is given by γ_{rot} until the width of both distributions is comparable. Then, if we increase the magnitude of the random field the transition where $\sigma_{\gamma_{\text{rot}}} \sim \sigma_{\gamma_{\text{nc}}}$ moves to larger scales as shown by the yellow dashed lines in Figure 3.6. It is important to mention that as we increase the magnitude of the random field the number of regions with negative circulation, i.e. with retrograde rotation with respect to the galaxy also increases.

Chapter 4

Algorithm and Code

In this chapter we explain how we obtained the dynamical information from the simulations, and how this is formations is processed and analyzed to get insights about the nature of the velocity field at different spatial scales. We also define relevant new physical spatial scales that define the problem of circulation according to our models.

4.1. The Principle

In this section we describe how we extract information from the normalized circulation field, γ, defined by equation 3.7. Hereafter, and for simplicity, we will refer to the *normalized circulation* simply as the *circulation* unless explicitly stated.

Let us imagine a two-dimensional fluid with velocity field $\vec{v}$. We assume that $\vec{v}$ can be composed by an ordered and smooth circular velocity field, $\vec{v}_{\rm rot}$, and a non-circular, random field, $\vec{v}_{\rm nc}$, i.e. $\vec{v} = \vec{v}_{\rm rot} + \vec{v}_{\rm nc}$, where

$$\vec{v}_{\rm rot}(R) = v_{\rm rot}(R)\hat{\phi}, \tag{4.1}$$

$$\omega = \frac{v_{\rm rot}(R)}{R}\left(1 + \frac{\partial \ln v_{\rm rot}(R)}{\partial \ln R}\right). \tag{4.2}$$

This gets translated into two components of the circulation field $\gamma = \gamma_{\rm rot} + \gamma_{\rm nc}$, since

$$\gamma^S = \frac{1}{A}\int \nabla \times \vec{v} \cdot {\rm d}\vec{S} = \frac{1}{A}\int \nabla \times (\vec{v}_{\rm rot} + \vec{v}_{\rm nc}) \cdot {\rm d}\vec{S} = \gamma^S_{\rm rot} + \gamma^S_{\rm nc}. \tag{4.3}$$

The superscript ^{S} means that these values correspond to an specific surface S. Through this work, these surfaces are defined by square regions of side ℓ, and surface area ℓ^2, for different positions in the (x, y) plane. Then γ is a function $\gamma(x, y, \ell)$.

For a fixed scale ℓ, we can measure the probability density distribution (pdf) of γ. The terms $\gamma_{\rm rot}$ and $\gamma_{\rm nc}$ behave differently as we show now. First, lets see how $\gamma_{\rm rot}$ behaves. The circulation $\gamma_{\mathrm{rot}}(x, y, \ell)$ is given by

$$\gamma_{\mathrm{rot}}(x, y, \ell) = \frac{1}{\ell^2} \int_{y-\frac{\ell}{2}}^{y+\frac{\ell}{2}} \int_{x-\frac{\ell}{2}}^{x+\frac{\ell}{2}} \omega_{\mathrm{rot}}(x', y')\mathrm{d}x'\mathrm{d}y' = \int_{-\frac{\ell}{2}}^{\frac{\ell}{2}} \int_{-\frac{\ell}{2}}^{\frac{\ell}{2}} \omega_{\mathrm{rot}}(x - x', y - y')\mathrm{d}x'\mathrm{d}y'. \tag{4.4}$$

We can write $\omega_{\mathrm{rot}}(x - x', y - y')$ as a Taylor expansion

$$\omega_{\mathrm{rot}}(x - x', y - y') = \omega_{\mathrm{rot}}(x, y) - \frac{\partial \omega_{\mathrm{rot}}(x, y)}{\partial x} x' - \frac{\partial \omega_{\mathrm{rot}}(x, y)}{\partial x} y' + ... \tag{4.5}$$

We assume that ω_{rot} is a smooth function, i.e. high order derivatives go to zero. Replacing equation 4.5 in equation 4.4 we get

$$\gamma_{\mathrm{rot}}(x, y, \ell) \approx \omega_{\mathrm{rot}}(x, y). \tag{4.6}$$

This shows that γ_{rot} is of the order of ω_{rot} across different scales ℓ. For the field γ_{nc} something different happens. Imagine that we choose a square region of size $\ell \times \ell$, and we divide it by $N \times N$ elements. We can approximate the integral that defines $\gamma_{\mathrm{nc}}(x, y, \ell)$

$$\gamma_{\mathrm{nc}}(x, y, \ell) = \frac{1}{\ell^2} \int \omega_{\mathrm{nc}}(x, y)\mathrm{d}S \approx \frac{1}{\ell^2} \sum_{i=1}^{N^2} \omega_{\mathrm{nc,i}} \frac{\ell^2}{N^2} = \frac{1}{N^2} \sum_{i=1}^{N^2} \omega_{\mathrm{nc,i}} = \langle \omega_{\mathrm{nc}} \rangle \tag{4.7}$$

If ω_{nc} is a continuous white noise field $\langle \omega_{\mathrm{nc}} \rangle = 0$. In real fluids, and for discrete velocity fields, there is a minimum size where the velocity field stops behaving as a random field. But for sufficiently large regions, large ℓ and consequently large N, $\langle \omega_{\mathrm{nc}} \rangle$ tends to zero. As we saw in section 3.1.5, if ω_{nc} is a Gaussian random field, the variance of γ_{nc} converges to zero for high values of ℓ.

From this discussion we can summarize that, at sufficiently large scales ℓ, the contribution from $\gamma_{\mathrm{nc}}(\ell)$ vanishes and pdf(γ) $\simeq$ pdf(γ_{rot}). On the other end, for small scales ℓ the contribution from $\gamma_{\mathrm{nc}}(\ell)$ increases while $\gamma_{\mathrm{rot}}(\ell)$ is about the same order. At small scales, the distribution of γ_{nc} gets broader, while the distribution of γ_{rot} converges to ω_{rot} given by equation 4.1. If the amplitude of pdf(γ_{nc}) is sufficiently high, it may occur that at small scales pdf(γ) is similar to pdf(γ_{nc}). We illustrate this point in Figure 4.2.

We create two maps, $\omega_{\mathrm{rot}}(x, y)$ and $\omega_{\mathrm{nc}}(x, y)$ with size $N \times N = 4000 \times 4000$. For ω_{rot} we assume a constant circular velocity field $v_{\mathrm{rot}} = v_0$, while ω_{nc} is a GRF, such that the Fourier transform of the velocity field, $\tilde{v}_{\mathrm{nc}}(k)$, obeys:

$$\tilde{v}_{\mathrm{nc}}(k) \propto \begin{cases} k^{-3/2} & \text{if } 8/L \leq k < 128/L \\ k^{-3} & \text{if } 128/L \leq k \leq 1000/L \\ 0 & \text{elsewhere} \end{cases} \tag{4.8}$$

We show both maps, $\omega_{\mathrm{rot}}(x, y)$ and $\omega_{\mathrm{nc}}(x, y)$, and their sum in the first row of Figure 4.2. For discrete maps, $\omega_{\mathrm{rot}}(x, y) = \gamma(x, y, \ell)$ when ℓ is equal to the resolution of the map. We can see that, at the level of the resolution of the images ($\ell = L/N$), $\gamma \simeq \gamma_{\mathrm{nc}}$ and the contribution from γ_{rot} is hard to notice. As we increase ℓ to $125L/N$ we can start to notice the contribution of γ_{rot} in the center of the map. For a scale $\ell = 400L/N$, γ is clearly dominated by γ_{rot}. This example shows how $\gamma(x, y, \ell)$ can transition from $\gamma \simeq \gamma_{\mathrm{nc}}$ at small scales to $\gamma \simeq \gamma_{\mathrm{rot}}$ at large scales.

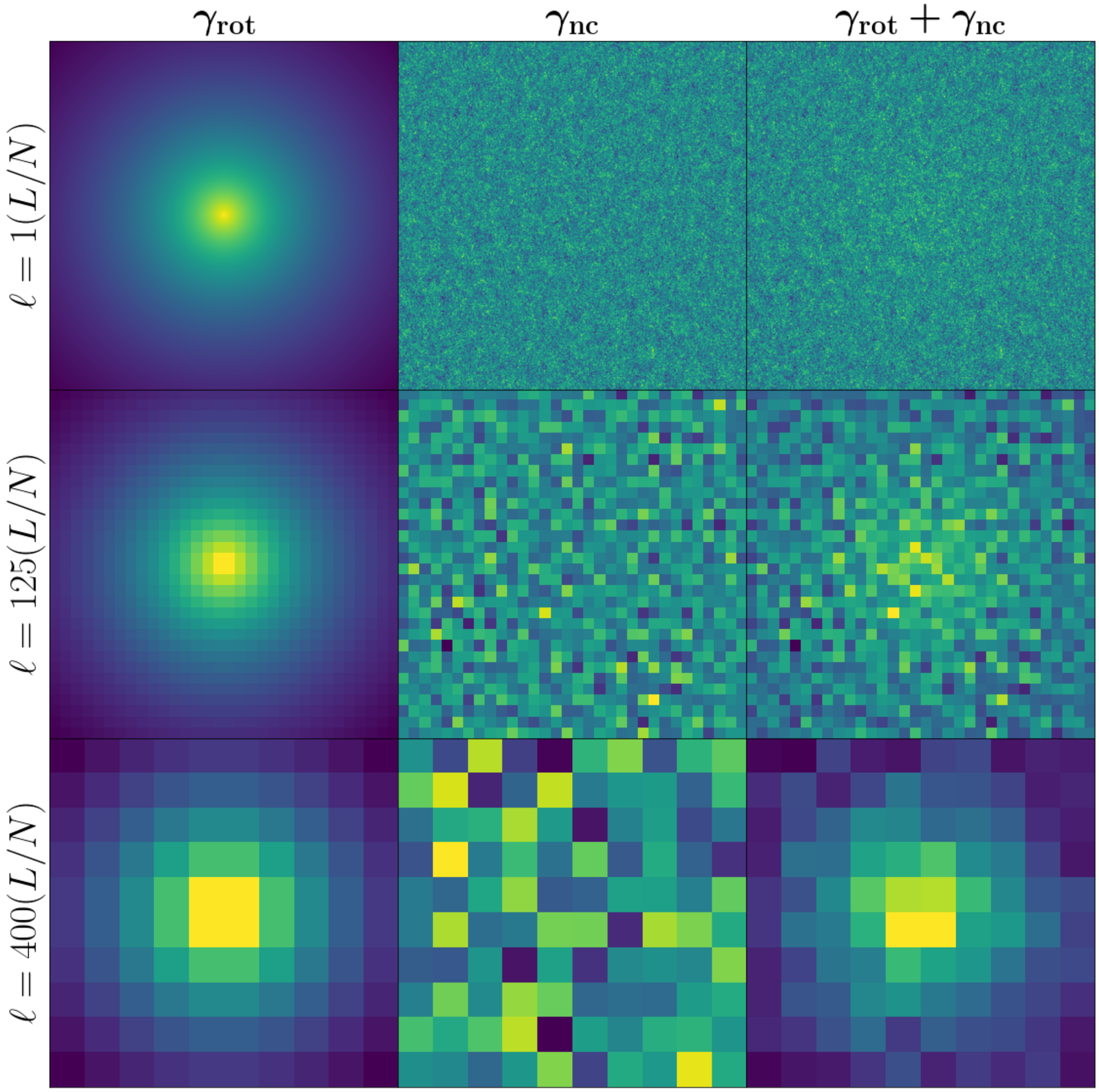

Figure 4.1: Circulation maps $\gamma_{\rm rot}$, $\gamma_{\rm nc}$ and $\gamma_{\rm rot} + \gamma_{\rm nc}$ for three different scales. We generate $\gamma_{\rm rot}$ assuming a constant velocity field, and $\gamma_{\rm nc}$ is a GRF generated by a broken power law in Fourier space with $n_1 = 3/2$, $n_2 = 3$, $k_{\rm min} = 8/L$, $k_{\rm max} = 1000/L$, and $k_{\rm c} = 128/L$ (see equation 4.8).The maps have a resolution of 4000×4000. From left to right, each column shows maps of $\gamma_{\rm rot}(x, y, \ell)$, $\gamma_{\rm nc}(x, y, \ell)$ and $\gamma_{\rm rot}(x, y, \ell) + \gamma_{\rm nc}(x, y, \ell)$ respectively. The first row shows maps with a scale $\ell = L/N$, equal to the resolution of the velocity fields. The middle and bottom row show maps where $\ell = 125L/N$ and $\ell = 400L/N$ respectively.

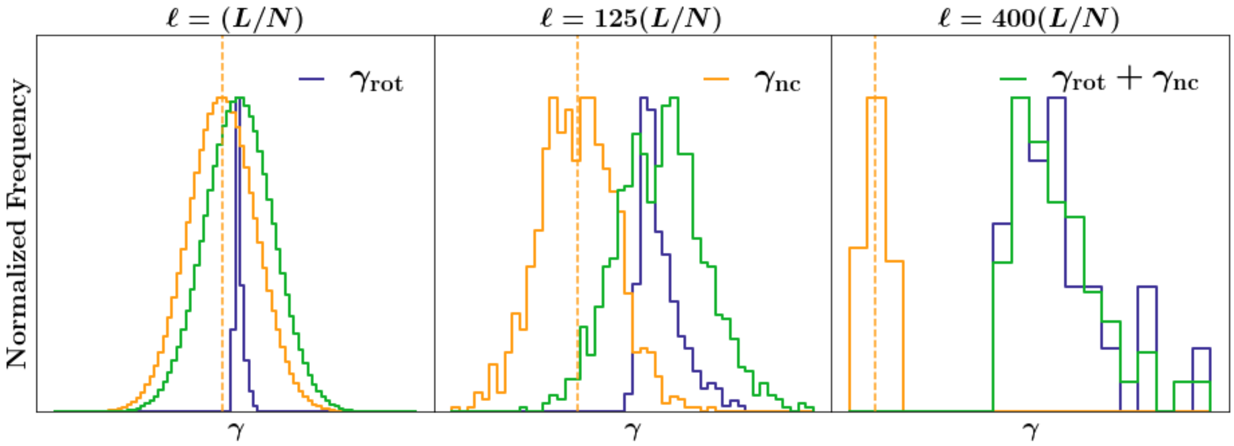

Figure 4.2: Histogram of circulation maps γ_{rot}, γ_{nc} and $\gamma_{\mathrm{rot}} + \gamma_{\mathrm{nc}}$, shown in Figure 4.1. From left to right, each panel shows the histograms of γ for $\ell = L/N$, $125L/N$, and $400L/N$. Blue, yellow and green lines correspond to γ_{rot}, γ_{nc}, and $\gamma_{\mathrm{rot}} + \gamma_{\mathrm{nc}}$ respectively.

4.1.1. The scale at which gas non-circular motions start to dominate

We have just seen an example where the circulation of gas can be dominated by non-circular or random motions at the smallest scales, and dominated by the large scale velocity field at large scales. If the amplitude of γ_{nc} is high enough, there must be scale $\ell = \lambda_{\mathrm{eq}}$ at which γ_{nc} and γ_{rot} contribute equally to the net circulation γ.

The scale λ_{eq} depends on the properties of γ_{rot}, and γ_{nc} which depend on the local dynamics of gas. For example, γ_{rot} in Figure 4.1 increases towards the center and its effects already can be seen at intermediate scales. Therefore, for that velocity field, the transition from γ being dominated by γ_{rot} to γ_{nc} occurs at smaller scales toward the center of the map. Hence, we expect λ_{eq} to depend on the position in the fluid.

Definition of λ_{eq}

Now that we have introduced the notion of the scale λ_{eq}, we need to choose a numerical definition. We start by defining the function $f_\gamma(\ell) = \sum \gamma^2_{\mathrm{nc},\ell} / \sum \gamma^2_{\mathrm{rot},\ell}$, that measures the ratio of the contributions of γ_{rot} and γ_{nc}. Then, λ_{eq} is given by the equation

$$f_\gamma(\lambda_{\mathrm{eq}}) = 1.0 \quad \text{with} \quad f_\gamma(\ell) = \frac{\sum \gamma^2_{\mathrm{nc},\ell}}{\sum \gamma^2_{\mathrm{rot},\ell}} \tag{4.9}$$

We compare their squared values since γ can have negative values. Additionally, comparing their square values is similar to comparing their total power.

For a random variable x with mean value μ_x and standard deviation σ_x, the expected value of $\sum x^2$ is $\mu_x^2 + \sigma_x^2$. We can rewrite $f_\gamma(\ell)$ as

$$f_\gamma(\ell) = \frac{\mu^2_{\gamma_{\rm nc}}(\ell) + \sigma^2_{\gamma_{\rm nc}}(\ell)}{\mu^2_{\gamma_{\rm rot}}(\ell) + \sigma^2_{\gamma_{\rm rot}}(\ell)} = \frac{\sigma^2_{\gamma_{\rm nc}}(\ell)}{\mu^2_{\gamma_{\rm rot}}(\ell) + \sigma^2_{\gamma_{\rm rot}}(\ell)} \tag{4.10}$$

where $\mu_{\gamma_{\rm nc}}$, $\mu_{\gamma_{\rm rot}}$, $\sigma_{\gamma_{\rm nc}}$, and $\sigma_{\gamma_{\rm rot}}$, are the mean values and standard deviations of $\gamma_{\rm nc}$ and $\gamma_{\rm rot}$ as a function of ℓ. For a region with constant $\omega_{\rm rot}$, $f_\gamma(\lambda_{\rm eq}) = 1.0$ is equivalent to the equation $\sigma_{\gamma_{\rm nc}}(\ell = \lambda_{\rm eq}) = \omega_{\rm rot}$.

4.2. Measuring circulation γ and $\gamma_{\rm rot}$

The aim is then to obtain the three fields, ω, $\omega_{\rm rot}$, and $\omega_{\rm nc}$, from our simulations. We can compute ω directly from the simulations. To get $\omega_{\rm rot}$ we need to choose how to model the smooth profile of the velocity field (i.e. the rotation curve). Finally, we model the random component by means of a function in Fourier space on the spatial coordinates. We have to point out that since we are computing the vorticity field for a discrete grid this field is also γ at the resolution level.

4.2.1. Two dimensional vorticity field

We calculate $\omega(x, y)$ as follows. First we compute the two dimensional velocity field averaging along the z-axis:

$$\vec{V}(x, y) = \frac{\int_{-z_0}^{z_0} \vec{v}(x, y, z)\rho(x, y, z)\mathrm{d}z}{\int_{-z_0}^{z_0} \rho(x, y, z)\mathrm{d}z}, \tag{4.11}$$

where ρ is the gas density, $\vec{v} = (v_x, v_y)$ are the x and y components of the three dimensional velocity field, and $\vec{V} = (V_x, V_y)$ is the reduced two-dimensional field. We choose $z_0 = 1$ kpc over the whole galactic plane. Then $\omega(x, y)$ is given by

$$\omega(x, y) = \frac{\partial V_y(x, y)}{\partial x} - \frac{\partial V_x(x, y)}{\partial y}. \tag{4.12}$$

Note that we are considering all the gas in $z \in$ [-1kpc,1kpc] to compute the integrated velocity fields, which is about 20 times the scale height of our simulated galaxies. We are not using a density threshold to integrate the velocity field. In observations, different tracers do not necessarily trace all the gas and are biased towards high density regions.

4.2.2. Smooth component

Since the definition of $\omega_{\rm rot}(R)$ involves radial derivatives we choose to parameterize $\omega_{\rm rot}$ by an analytic function. To get $\omega_{\rm rot}$ we fit a rotation curve of the form

$$V_{\rm rot}(R) = v_0 \arctan(R/R_1) \exp(-R/R_2), \tag{4.13}$$

to the circular velocity field, and we apply equation 2.2 to obtain $\omega_{\rm rot}$. The $\arctan(x)$ function provides a good fit to observed rotation curves (Courteau 1997), while the $\exp(-x)$ function recovers the decay of the rotation curve for our simulated galaxies. To fit the function in equation 4.13, we divide the disk in radial bins of width 500 pc. For each radial bin we have a pair velocity-uncertainty $(v_i, \delta v_i)$, where v_i is the median of the circular velocity and δv_i is half of the difference between the 84th and 16th percentiles of the circular velocity field. Finally, we perform a least-squares optimization to fit the rotation curve. The vorticity of the field $V_{\rm rot}(R)$ is

$$\omega_{\rm rot}(R) = v_0 \exp\left(-\frac{R}{R_2}\right)\left[\frac{R_1}{R_1^2 + R^2} + \arctan\left(\frac{R}{R_1}\right)\left(\frac{1}{R} - \frac{1}{R_2}\right)\right] \tag{4.14}$$

4.2.3. Differential component

Our main assumption is that we can separate the vorticity and circulation fields as

$$\omega(x,y) = \omega_{\rm rot}(x,y) + \omega_{\rm nc}(x,y) \quad \& \quad \gamma(x,y,\ell) = \gamma_{\rm rot}(x,y,\ell) + \gamma_{\rm nc}(x,y,\ell), \tag{4.15}$$

where x, and y are the spatial coordinates of the fields, and ℓ is the spatial scale at which circulation is being measured. The next step is to model the difference $\Delta\gamma(x,y,\ell) = \gamma(x,y,\ell)$-$\gamma_{\rm rot}(x,y,\ell)$. We can measure and model $\gamma(x,y,\ell)$ and $\gamma_{\rm rot}(x,y,\ell)$ from the simulations. We need to choose at which scales we compute both circulations and within what spatial domain.

We use $N_\ell = 40$ scales, $\ell \in [\ell_1, \ell_2, ..., \ell_{N\ell}]$, within $\ell_{\rm min}$ and $\ell_{\rm max}$. The smallest scale, $\ell_{\rm min}$ is equal to the spatial resolution of the simulations Δx. The maximum scale is chosen to be $\ell_{\rm max} \approx 5$ kpc. The scales between $\ell_{\rm min}$ and $\ell_{\rm min}$ are integers and quasi-logarithmic spaced. This means that we create logarithmic spaced intervals and we truncate them, skipping repeated intervals. We also bound the region of interest to a galactic radius of $R_{\rm max}$ =15 kpc, and only within this radius circulation is measured.

4.2.4. Computing γ

Once the vorticity maps ω, and $\omega_{\rm rot}$, from simulations are saved, we compute γ as follows:

1 We go over each cell of vorticity maps that lie within $R_{\rm max}$

2 We split the computation of γ on different processors. Each processor computes $\gamma(x,y,\ell)$ and $\gamma_{\rm rot}(x,y,\ell)$ for a subset of the points within the domain. We compute and save γ and $\gamma_{\rm rot}$ separately since it allows us to test different models for $\gamma_{\rm rot}$.

3 To numerically compute $\gamma(x,y,\ell)$ for different scales we do the following.
   - Since $\gamma = \int \omega {\rm d}S / \int {\rm d}S$ we can scale the area of each cell to different units. We choose that the area ${\rm d}A$ of each element on the vorticity maps equal to 1, ${\rm d}A = 1$. For each point we compute separately the sum $\Gamma_{i,j} = \sum \omega_{i,j} {\rm d}S_{i,j}$ and $A_{i,j} = \sum {\rm d}S_{i,j}$.
   - We compute $\Gamma^1_{i,j}$ at the point (i,j) at the resolution level. In this case, $\Gamma^1_{i,j} = \omega_{i,j}$.

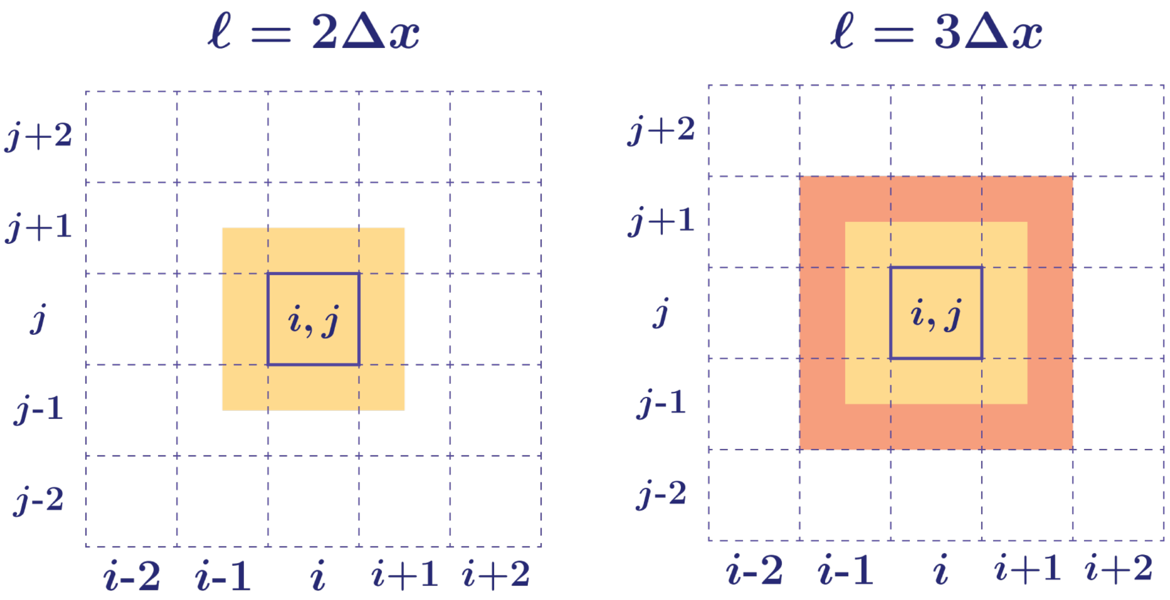

Figure 4.3: Illustration of the computation of γ. In the left panel we show the integrated area to compute γ centered at the cell (i, j) with a scale $\ell = 2\Delta x$. In the right panel, we show in orange the new area to be integrated to compute γ at the next scale $\ell = 3\Delta x$.

- We calculate $\Gamma^n_{i,j}$ and $A_{i,j}$ recursively. For the scale $\ell = (n+1)\Delta x$ we compute $\Gamma^{n+1}_{i,j} = \Gamma^n_{i,j} + \sum\limits_{\text{bound}} \omega_{i,j} \mathrm{d}S_{i,j}$ and $A^{n+1}_{i,j} = A^n_{i,j} + \sum\limits_{\text{bound}} \mathrm{d}S_{i,j}$, where $\sum\limits_{\text{bound}}$ is the summation along the boundary of the region as shown in the right panel of Figure 4.3. The values of $\mathrm{d}S_{i,j}$ on the corners have values $1/4$ or $3/4$ when $n+1$ is even or odd respectively. For the rest of the boundaries $\mathrm{d}S_{i,j} = 1/2$.
- If $\ell = (n+1)\Delta x \in [\ell_1, \ell_2, ..., \ell_{N\ell}]$ we save the values of $\Gamma^{n+1}_{i,j}$ and $A^{n+1}_{i,j}$.
- We get $\boldsymbol{\gamma}_{i,j} = \boldsymbol{\Gamma}_{i,j}/\boldsymbol{A}_{i,j}$. For each coordinate (i, j), we have an array of circulation values for different scales

$$\boldsymbol{\gamma}_{i,j} = [\gamma_{i,j}(\ell_1), \gamma_{i,j}(\ell_2), ..., \gamma_{i,j}(\ell_{N\ell})]. \tag{4.16}$$

- We also save the radius $R_{i,j}$ of each cell

4.3. The model for γ_{nc}

The next step is to define the model of γ_{nc} to compare it with the measured difference $\gamma - \gamma_{\text{rot}}$. Our model for γ_{nc} is a Gaussian random velocity field as described in section 3.1. The velocity field is defined by a function in Fourier space $\mathcal{V}(k)$ which for this thesis is given by the broken power law:

$$\mathcal{V}(k) \propto \begin{cases} k^{-n_1} & \text{if } 4/L \leq k < k_c \\ k^{-n_2} & \text{if } k_c \leq k \leq N/4L \\ 0 & \text{elsewhere} \end{cases} \tag{4.17}$$

where n_1 and n_2 are the exponents of the power law, L is the physical size of the vorticity map, N its resolution, and k_c is the critical wave number where $\mathcal{V}(k)$ breaks. By adding the constraint of continuity for $\mathcal{V}(k)$ at k_c, we need a parameter that sets the amplitude $V(k)$ to fully characterize this function. This parameter is the characteristic velocity dispersion of the random velocity field.

$$\sigma_0^2 = 2\pi \int_{k_{\min}}^{k_{\max}} \mathcal{V}(k)^2 k \mathrm{d}k. \tag{4.18}$$

To resume, the parameters defining the velocity field that originates γ_{nc} are $(n_1, n_2, k_c, \sigma_0)$.

We already now that γ_{rot} changes with galactic radius R. We expect that the properties of γ_{nc} also depend on the position on the galactic disk. As a first approximation for our work, we assume that its properties change with radius R. This is a good approximation for our simulations since they lack large scale structures that break the axisymmetry. Galaxies, simulated and observed, with structures like bars and spiral arms, γ_{rot} and γ_{nc} would have a significant dependence on the azimuthal angle ϕ.

We divide the galactic disks on nine radial annuli, 3 kpc wide, centered on 1.5, 3.0, 4.5, 6.0, 7.5, 9.0, 10.5, 12.0, and 13.5 kpc. As mentioned in section 4.2.4, we vary the scale ℓ from the resolution of the simulations 30 pc to around 5 kpc. Notice that ℓ can be larger than the width of a radial annulus. We might argue that within a radial annulus there is no information of scales larger than the width of the radial bin. However, the function $\mathcal{V}(k)$ has information about the correlation between two points in the velocity field, and within each radial annulus we can find points separated by distances larger than 3 kpc. The center of each square region of side ℓ is inside the 3 kpc annulus but it can cover cells outside the annulus. Information from neighbor regions will affect the values of the parameters within each annular region. This might smooth the resulting radial profiles of our model parameters.

In summary, our models for the dynamical fields are:

$$\begin{aligned}
V(x,y) &= V_{\text{rot}}(R) + V_{\text{nc}}(x,y; n_1(R), n_2(R), k_c(R), \sigma_0(R)) \\
\omega(x,y) &= \omega_{\text{rot}}(R) + \omega_{\text{nc}}(x,y; n_1(R), n_2(R), k_c(R), \sigma_0(R)) \\
\gamma(x,y) &= \gamma_{\text{rot}}(R) + \gamma_{\text{nc}}(x,y; n_1(R), n_2(R), k_c(R), \sigma_0(R)).
\end{aligned}$$

4.4. Deriving the parameter distributions

At each radial annuli, we are looking for the parameters n_1, n_2, k_c, and σ_0, that best represent the equation $\gamma = \gamma_{\text{rot}} + \gamma_{\text{nc}}$. However, for a given set of parameters, the field γ_{nc} is a random realization from a parent GRF and is not single-valued. This means that the expression $\gamma = \gamma_{\text{rot}} + \gamma_{\text{nc}}$ has to be looked as the sum of two distributions rather than the sum of two fields or images. Then, to look for parameters that can model our data we need to compare γ, γ_{rot}, and γ_{nc} as distributions. We choose to compare histograms of γ and $\gamma_{\text{rot}} + \gamma_{\text{nc}}$ as the final ingredient of our technique.

At each spatial scale ℓ we compare the distributions of γ and $\gamma_{\text{rot}} + \mathcal{N}(0, \sigma_\gamma)$ where $\mathcal{N}(0, \sigma_\gamma)$ is a random field with dispersion σ_γ. We are in fact, comparing the difference γ and γ_{rot} with

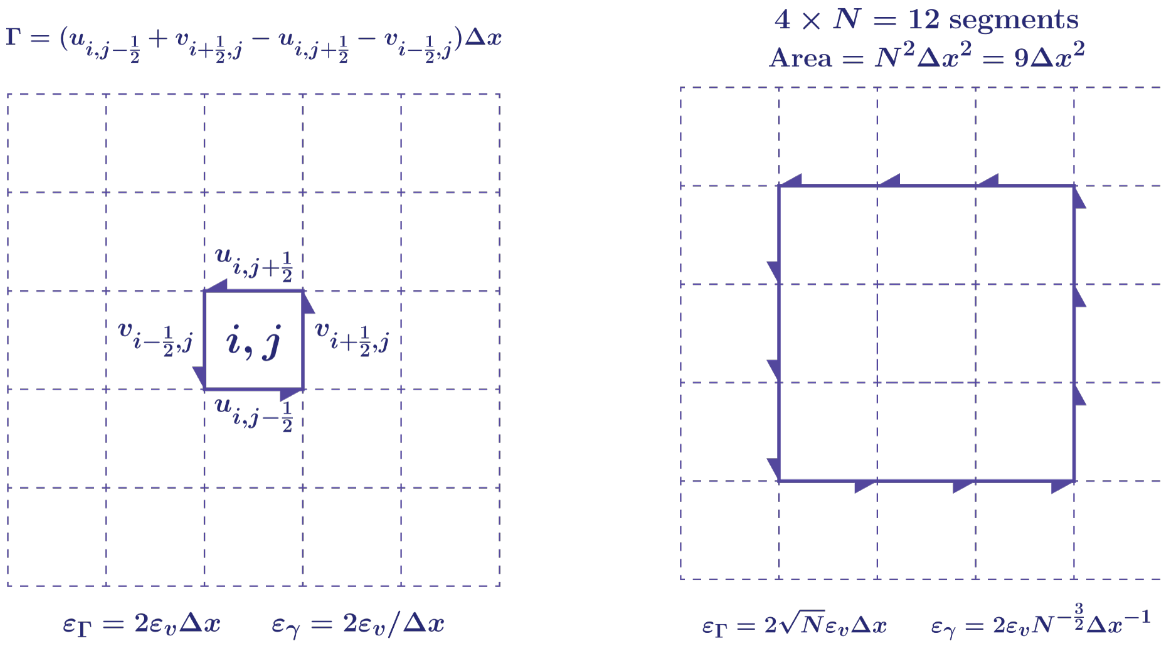

Figure 4.4: Illustration of the propagation of uncertainty for different scales. At the right we show the closed path used to compute γ with $\ell = \Delta x$, consisting on 4 elements. In the right panel, we show the closed path for a region with $\ell = N\Delta x$, with $N = 3$. This path has $4 \times N = 12$ elements.

a normal distribution. Therefore, we compute the histogram of $\Delta\gamma = \gamma - \gamma_{\mathrm{rot}}$.

To build the histograms and to compare them, we must choose the width of the bins, $\Delta\gamma$, and the uncertainty, ε_γ, for each measurement with their propagation in the histogram bins. For the bin width we choose a conservative criteria: 8 times the bin-width set by the Freedman-Diaconis rule (Freedman & Diaconis 1981), $\Delta\gamma = 16\ \mathrm{IQR}\ (\gamma)\ N^{-1/3}$ where $\mathrm{IQR}(\gamma)$ is the interquartile range of γ and N is the total number of data points. Freedman-Diaconis rule attempts to minimize the integrated mean squared difference of the histogram model and the true underlying density.

For the uncertainty in γ, we set an uncertainty of $\varepsilon_v = 1$ km/s in the measured velocity at the resolution of the simulation Δx (≈ 30 pc) which is comparable with the precision of recent gas velocity measurements on nearby galaxies (Druard et al. 2014; Caldú-Primo & Schruba 2016; Koch et al. 2018; Sun et al. 2018). To propagate the uncertainty we use equation 2.19. For a square region with area $\Delta x \times \Delta x$, i.e. at the maximum resolution, the circulation is the sum of the integral along the four faces of the square. This is illustrated in the left panel of Figure 4.4. For a cell at (i, j), $\Gamma = (u_{i,j-\frac{1}{2}} + v_{i+\frac{1}{2},j} - u_{i,j+\frac{1}{2}} - v_{i-\frac{1}{2},j})\Delta x$ and its uncertainty is $\varepsilon_\Gamma = \sqrt{4\varepsilon_v^2}\Delta x = 2\varepsilon_v\Delta x$. Since $\gamma = \Gamma/A$, its uncertainty is $\varepsilon_\gamma = 2\varepsilon_v/\Delta x$.

A square region of size $\ell = N\Delta x$ is delimited by $4N$ linear segments, N at each side. Then, Γ is the sum of $4N$ elements and its uncertainty is $2\sqrt{N}\varepsilon_v\Delta x$, while for γ is $2\sqrt{N}\varepsilon_v\Delta x/(N\Delta x)^2 = (2\varepsilon_v/\Delta x) \times N^{-3/2} = \varepsilon_\gamma N^{-3/2}$. The scaling of the uncertainty of γ with

N is not straightforward if we use equation 2.21. We have to recall that ω is the difference between two terms. If we add the vorticity of two neighbor cells we are also subtracting the line integral along the line that both regions share. For that reason, when we compute the uncertainty in γ for a region with $N \times N$ elements, we are adding $4N$ terms instead of $N \times N$.

The histogram counts of our distributions have Poisson noise, i.e. and uncertainty of $\sqrt{h_j} = \sqrt{N_j}$, where N_j is the number of data points lying in th j-th bin. We also have to propagate the uncertainties in ε_γ into the histogram. Let us consider the j-th bin with endpoints $[l_j, u_j]$ and a data point with value γ_i with uncertainty ε_i. Assuming that γ_i is the mean value of a Gaussian random variable with standard deviation ε_i the probability p_{ij} that this data point lies within $[l_j, u_j]$ is

$$p_{ij} = \frac{1}{2}\left[\mathrm{erf}\left(\frac{u_j - \gamma_i}{\sqrt{2}\varepsilon_i}\right) - \mathrm{erf}\left(\frac{l_j - \gamma_i}{\sqrt{2}\varepsilon_i}\right)\right], \tag{4.19}$$

where erf is the error function. Each bin acts like a Bernoulli random variable: we add 1 if the measurement lies in the bin or zero otherwise, with a probability p_{ij} and $1-p_{ij}$ respectively. The variance for the Bernoulli distribution is $p_{ij}(1-p_{ij})$. Then the total variance in the j-th bin due to the uncertainties in γ is $\sigma^2_{h_j} = \sum_i^N p_{ij}(1-p_{ij})$.

At this point we have built a histogram distribution of $\Delta\gamma = \gamma - \gamma_{\mathrm{rot}}$ at each scale ℓ. We fit a Normal distribution $\mathcal{N}(0, \sigma_\gamma)$ using the least-squares method. This step creates an array $\sigma_\gamma(\ell)$ as a function of ℓ with its respective uncertainty ε_σ.

4.5. Markov Chain

Now that we have defined how to compute σ_γ from simulations, we need to explore the parameter space $\boldsymbol{\theta} = (n_1, n_2, k_c, \sigma_0)$ of the function $\mathcal{V}(k)$. Each parameter vector $\boldsymbol{\theta}$ defines a different curve $\sigma_{\gamma_{\mathrm{nc}}}(\ell, \boldsymbol{\theta})$. To find the posterior distributions of $\boldsymbol{\theta}$ given our data $\mathbf{D}$, i.e. $P(\boldsymbol{\theta}|\mathbf{D})$ we use the Bayes' theorem:

$$P(\boldsymbol{\theta}|\mathbf{D}) = \frac{P(\mathbf{D}|\boldsymbol{\theta})P(\boldsymbol{\theta})}{P(\mathbf{D})}. \tag{4.20}$$

In this equation, $P(\mathbf{D}|\boldsymbol{\theta})$ is the the likelihood to obtain $\mathbf{D}$ that in our case corresponds to the array $\sigma_\gamma(\ell)$. Our likelihood is given by

$$P(\mathbf{D}|\boldsymbol{\theta}) = \prod_\ell \frac{1}{\sqrt{2\pi}\varepsilon_\sigma} \exp\left(\frac{-(\sigma_\gamma(\ell) - \sigma_{\gamma_{\mathrm{nc}}}(\ell, \boldsymbol{\theta}))^2}{2\varepsilon_\sigma^2}\right), \tag{4.21}$$

$P(\boldsymbol{\theta})$ is our prior knowledge of the parameters. We assume uniform prior distributions for each parameter with $n_1 \in [n_{1,\mathrm{min}}, n_{1,\mathrm{max}}]$, $n_2 \in [n_{2,\mathrm{min}}, n_{2,\mathrm{max}}]$, $k_c \in [k_{c,\mathrm{min}}, k_{c,\mathrm{max}}]$, and $\sigma_0 \in [\sigma_{0,\mathrm{min}}, \sigma_{0,\mathrm{max}}]$. $P(\mathbf{D})$ is the Bayesian evidence of the data which ensures proper normalization.

We can compare different models $\boldsymbol{\theta}_1$ and $\boldsymbol{\theta}_2$ by comparing their posterior probabilities given the data:

$$r = \frac{P(\boldsymbol{\theta}_2|\mathbf{D})}{P(\boldsymbol{\theta}_1|\mathbf{D})} = \frac{P(\mathbf{D}|\boldsymbol{\theta}_2)P(\boldsymbol{\theta}_2)}{P(\mathbf{D}|\boldsymbol{\theta}_1)P(\boldsymbol{\theta}_1)}. \tag{4.22}$$

To sample the posterior distributions we use Markov Monte Carlo methods. Specifically we use the Metropolis within Gibbs scheme shown in Algorithm 4.5. The function

Algorithm 1 Metropolis-within-Gibbs Algorithm

```
Input: Starting point $\theta_0$, function $f(\theta)$, transition kernel $q(y|x)$
Output: An array of points $\boldsymbol{\theta}_0, \boldsymbol{\theta}_1, ..., \boldsymbol{\theta}_N$, with $\boldsymbol{\theta} = (\theta^1, ..., \theta^{\mathrm{d}})$
for $t = 1$ to $N$ do
    for i = 1 to d do
        Generate $\theta^i_\star$ from $q_{\mathrm{i}}(\theta^i|\theta^1_{t+1}, ..., \theta^{i-1}_{t+1}, \theta^{i+1}_t, ..., \theta^{\mathrm{d}}_t)$
        Calculate $r = \frac{f(\theta^i_\star|\theta^1_{t+1},...,\theta^{i-1}_{t+1},\theta^{i+1}_t,...,\theta^{\mathrm{d}}_t)}{f(\theta^i_t|\theta^1_{t+1},...,\theta^{i-1}_{t+1},\theta^{i+1}_t,...,\theta^{\mathrm{d}}_t)} \frac{q_i(\theta^i_t|\theta^1_{t+1},...,\theta^{i-1}_{t+1},\theta^{i+1}_t,...,\theta^{\mathrm{d}}_t)}{q_i(\theta^i_\star|\theta^1_{t+1},...,\theta^{i-1}_{t+1},\theta^{i+1}_t,...,\theta^{\mathrm{d}}_t)}$
        Sample a uniform random variable $U$
        if $U < r$ then $\theta^i_{t+1} = \theta^i_\star$
        else $\theta^i_{t+1} = \theta^i_t$
    end for
end for
```

$f(\theta^i_\star|\theta^1_{t+1}, ..., \theta^{i-1}_{t+1}, \theta^{i+1}_t, ..., \theta^{\mathrm{d}}_t)$ is the conditional probability of getting the i-th parameter equal to $\theta^i_\star$, given that the other parameters remain unchanged. For example, if we want to compare a proposed step to from $k_{c,t}$ to $k_{c,\star}$ we need to compare:

$$r = \frac{P((n_{1,t+1}, n_{2,t+1}, k_{c,\star}, \sigma_{0,t})|\mathbf{D})}{P((n_{1,t+1}, n_{2,t+1}, k_{c,t}, \sigma_{0,t})|\mathbf{D})} \frac{q_{k_c}(k_{c,t}|n_{1,t+1}, n_{2,t+1}, \sigma_{0,t})}{q_{k_c}(k_{c,\star}|n_{1,t+1}, n_{2,t+1}, \sigma_{0,t})}. \tag{4.23}$$

The function $q(y|x)$ is the transition kernel or proposal distribution that samples the proposed step from x to y. In this work the transition function is:

$$q(\boldsymbol{\theta}_2|\boldsymbol{\theta}_1) = \prod_i^4 \frac{1}{\sqrt{2\pi}\sigma_{\theta_i}} \exp\left(-\frac{(\theta_{i,\mathit{2}} - \theta_{i,\mathit{1}})^2}{2\sigma^2_{\theta_i}}\right). \tag{4.24}$$

Since $q(\boldsymbol{\theta}_2|\boldsymbol{\theta}_1) = q(\boldsymbol{\theta}_1|\boldsymbol{\theta}_2)$ the ratio r is reduced to

$$r = \frac{f(\theta^i_\star|\theta^1_{t+1}, ..., \theta^{i-1}_{t+1}, \theta^{i+1}_t, ..., \theta^{\mathrm{d}}_t)}{f(\theta^i_t|\theta^1_{t+1}, ..., \theta^{i-1}_{t+1}, \theta^{i+1}_t, ..., \theta^{\mathrm{d}}_t)}. \tag{4.25}$$

We need to choose the values for σ_{θ_i}. To do this we do the following. During the first 1000 steps of the Markov chain, we compute the ratio r using the tempered probabilities:

$$r = \frac{P(\mathbf{D}|\boldsymbol{\theta}_2)^\beta P(\boldsymbol{\theta}_2)}{P(\mathbf{D}|\boldsymbol{\theta}_1)^\beta P(\boldsymbol{\theta}_1)}, \tag{4.26}$$

with $\beta = ((t-1)/1000)^{1/2}$, where t is the number step in the chain. For the first steps of the chain, $r \approx P(\boldsymbol{\theta}_2)/P(\boldsymbol{\theta}_1)$ and the new points are almost sampling the prior distribution. As t increases the posterior probability converges to the desired distribution. For $t > 1000$ we set $\beta = 1$. At each step we update the mean μ and standard deviation s values for each parameter θ using

$$\mu_{t+1} = \frac{t\mu_t + \theta_{t+1}}{t+1} \tag{4.27}$$

$$s^2_{t+1} = \frac{t}{t+1}s^2_t + \frac{t}{(t+1)^2}(\theta_{t+1} - \mu_t)^2. \tag{4.28}$$

At the start of the chain we set $\mu_0 = \frac{1}{2}(\theta_{\text{min}} + \theta_{\text{max}})$, $s_0 = \frac{1}{2}(\theta_{\text{max}} - \theta_{\text{min}})$, and the first step is draw from the prior distribution.

At each step we set the standard deviations of the transition kernel by $\sigma_{\theta,i} = \frac{1}{2}s_{t,i}$. The factor $\frac{1}{2}$ has two reasons: (i) the optimal step size for Gaussian posteriors is $\sigma_{\text{jump}} = 2.38\sigma_{\text{posterior}}/\text{d} = 0.595\sigma_{\text{posterior}}$, and (ii) $s_{t,i}$ overestimates the standard deviation of the posterior distribution due to the first steps. For this reason, we also add 4000 initial steps to let $\sigma_{\theta,i}$ converge closer to its optimal value. With these steps we get an acceptance rate around 0.2 and 0.3.

We use 72 random walkers that follow this algorithm. Each random walker creates a chain with 10000 values of $\boldsymbol{\theta}$ after the first 5000 that are used for the convergence of the sampling algorithm. Once we have samples of $\boldsymbol{\theta} = (n_1, n_2, k_c, \sigma_0)$ we can reconstruct the PDFs of the model parameters. These samples also establish the parent distribution of γ_{nc}.

4.5.1. Computing $\sigma_{\gamma_{\text{nc}}}$

For one of the steps of this algorithm we need to compute $\sigma_{\gamma_{\text{nc}}}(\ell, \boldsymbol{\theta})$. As discussed in section 3.1.4, we compute $\sigma_{\gamma_{\text{nc}}}(\ell, \boldsymbol{\theta})$ numerically through equation 3.1.4. Instead of performing a numerical integration of $\sigma_{\gamma_{\text{nc}}}(\ell, \boldsymbol{\theta})$ at each step of the chain we create a grid of 72^3 values in the (n_1, n_2, k_c) space over which we pre-tabulate the integral. The parameter σ_0 works as the normalization of $\mathcal{V}(k)$ and can be handled independently. The intervals chosen to create the grid are $n_1 \in (0.8, 2.5)$, $n_2 \in (2.0, 20.0)$, and $k_c \in (2k_{\text{min}}, k_{\text{max}}/2)$. For n_1 and n_2 we use linear spacing while for k_c we use a logarithmic spacing to create the grids.

Chapter 5

Simulations

To test if circulation is a useful tool to find the transition scale between galactic rotation and non-circular motions, we use hydrodynamical simulations of galactic disks with different initial conditions. Numerical simulations are an excellent testbed for the study of circulation since they provide the full velocity field, and allow us to look for observable signatures by changing different physical parameters, such as rotation or self-gravity.

We create a set of simulated galaxies using the adaptive mesh refinement code Enzo (Bryan et al. 2014). The simulations are evolved in comoving coordinates in a ΛCDM universe from a redshift $z = 0.2$, where we have adopted the values $\Omega_m = 0.3$, $\Omega_\Lambda = 0.7$, and $\mathrm{H}_0 = 67\,\mathrm{km\,s^{-1}Mpc^{-1}}$. We run three simulations in a box of 483.35 kpc with periodic boundary conditions. For a disk of 50 kpc in diameter, the box size is around ten times larger, that ensures that the simulated galaxy is not greatly affected by the boundary conditions. The size of the parent grid is 128^3, that corresponds to a coarse resolution of 3.7 kpc. We add 7 levels of refinement that translates in a maximum resolution of 29.5 pc.

We use two criteria to refine a given gas cell, and both criteria have to be fulfilled: refinement by baryon mass and Jeans length.

- **Baryon Mass:** This refinement criterion refines a cell if the cell baryonic mass m_{cell} is larger than:
  $$m_{\mathrm{cell}} > m_0 r^{\alpha l} \tag{5.1}$$
  where m_0 is the maximum mass for refinement at the root grid level, r is the refinement factor, l is the refinement level, and α defines how the mass threshold changes at each level. For $\alpha = 0$ this method gives a constant mass threshold for every level. In our simulations $\alpha = 0$, and $m_0 = 8518.58 M_\odot$.
- **Jeans length:** In order to prevent artificial fragmentation, we refine gas cells such that the Jeans length is resolved by a number of cells N_J (Truelove et al. 1998). This is translated into the following criterion:
  $$\Delta x \left(\frac{\pi k_B T}{N_J^2 G \rho m_H} \right)^{1/2} \tag{5.2}$$
  We use $N_J = 4$ following Truelove et al. (1997).

During the first 500 Myr, we use only 6 levels of refinement, with an effective resolution of 59 pc until a quasi-steady state is reached. Then the resolution is increased to 30 pc for the following 200 Myr. Over 80 % of the mass in gas cells is found at the highest resolution.

5.1. Initial conditions

The simulated galaxies are modeled as four-component systems that include gas, stars particles, a stellar potential and dark matter (DM). In the case of gas, we model it using grids, while the stellar potential and DM are represented by external potentials. Star particles form from gas cells and are not added at the beginning of the simulations.

5.1.1. Gas

The gas is initially set as a rotation-supported disk, with an initial density profile described by an exponential radial profile, and the vertical density initially follows a sech^2 profile:

$$\rho_{\rm gas} = \rho_0 \exp\left(-\frac{R}{R_0}\right) {\rm sech}^2\left(\frac{z}{2z_0}\right), \tag{5.3}$$

where R_0 is the disk scale length of 3.5 kpc, and z_0 is the disk scale height of 0.4 kpc. The total gas mass for this profile is

$$M_{\rm gas} = 8\pi z_0 R_0^2 \rho_0. \tag{5.4}$$

5.1.2. Stars

To model the stellar potential we use a Miyamoto-Nagai profile (Miyamoto & Nagai 1975), which models the stellar disk and bulge of a galaxy. The stellar potential is given by

$$\Phi_\star(R,z) = -\frac{GM_\star}{\sqrt{R^2 + (a + \sqrt{z^2+b^2})^2}}, \tag{5.5}$$

where $M_\star$ is the total stellar mass of the field, and a and b are characteristic length scales. When $a = 0$, the potential is equivalent to the Plummer's spherical potential (Plummer 1911). We adopt the values $a = 5$ kpc and $b = 200$ pc, which are similar to the fitted values for the stellar disk of the Milky Way (Kafle et al. 2014).

We add this potential field in Enzo as an acceleration vector field $\vec{a}_\star = a_R \hat{R} + a_z \hat{z}$, given by

$$a_R = -\frac{\partial \Phi_\star}{\partial R} = -\frac{GM_\star R}{(R^2 + (a + \sqrt{z^2+b^2})^2)^{3/2}} \tag{5.6}$$

$$a_z = -\frac{\partial \Phi_\star}{\partial z} = -\frac{GM_\star z}{(R^2 + (a + \sqrt{z^2+b^2})^2)^{3/2}} \frac{a + \sqrt{z^2+b^2}}{\sqrt{z^2+b^2}}. \tag{5.7}$$

5.1.3. Dark Matter

The dark matter potential is described by the Navarro-Frenk-White profile (Navarro et al. 1997) given by

$$\Phi_{NFW}(r) = \frac{\rho_{c_{\rm DM}}\delta_c}{(r/r_s)(1+r/r_s)^2}, \tag{5.8}$$

where $r_s = r_{200}/c_{\rm DM}$ is a characteristic radius, $\rho_c = 3H^2/8\pi G$ is the critical density, $c_{\rm DM}$ is the concentration parameter, and δ_c is defined

$$\delta_c = \frac{200}{3}\frac{c_{\rm DM}^3}{\ln(1+c_{\rm DM}) - c_{\rm DM}/(1+c_{\rm DM})}. \tag{5.9}$$

The characteristic radius r_{200} corresponds to the volume at which the mean density within r_{200} is 200 time the critical density, i.e.

$$M_{200} = 200\rho_c\frac{4\pi}{3}r_{200}^3. \tag{5.10}$$

We adopt a value $c_{\rm DM} = 21$ for $M_{200} = 8\times10^{11}M_\odot$ and $c_{\rm DM} = 26.45$ for $M_{200} = 4\times10^{11}M_\odot$. The values for the initial conditions of our simulations are summarized in Table 5.1. In our nomenclature G stands for the amount of gas and E for the relative magnitude of the external potential.

Table 5.1: Simulation parameters

Run	$M_{\rm gas}$	$M_\star$	M_{200}
	$M_\odot$	$M_\odot$	$M_\odot$
G2E1	2×10^{10}	1×10^{11}	8×10^{11}
G1E1	1×10^{10}	1×10^{11}	8×10^{11}
G1E0.5	1×10^{10}	5×10^{10}	4×10^{11}

5.2. Radiative cooling

An accurate treatment of the cooling produced by the metal content requires taking into account several transitions and chemical reactions, which translates in a higher consumption of computational resources. Most metal cooling methods rely on assumptions on the subgrid physics in order balance accuracy and speed. For this reason, we employ the simplest cooling method available in Enzo, that consists in using the analytic cooling function of Sarazin & White (1987), which assumes a fully ionized gas with a constant metallicity of $0.5Z_\odot$. This allow the gas to radiative cool down to 10^4 K. We add the cooling curves defined in Rosen & Bregman (1995) to cool the gas down to 300 K, that assume a fully ionized gas of solar metallicity. This imposes a minimum value for the Jeans scale λ_J. For a surface density of $10M_\odot\text{pc}^{-2}$ and a temperature $T = 300$ K, λ_J is of the order of 100 pc. This means that overdensities in our simulations are more representative of HI clouds.

5.3. Star formation

Our recipe of star formation follows the Cen & Ostriker (1992) algorithm, which assumes that stars are formed in overdense, converging and gravitationally unstable regions of gas. In order to create a star particle from a gas cell, the following criteria must be fulfilled: (i) the number density n exceeds a density threshold $n_{\rm thres}$, (ii) the velocity flow is converging (collapse), (iii) the cooling time is shorter than the local free-fall time, (iv) the gas mass in the cell is greater than the Jeans mass, and (v) the resulting particle has at least a mass $m_{\rm min}$. These criteria are numerically given by

$$n_{\rm cell} > n_{\rm thres} = 100 {\rm cm}^{-3} \tag{5.11}$$

$$\nabla \cdot \vec{v} < 0 \tag{5.12}$$

$$t_{\rm cool} < t_{\rm dyn} \equiv \sqrt{\frac{3\pi}{G\rho}} \tag{5.13}$$

$$m_{\rm cell} > m_J \equiv \frac{4\pi}{3}\left(\frac{\lambda_J}{2}\right)^3 \tag{5.14}$$

$$m_\star > m_{\rm min}. \tag{5.15}$$

If these criteria are satisfied a star particle is formed with a mass equal to $m_\star = \epsilon_{\rm SF}\ m_{\rm cell}$, where $\epsilon_{\rm SF}$ is the numerical star formation efficiency. We adopt the value $\epsilon_{\rm SF} = 0.1$.

5.4. Stellar Feedback

We include stellar feedback that can be divided in two groups: (i) early stellar feedback in the form of radiation and stellar winds, (ii) and late feedback given by SNe explosions. SNe feedback alone is not able to regulate star formation in galaxies (Girichidis et al. 2016) and fails to reproduce some galactic properties (Hopkins et al. 2014). Early stellar feedback is relevant since it can disperse clouds before the explosions of the first supernova (Murray et al. 2010; Walch et al. 2012), and reduces the ambient density in which supernovae explode (Kannan et al. 2020). To compute the energy or momentum injection as a function of time, for each type of stellar feedback, we use tabulated results from STARBURST99 (Leitherer et al. 1999) assuming a Kroupa IMF, solar metallicity, and instantaneous star formation.

5.4.1. HII Regions

Young massive stars emit significant amounts of ionizing radiation during their first Myr after formation. This radiation can create bubbles ionized gas with temperatures around 10^4 K, HII regions, reducing the star formation rate near newborn stars. This type of feedback is important since it provides an early source of heating that can halt the gravitational collapse of gas. Photo-heating and ionization in simulations also shows to result in simulated galaxies more similar to observed galaxies (Stinson et al. 2013).

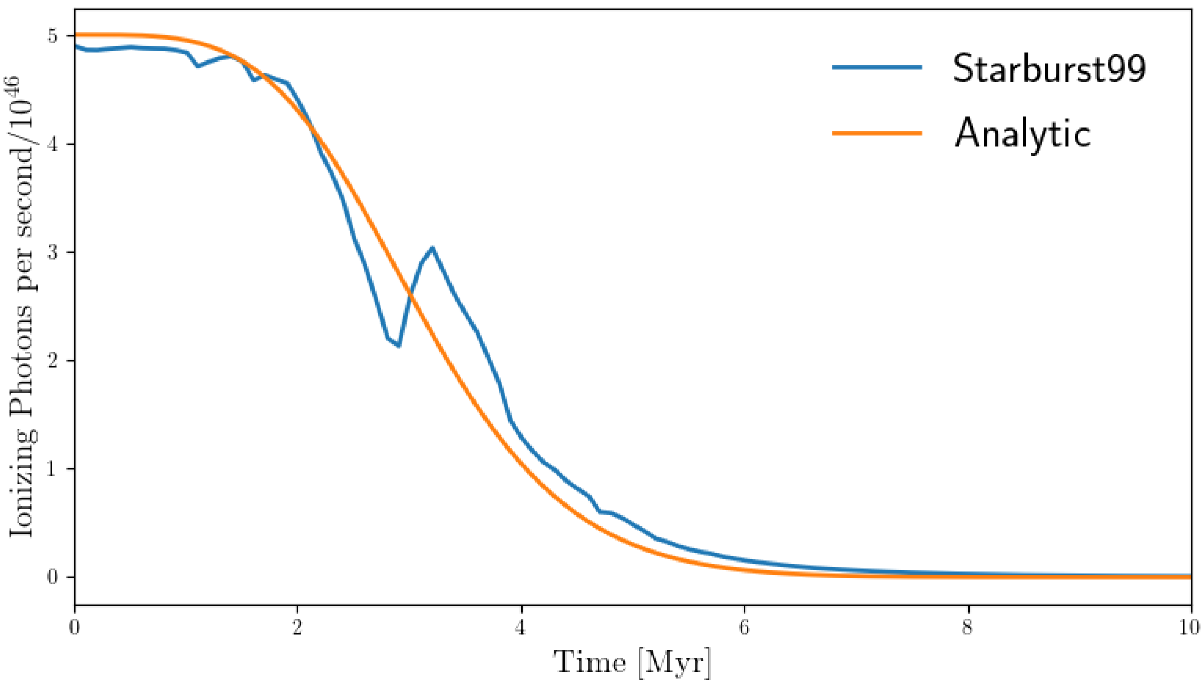

Figure 5.1: Number of ionizing photons as a function of time. The solid blue line shows the number of ionizing photons per second from the tabulated data of STARBURST99. The orange solid line shows the analytic function given by the equation 5.17 .

The size of HII regions, assuming full ionization within them, can be estimated by the Strömgren radius that is given by the equation:

$$R_S = \left(\frac{3S}{4\pi\alpha_B n^3}\right)^{1/3}, \tag{5.16}$$

where R_S is the radius of the Strömgren sphere, S is the number of ionizing photons per time unit, $\alpha_B = 2.6^{-13}\text{cm}^3\ \text{s}^{-1}$ is the Case B recombination rate of hydrogen at a temperature $T = 10^4$ K, and n is the number density of gas. To compute R_S in simulations we use an analytic approximation of S, according to the results of STARBURST99. The analytic function of S is

$$S = 5\times10^{46}\text{sech}\left(\frac{t^2}{t_0^2}\right) s^{-1} \qquad ; \qquad t_0 = 2.6726\,\text{Myr}, \tag{5.17}$$

where t is the age of a stellar particle in the simulation. We show the curve from STARBURST99 and the analytic function of S in Figure 5.1.

To add the energy budget of HII regions, we follow the approach of Goldbaum et al. (2016). At each time step, we compute R_S around young stars with an age lower than 10 Myr. Next, we compare the volume of the Strömgren sphere, $V_S = 4\pi R_S^3/3$, with the volume of the cell where the star particle resides, $V_c = \Delta x^3$, where Δx is the size of the cell. If $V_S > V_c$, the cell is heated to a temperature of 10^4 K. If $V_S < V_c$ and the cell's temperature is lower than 10^4 K we correct the energy input by V_S/V_c. This means that, if an energy ΔE is needed to heat the gas to 10^4 K, we add $\Delta E \times V_S/V_c$ instead. By doing this we ensure that HII regions always increase the thermal energy of gas. If $2V_c > V_S > V_c$ we increase the temperature of neighbor cells in the same way.

5.4.2. Stellar Winds and Radiation Pressure

The radiation from young massive stars not only can ionize gas but it can also change the momentum of the neighboring gas (Agertz et al. 2013; Marinacci et al. 2019). This early type of feedback is often claimed to drive strong outflows, drive turbulence and cause the destruction of star-forming clouds before the explosions of the first supernovae (Matzner 2002; Agertz et al. 2013). If $L_{\rm bol}(t)$ is the bolometric luminosity of a stellar population, the momentum injection rate is given by:

$$\dot{p}_{\rm rad} = (1 + {\rm e}^{-\tau_{UV}} + \tau_{\rm IR})\frac{L_{\rm bol}(t)}{c}. \tag{5.18}$$

The term $(1 + {\rm e}^{-\tau_{UV}})$ represents the absorption and scattering of UV light. For the UV opacities found in star forming regions $(1 + {\rm e}^{-\tau_{UV}}) \approx 1$. The last term, $\tau_{\rm IR}$ takes into account multiple scattering of IR photons by dust grains. For our simulations, and assuming an IR opacity if $\kappa_{\rm IR} = 10\ {\rm cm^2 g^{-1}}$, the optical depth of IR radiation is usually $\tau_{\rm IR} \simeq 0.2$. We do not consider the scattering of IR photons and we set $\tau_{\rm IR} = 0$.

The rate momentum injection is then given by $L_{\rm bol}/c$. We get $L_{\rm bol}$ from tabulated results of STARBURST99. To compute the momentum injection, first we calculate the cumulative bolometric energy $E_{\rm bol}(t) = \int_0^t L_{\rm bol}(t'){\rm d}t'$. We also approximate $E_{\rm bol}(t)$ by an analytic function. The cumulative energy for a stellar population as a function of time is given by

$$E_{\rm bol}(t) = \eta_{\rm bol}\frac{M_\star}{M_\odot}\bar{E}(t)M_\odot c^2, \tag{5.19}$$

where $\eta_{\rm bol} = 4.98 \times 10^{-4}$, and $\bar{E}(t)$ is a dimensionless function given by

$$\bar{E}(t) = \frac{1}{3}\left(\tanh\left(\frac{t}{t_0}\right) + 2\tanh\left(\frac{t}{t_1}\right)\right), \tag{5.20}$$

where $t_0 = 27$ Myr, and $t_1 = 4.9$ Myr. We show our analytic approximation of $E_{\rm bol}(t)$ and the tabulated values of STARBURST99 in Figure 5.2.

Stars can also add momentum to the surrounding gas through stellar winds. Stellar winds also help to disperse dense gas clouds from which stars are born (Marinacci et al. 2019). To account this source of feedback we use the tabulated calculations of STARBURST99 of the cumulative momentum as a function of time from stellar winds. We approximate the momentum injection by an analytic function. A star particle with mass $M_\star$ injects a momentum $p_{\rm wind}(t)$ given by:

$$p_{\rm wind}(t) = \eta_{\rm wind}\frac{M_\star}{M_\odot}\bar{p}(t)M_\odot c, \tag{5.21}$$

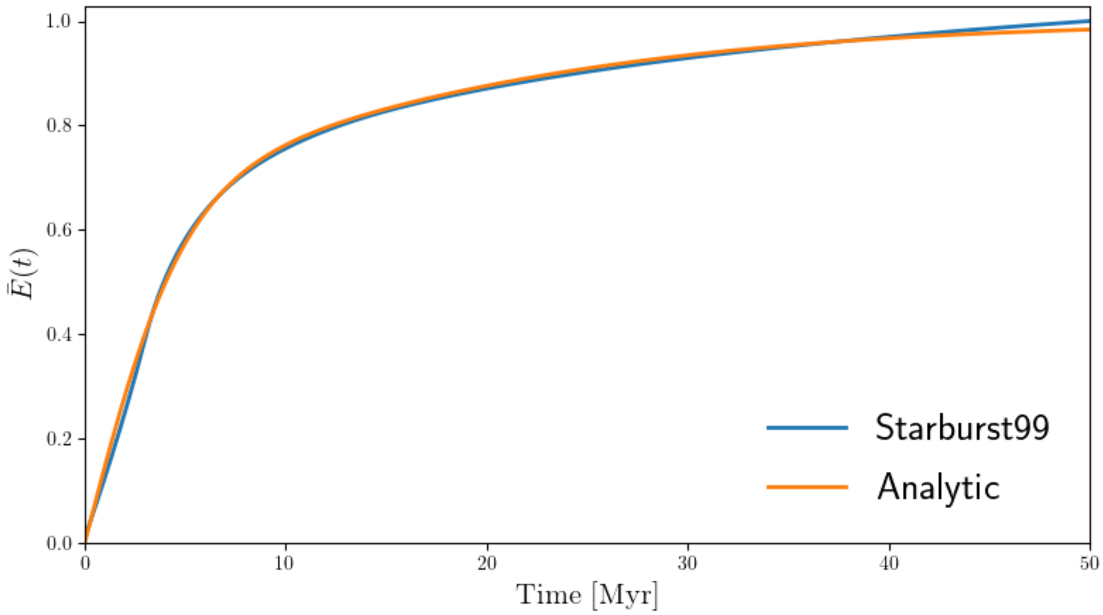

Figure 5.2: Normalized bolometric cumulative energy of a stellar population. The blue line shows the normalized integral of bolometric luminosity for a stellar population according to STARBURST99 calculations. The orange line shows the analytic approximation in equation 5.20.

where $\eta_{\rm wind} = 2.57 \times 10^{-4}$, and $\bar{p}(t)$ is a dimensionless function given by

$$\bar{p}(t) = \frac{1}{3}\left(1 + \tanh\left(\frac{t - t_0}{t_1}\right) + \tanh\left(\frac{t}{t_2}\right)\right), \tag{5.22}$$

where $t_0 = 3.12$ Myr, $t_1 = 1.29$ Myr, and $t_2 = 4.46$ Myr. The total momentum input from a stellar population is $\eta_{\rm wind} M_\odot c$ per solar mass, and $\bar{p}(t)$ is a function that goes from 0 to 1. In the simulations, for a given time interval $[t, t + \Delta t]$ we inject a momentum $\Delta p_{\rm wind} = p_{\rm wind}(t+\Delta t) - p_{\rm wind}(t)$. We split this momentum among the nearest six cells to the cell where the star resides in. We show our analytic approximation of $p_{\rm wind}(t)$ and the tabulated values of STARBURST99 in Figure 5.3.

Since the momentum from stellar winds and radiation is added for one stellar particle at a time, there is some cancellation of the injected momentum for groups of stellar particles separated by one cell (Hopkins & Grudić 2019).

5.4.3. Supernova II explosions

SN feedback plays an important role regulating star formation and shaping the structure of the ISM (Agertz et al. 2013; Hopkins et al. 2014). Supernovae deposit energy, momentum and metals into the ISM. In this work, we implement SN feedback by changing the thermal energy of gas cells directly where stellar particles reside. We calculate the rate of energy injection using the tabulated information in STARBURST99. We show in Figure 5.4 the energy rate or luminosity, and the cumulative energy desposited by SN explosions for a stellar population

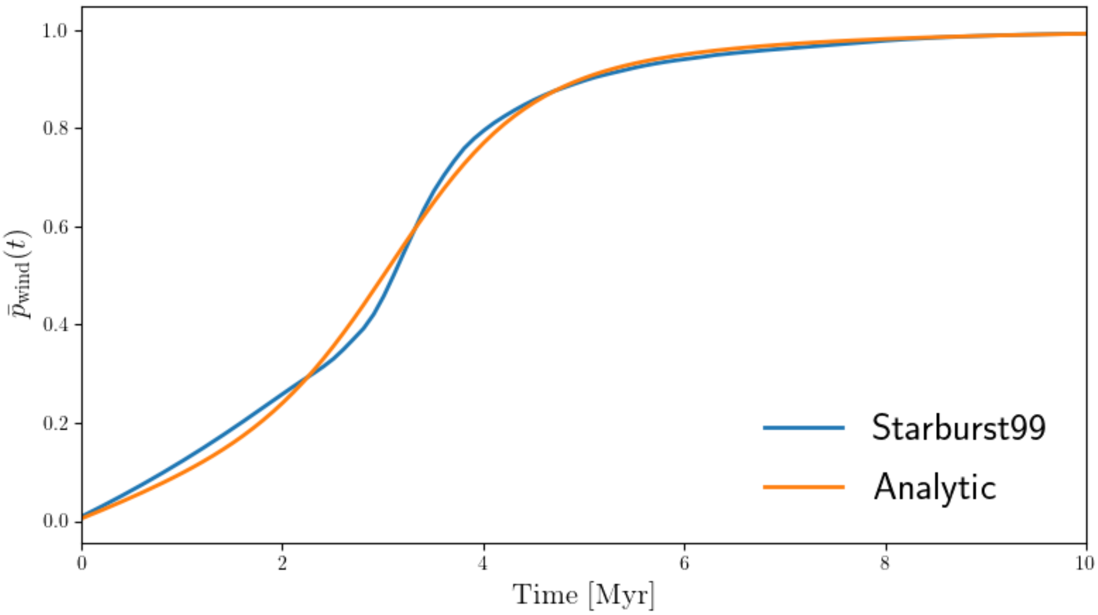

Figure 5.3: Normalized momentum input of a stellar population. The blue line shows the normalized integral of the rate of momentum injection for a stellar population according to STARBURST99 calculations. The orange line shows the analytic approximation in equation 5.22.

of $10^6 M_\odot$. Similar to the other feedback recipes, we use an analytic function to compute the amount of energy to be deposited in gas cells. The rate of energy injection is given by

$$\dot{E}_{SN}(t) = \begin{cases} 0 & t \leq 3.21\,\mathrm{Myr} \\ L_0 + L_1\,\mathrm{sech}^2\left(\dfrac{t-t_1}{t_0}\right) & 3.21\,\mathrm{Myr} < t \leq 10.768\,\mathrm{Myr} \\ L_2\left(\dfrac{t}{t_0}\right)^{\delta} & 10.768\,\mathrm{Myr} < t < 38.2\,\mathrm{Myr} \\ 0 & 38.2\,\mathrm{Myr} \leq t \end{cases} \tag{5.23}$$

where $L_0 = 1.72 \times 10^{40}$erg/s, $L_1 = 2.69 \times 10^{38}$erg/s, $L_2 = 1.41 \times 10^{40}$, $t_0 = 8.30\,\mathrm{Myr}$, $t_1 = 5.55\,\mathrm{Myr}$, and $\delta = -0.593$. This analytic function is illustrated by the dash-dotted lines in Figure 5.4. Equation 5.23 has errors below 4 % compared to the tabulated results of STARBURST99. For a time step Δt we deposit an energy

$$E_{\rm SN} = \eta_{\rm SN}\dot{E}_{\rm SN}(t_\star)\left(\frac{M_\star}{10^6 M_\odot}\right)\Delta t, \tag{5.24}$$

where $M_\star$ is the particle mass, $t_\star$ the stellar particle age, and $\eta_{\rm SN}$ is a factor to change the amount of energy deposited per stellar mass.

5.5. Additional Simulations

We run a second set of simulations using only supernovae feedback to explore the effects of changing the feedback prescription. This second set has a higher density threshold of

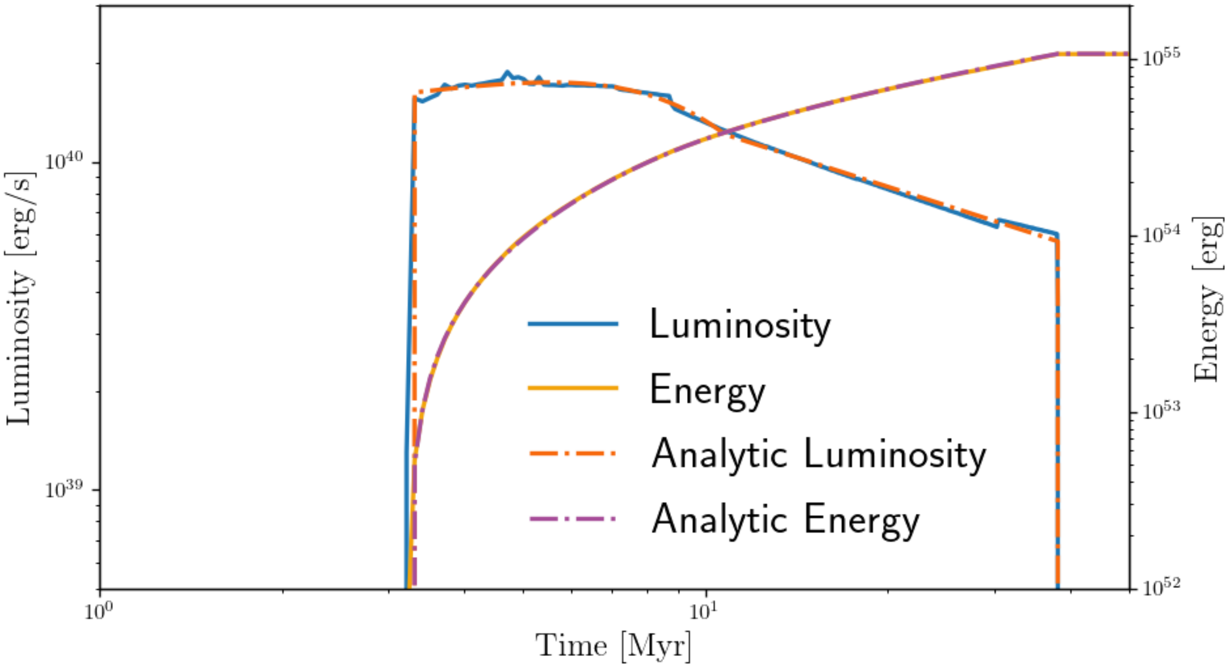

Figure 5.4: Supernova Feedback: Energy rate or luminosity, and the cumulative energy desposited by SN explosions for a stellar population of $10^6 M_\odot$. The blue and yellow solid lines represent tabulated results from STARBURST99 (Leitherer et al. 1999) assuming a Kroupa IMF, solar metallicity, and instantaneous star formation. Dashed orange and purple lines correspond to the analytic approximation in equation 5.23.

2800 cm^{-3}, necessary to match the Kennicutt-Schmidt relation (Kennicutt 1998). Except from the expected decrease in the magnitude of non-circular motions due to the injection of less energy on small scales, most of the conclusions from the previous set of simulations hold also for these simulations.

Chapter 6

Results

6.1. Disk structure

We begin by checking the structure of our simulated galaxies at $t = 700$ Myr. In Figure 6.1 we show projections of the gas density field across the z-axis. These maps have a spatial dimension of (50 kpc)^2. Our galaxies show a flocculent structure and do not present grand design spiral patterns or bars. Near the galactic center, we see clumps with different sizes for each simulation, particularly larger clumps for G2E1 which show signs of tidal interactions. Structures in G1E0.5 appear to be less affected by shear due to the lower magnitude of its rotation curve. Structures in G1E0.5 appear to be more decoupled from galactic rotation in comparison to G2E1 and G1E1. The dashed white circle of 15 kpc radius in Figure 6.1 shows the outer edge of the outermost radial annulus where we measure the circulation of gas. When we measure the circulation within square regions of size 5 kpc, and centered on a point at radius 15 kpc, we include points that are up to a distance of 18.54 kpc from the galactic center. We show a 18.54 kpc radius dotted circle for illustrative purposes in Figure 6.1.

The middle panel of Figure 6.1 shows the surface density of the stellar particles formed in the course of the simulation. The stellar distributions show no clear sign of spiral structures. On the other hand, all the simulations show large stellar clusters. G2E1 shows the largest stellar cluster at the center of this galaxy. On the other extreme, G1E1 has a stellar distribution that is more homogeneous, but it does not have a large radial extension.

In the bottom panel of Figure 6.1 we show the face-on projection of the temperature field weighted by density. This map is computed as:

$$T(x,y) = \int \rho(x,y,z)T(x,y,z)/\int \rho(x,y,z)\mathrm{d}z. \tag{6.1}$$

We can see that regions of low density adjacent to high density regions show temperatures up to $10^7 K$ produced by stellar feedback. If we zoom-in we can see the effects of the recipe for HII regions. Figure 6.2 shows the temperature map at the center of each galaxy. We can clearly see small points of high temperature within the knots and filaments of high density.

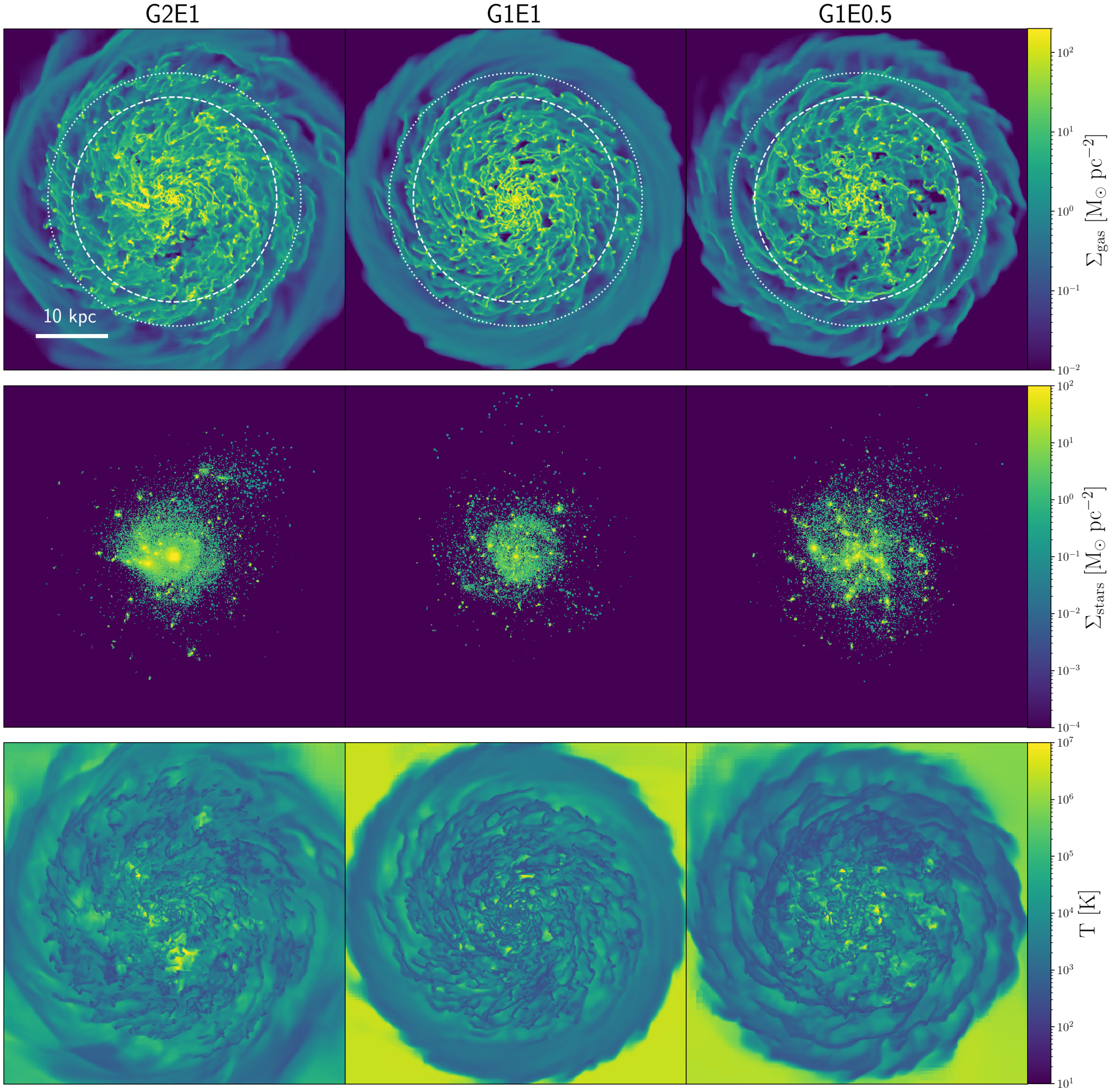

Figure 6.1: Face-on projections of simulated galaxies at $t = 700$ Myr of size (50 kpc)^2. From left to right we show the projections for G2E1, G1E1, and G1E0.5. *Top:* Gas surface density map. Dashed white circles delimit the region inside 15 kpc which corresponds to the maximum radius of the defined annuli. The dotted line shows the maximum radius of the cells that are included in the analysis of circulation, which corresponds to 18.54 kpc. *Middle:* Surface density of stellar particles formed in the simulations. *Bottom:* Density weighted projection of the temperature field.

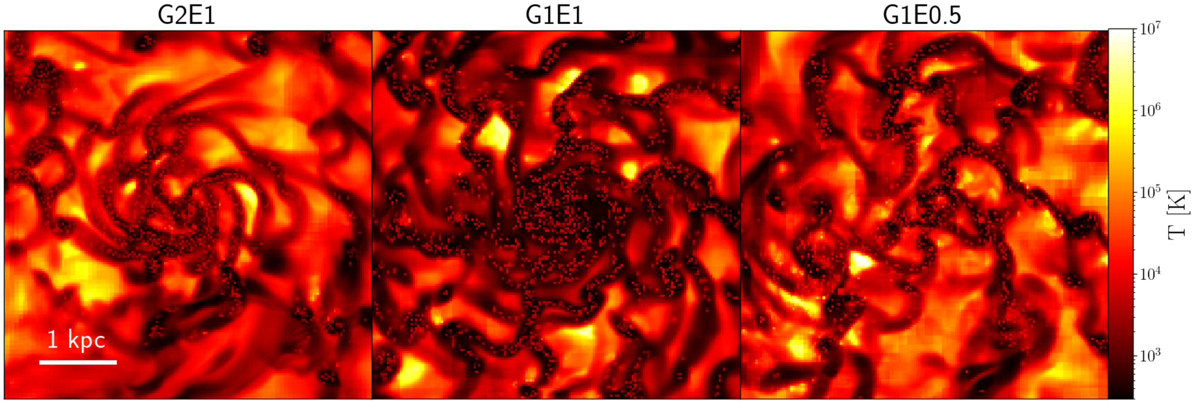

Figure 6.2: Temperature maps of size (5 kpc)^2

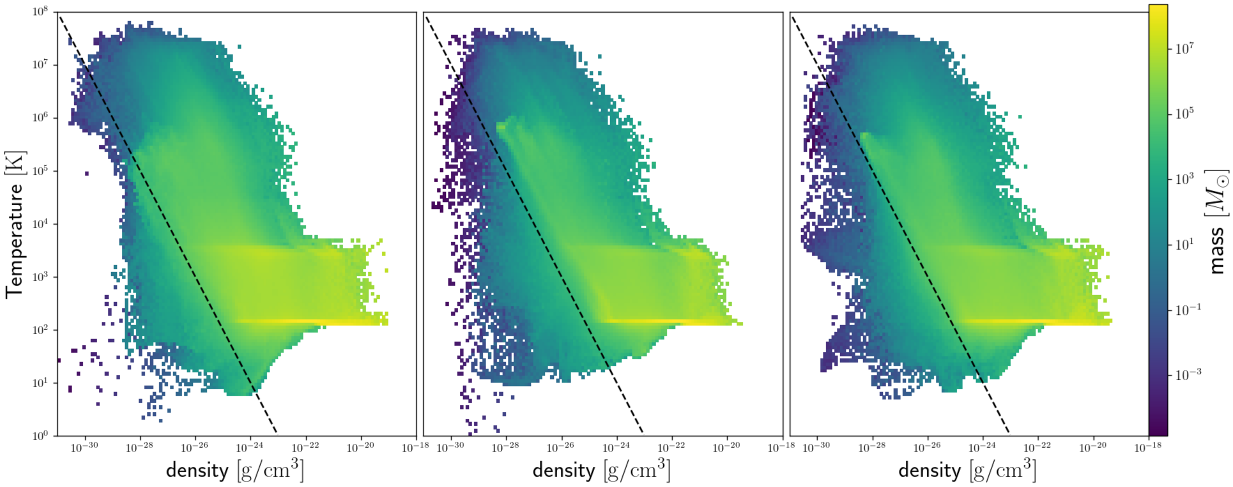

Figure 6.3: 2D Phase plots of temperature and density of gas. The plots correspond to runs G2E1, G1E1, G1E0.5 from left to right. Colors represent the total mass in cells with the respective values of T and ρ. The black dashed line represent a curve of constant pressure $P \propto \rho T$.

In Figure 6.3 shows $T - \rho$ phase diagrams of the ISM. These diagrams shows that we are not resolving the cold ISM due to the temperature floor at 300 K. Instead of giant molecular clouds, the overdensities in these simulations represent HI clouds. Most of the mass is in the cold phase of the ISM. Regions with temperatures below 300 K correspond to expanding regions that cool adiabatically. The gas also follows paths of constant pressure $P \propto \rho T$ illustrated by the black dashed line in Figure 6.3.

Another important diagnostic of dynamics for galactic disks is the Toomre parameter Q (Toomre 1964). The classical Toomre parameter is $Q = \kappa c_s/\pi G\Sigma$ with c_s the sound speed, κ the epicyclic frequency, and Σ the gas surface density. Variations of this parameter include the effects of the total velocity dispersion of gas σ_v, with $Q = \kappa\sigma_v/\pi G\Sigma$. However, for turbulent fields σ_v its itself a function of k (Romeo et al. 2010) while c_s is not. Other approaches include the effect of stars, and disk thickness in the stability of disks. In particular Romeo & Falstad (2013) define the Toomre parameter for a multi-component disk as

$$\frac{1}{Q_N} = \sum_{i=1}^{N} \frac{W_i}{T_i Q_i}, \tag{6.2}$$

where $Q_i = \kappa\sigma_i/\pi G\Sigma_i$ is the Toomre parameter of the i-th component, σ_i is the radial velocity dispersion, T_i is the thickness correction given by

$$T \approx \begin{cases} 1 + 0.6\left(\frac{\sigma_z}{\sigma_R}\right)^2 & \text{for } 0 \leq \sigma_z/\sigma_R < 0.5 \\ 0.8 + 0.7\left(\frac{\sigma_z}{\sigma_R}\right) & \text{for } 0 \leq \sigma_z/\sigma_R < 0.5 \end{cases} \tag{6.3}$$

and W_i are the weights

$$W_i = \frac{2\sigma_m\sigma_i}{\sigma_m^2 + \sigma_i^2}, \tag{6.4}$$

where the index m denotes the component with smallest $Q : Q_m = \min\{Q_i\}$. Figure 6.4 shows the profiles of the Toomre parameter for gas, stars, and the multi-component version of Romeo & Falstad (2013). To compute these profiles and their errorbars we use the data of the following 30 Myr. We see that Q_{gas} shows high values compared to Q_{stars}. The blue line shows the multi-component Toomre parameter which lies close to Q_{star}. This shows that stars keep the disk near marginal stability, i.e. $Q \approx 1$. Except for G1E0.5, we don't see a clear radial trend for Q. Li et al. (2005) suggested that the efficiency of star formation may be controlled by the Q parameter. However, Q does not show the behaviour of ϵ_{SF}.

6.2. Star formation

We need to test whether our recipes of star formation and stellar feedback produce a realistic rate of star formation. The most common benchmark is the Kennicutt-Schmidt relation (Kennicutt 1989). Observations show that at first order, the star formation per unit area, Σ_{SFR}, in galaxies can be parameterized by

$$\Sigma_{\text{SFR}} \propto \Sigma_{\text{gas}}^N, \tag{6.5}$$

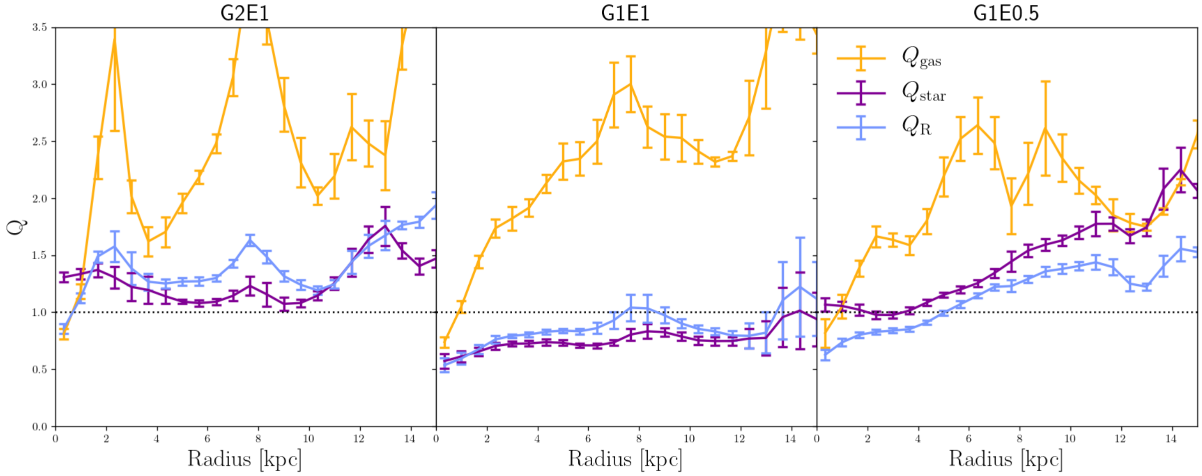

Figure 6.4: Radial profiles of the Q Toomre parameter for each run. Yellow lines show the Toomre parameter for the gaseous component, while the purple line shows the Toomre parameter of the stellar component. The blue line shows the effective Toomre parameter as defined by (Romeo & Falstad 2013).

where $\Sigma_{\rm gas}$ is the gas surface density, and N is the exponent of the power law. Kennicutt (1989) found empirically an index of 1.4, that has been proposed to come from the ratio between $\Sigma_{\rm gas}$ and the free-fall time $t_{\rm ff}$. In Figure 6.5 we show the $\Sigma_{\rm SFR} - \Sigma_{\rm gas}$ plot for our galaxies at $t = 700$ Myr.

To compute $\Sigma_{\rm gas}$ and $\Sigma_{\rm SFR}$ we divide the disk of each galaxy in annulus with a width of 500 pc, and we consider the gas and particles within 1000 pc from the midplane in the vertical axis. We consider all the gas inside these annular regions. To compute the star formation rate we consider stars formed in the last 10 Myr. We show $\Sigma_{\rm gas}$ and $\Sigma_{\rm SFR}$ for each one of these regions as circles in the left panel of Figure 6.5.

For comparison with observational studies, we show as shaded regions the regimes of normal and starburst galaxies defined by Daddi et al. (2010). These two sequences follow a relation $\Sigma_{\rm SFR} \propto \Sigma_{\rm gas}^{1.42}$. The star formation across the galactic disks of our galaxies falls in the sequence of normal disk galaxies. In table 6.1 we show the fits to the star formation relations. All the simulations show an exponent lower than 1.5. Comparing each run, G2E1 and G1E0.5 show higher $\Sigma_{\rm SFR}$ for a given $\Sigma_{\rm gas}$. G2E1 has the highest gas content and a similar gas fraction compared to G1E0.5. It is noteworthy that, although G1E0.5 and G1E1 have the same initial gas content, G1E0.5 is consistently forming stars at a higher rate. This result agrees with the work of Utreras et al. (2016) that found that the efficiency of star formation is anti-correlated with the degree of galactic rotation. G1E0.5 has a lower rotation compared to G1E1, about 1.4 times lower.

We also compare our results with the star formation relation proposed by Escala (2015), given by:

$$\Sigma_{\rm SFR} = \epsilon_{\rm SF} \sqrt{\frac{G}{L}} \Sigma_{\rm gas}^{3/2}, \tag{6.6}$$

Table 6.1: Star formation relations

	$\log_{10}\Sigma_{\rm SFR} \propto$	$N\log_{10}\Sigma_{\rm gas}+C$	$\log_{10}\Sigma_{\rm SFR} \propto$	$N\log_{10}\Sigma_{\rm gas}^{\frac{3}{2}}\sqrt{\frac{G}{H}}+C$
Run	N	C	N	C
G2E1	1.28 ± 0.18	-3.53 ± 0.24	1.01 ± 0.14	-1.80 ± 0.06
G1E1	1.41 ± 0.06	-3.84 ± 0.09	0.84 ± 0.04	-2.01 ± 0.02
G1E0.5	1.31 ± 0.08	-3.48 ± 0.11	0.81 ± 0.05	-1.86 ± 0.02

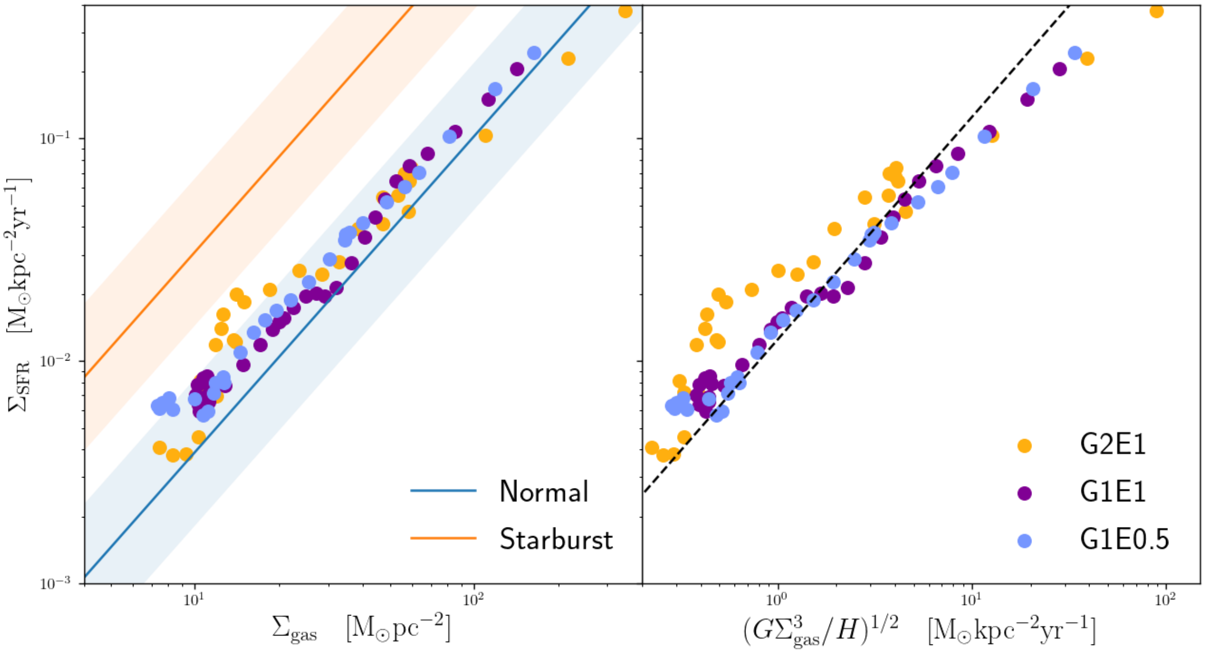

Figure 6.5: Star formation relations. *Left* : $\Sigma_{\rm SFR}$ vs $\Sigma_{\rm gas}$. Yellow, blue and purple circles represent runs G2E1, G1E1, and G1E0.5 respectively. The blue shaded region corresponds to the normal sequence of star formation as defined by Daddi et al. (2010), whereas the orange shaded region corresponds to the sequence of starburst galaxies. *Right* : $\Sigma_{\rm SFR}$ vs $(G\Sigma_{\rm gas}/H)^{1/2}$. The black dashed line represents a relation $\Sigma_{\rm SFR} = \epsilon_{\rm SF}$ $(G\Sigma_{\rm gas}/H)^{1/2}$.

where L represents a characteristic length scale of the system, and $\epsilon_{\rm SF}$ is the dimensionless efficiency of star formation. This relation is motivated by dimensional analysis, that states that only quantities with the same dimensions can be compared. In equation 6.6, the star formation efficiency $\epsilon_{\rm SF}$ is likely to be related with the dynamics inside molecular clouds through dimensionless quantities, which have been found and tested in simulations (Padoan et al. 2012; Semenov et al. 2016).

We assume that L is the scale height H. To compute H we divide each annulus in subregions with at least 200 cells. On each of these regions we compute H_i as

$$H_i = \sqrt{\langle z^2\rangle - \langle z\rangle^2} \quad \& \quad \langle z^n\rangle = \frac{\sum m_j z_j^n}{\sum m_j}. \tag{6.7}$$

Then, for each annulus we have a distribution of values H_i. We take the median as the representative value of the scale height H. We do this to reduce the effect of possible bending modes in the galactic disks, which can spuriously increase the values of H. We plot equation 6.6 in the right panel of Figure 6.5. The black dashed line in Figure 6.6 illustrates a linear relation (exponent equal to one). We fit power law relations to these values, and the results are displayed in table 6.1. We see that adding the effect of the scale height splits the points of G2E1 from the others, showing a higher star formation rate for the same conditions of gas content and self gravity.

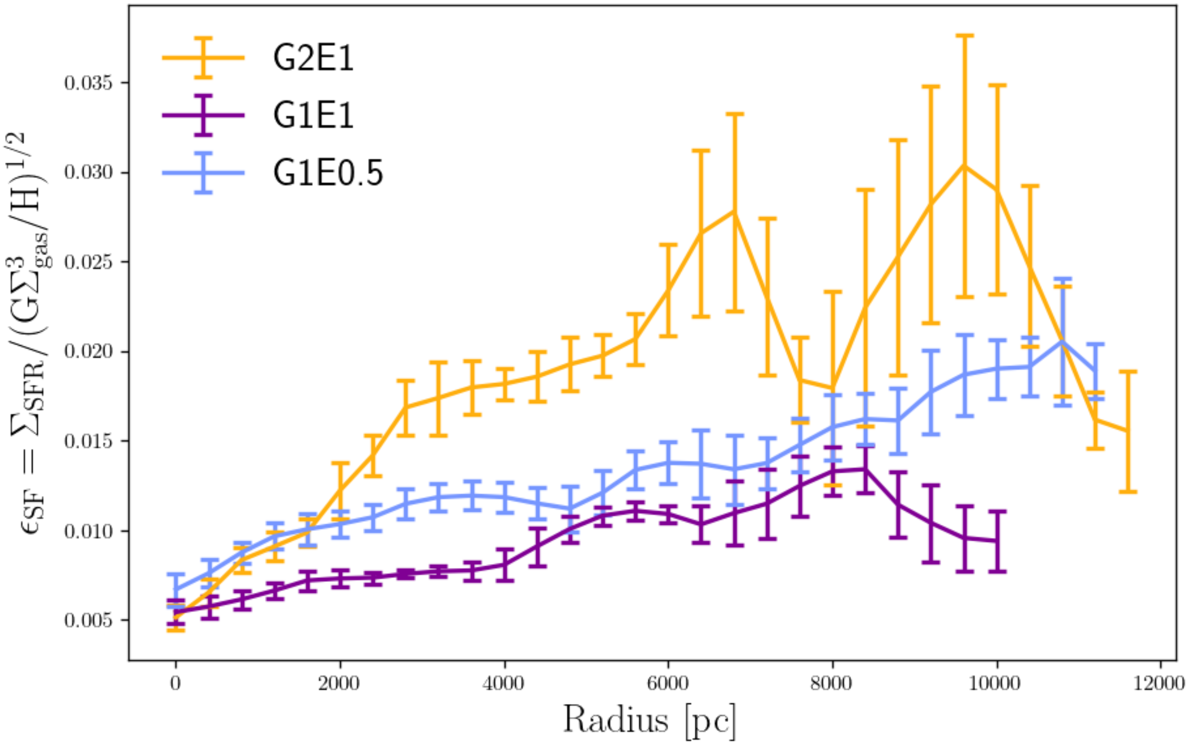

Figure 6.6: Dimensionless efficiency of star formation $\epsilon_{\rm SF}$ vs galactocentric radius. Yellow, blue and purple lines represent runs G2E1, G1E1, and G1E0.5 respectively.

There is also a consistent trend: at higher gas surface densities the efficiency of star formation decreases. Since the $\Sigma_{\rm gas}$ increases towards the center of galaxies, this trend can be seen as the variation of the efficiency versus the galactic radius. We plot $\epsilon_{\rm SF}$ versus radius in Figure 6.6. For our simulations the efficiency increases with galactocentric radius. Although the galactic center has a higher gas content it shows a lower efficiency. Since there is a clear trend, there must be a secondary parameter controlling the $\epsilon_{\rm SF}$.

In simulations of galactic disks, Utreras et al. (2016) found $\epsilon_{\rm SF} \propto \exp(-1.9\Omega t_{\rm ff})$, where Ω is the angular velocity and $t_{\rm ff}$ is the initial free-fall time. To compute $\epsilon_{\rm SF}$ Utreras et al. (2016) consider entire galaxies as a single region of star formation. Here, to estimate the rotation of each annular region we compute the vorticity $\omega_{\rm rot}$ coming from the galactic circular velocity. To compute the free-fall time we use

$$t_{\rm ff} \approx \frac{1}{\sqrt{G\rho}} \approx \sqrt{\frac{H}{G\Sigma}} \tag{6.8}$$

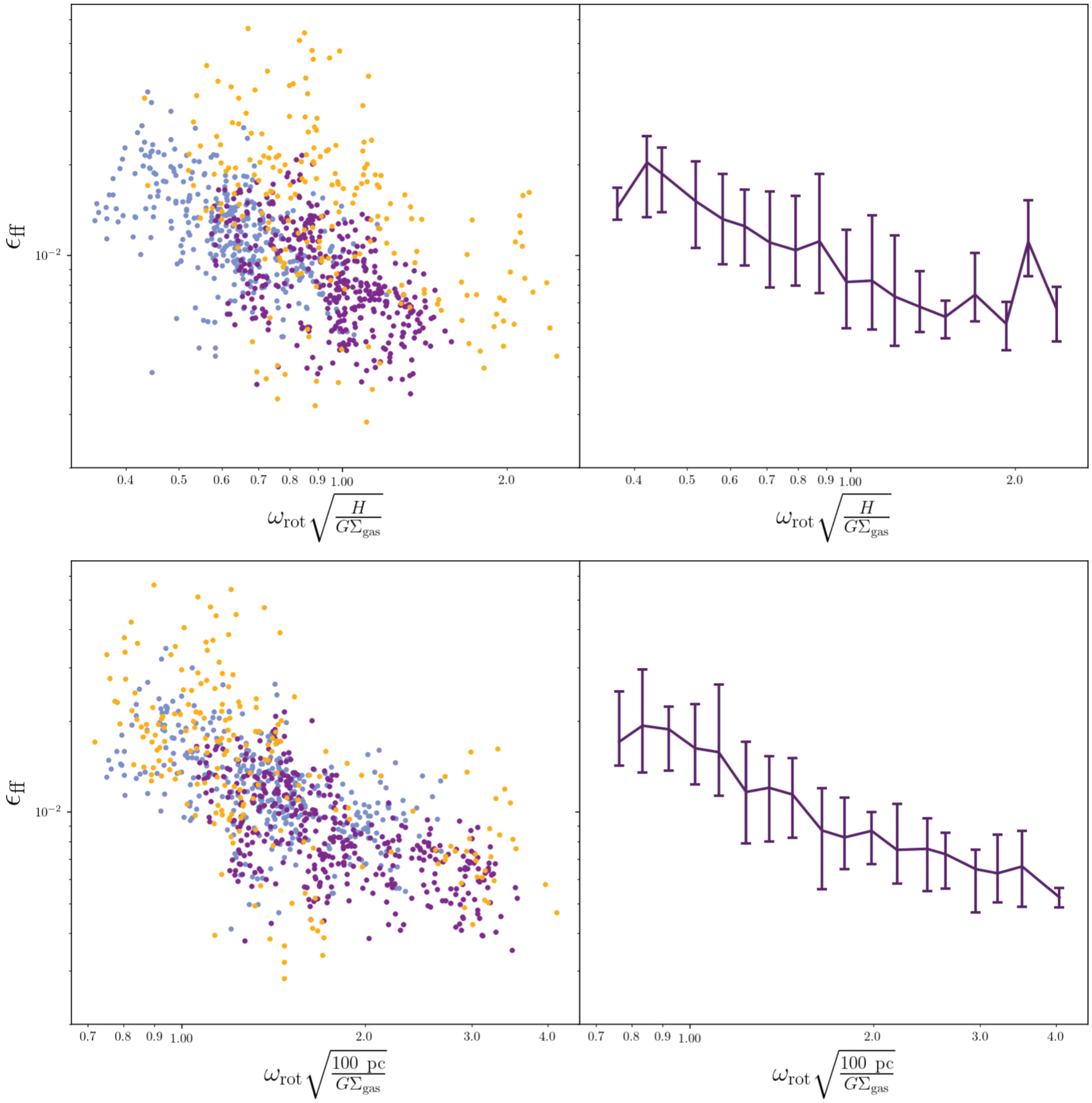

Figure 6.7: Dimensionless efficiency of star formation $\epsilon_{\rm SF}$ vs galactocentric radius. Yellow, blue and purple lines represent runs G2E1, G1E1, and G1E0.5 respectively.

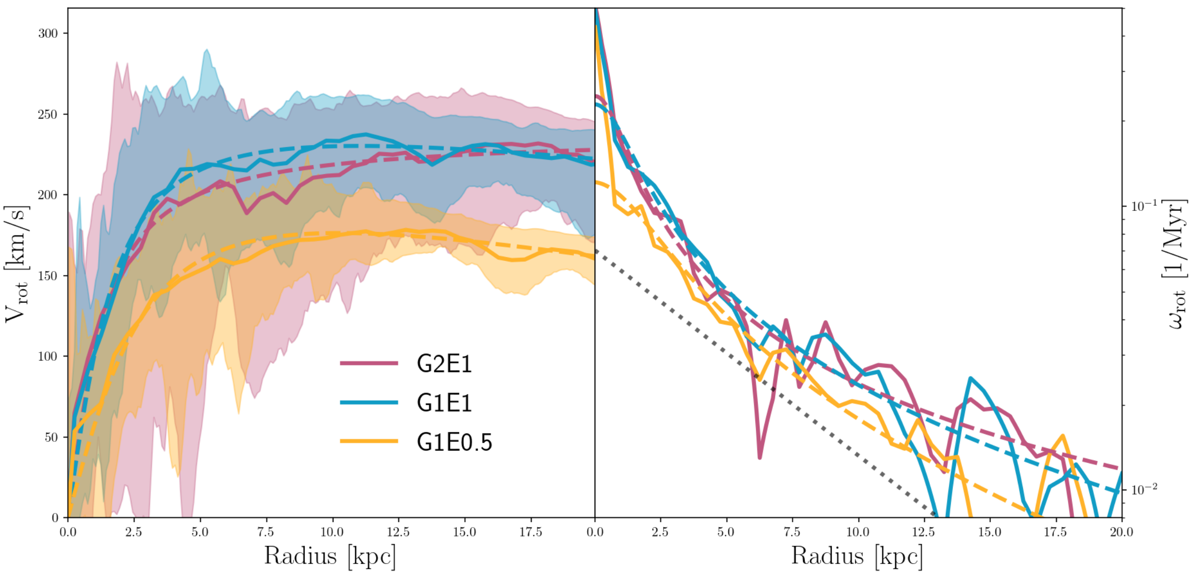

Figure 6.8: Profiles of rotational velocities and large scale vorticity. *Left*: Radial profiles of the circular velocity $v_{\rm rot}$, which are used to compute the large scale vorticity component $\omega_{\rm rot}$. Solid lines show the median values of the rotation curve. Shaded regions represent 1σ uncertainties due to variations in the velocity field. The analytic models of the rotation curves are shown as the dashed lines. *Right*: Radial profiles of vorticity $\omega_{\rm rot}(R)$. The solid and dashed lines correspond to the median values and the analytic models respectively. The gray dotted line shows a function proportional to $\exp(-R/5{\rm kpc})$ for comparison.

We plot $\epsilon_{\rm SF}$ versus $\omega_{\rm rot}\sqrt{\frac{H}{G\Sigma}}$ in the top panel of Figure 6.7. We see that there is an apparent trend between these two quantities although the scatter of G2E1 is large to make any conclusion. We have assumed that there is a balance between rotation in the plane, $\omega_{\rm rot}$ and the vertical strength of gravity. We can relax that assumption by taking $H = 100$ pc if we consider it as the typical size of clouds or if the vertical self-gravity is limited by our resolution. Using $H = 100$ pc, $\epsilon_{\rm SF}$ appears to be better correlated to $\omega_{\rm rot}\sqrt{\frac{H}{G\Sigma}}$. This could indicate that we are witnessing the effects of rotation in the efficiency of star formation. However, as we see in Figure 6.6, the efficiency is correlated with radius, hence any parameter that increases or decreases with radius will show a correlation with the efficiency of star formation.

6.3. Vorticity

We show the rotation curves $v_{\rm rot}(R)$ of each run in the left panel of Figure 6.8. The shaded regions show the variations in the tangential velocity field. Analytic rotation curves are obtained by fitting equation

$$V_{\rm rot}(R) = V_0 {\rm arctan}(R/R_1)\exp(-R/R_2) \tag{6.9}$$

to the velocity field. We show the fitted functions as dashed lines in Figure 6.8. In the right panel of Figure 6.8 we also show the resulting vorticity $\omega_{\rm rot}(R)$. We see that the vorticity coming from galactic rotation, $\omega_{\rm rot}(R)$, decreases as we get far from the galactic center. This also implies that the circulation $\gamma_{\rm rot}$ decreases as a function of radius. If the parameters that define the turbulent velocity field remain constant across the galactic disk, the relative contribution from $\gamma_{\rm rot}$ to the total circulation γ would decrease with galactocentric radius. In that scenario, the scale at which gas dynamics transitions from being dominated by galactic rotation to being dominated by non-circular motions, i.e. $\lambda_{\rm eq}$, increases with galactocentric radius since at large radii the vorticity produced by galactic rotation is smaller.

In Figure 6.9 we show the maps of the vorticity fields $\omega_{\rm rot}$, ω, and their difference $\omega - \omega_{\rm rot}$. In the top panels we see the smooth component $\omega_{\rm rot}$. In the middle panels we show the vorticity field of the two dimensional velocity field defined in section 4.2.1. We can see that towards the center of galaxies, the vorticity takes more positive values. This claim is more evident once we subtract $\omega_{\rm rot}$ to ω. This resulting field is shown in the bottom panel of 6.9. We can see that the vorticity field has a non-ordered component with structures growing in size at large radii.

6.4. Model parameters

We have assumed that the velocity field can be decomposed as the sum of two fields $v_{\rm rot}$ and $v_{\rm nc}$, where $v_{\rm nc}$ is the non-circular component modeled as a GRF. The non-circular component is modeled by the function $\mathcal{V}(k)$ in Fourier space which takes the parameters n_1, n_2, λ_c, and σ_0 to characterize the velocity field for different annuli.

In Figure 6.10 we show the probability distributions of n_1, n_2, λ_c, and σ_0, where $\lambda_c = 1/k_c$ corresponds to the characteristic scale of the model $\mathcal{V}(k)$. Keep in mind that, given the shape of the chosen function $\mathcal{V}(k)$, the parameters n_1, n_2, and λ_c are correlated parameters. Runs G2E1 and G1E1 show variations of n_1 between 1.0 and 1.9. The distribution of λ_c ranges from its minimum value ~ 240 pc to 1.1 kpc. In the annulus of G1E1 centered at 4.5 kpc λ_c is unresolved. The parameter σ_0 shows narrow distributions. G2E1, the most massive galaxy, shows values of σ_0 above 30 km s^{-1} at all radii. The distribution of n_2 gets flat for values over 5. The model is not sensitive to variations of n_2 over $n_2 = 5$. Equation 3.6 shows the contribution from each scale ℓ and the amplitude of the vorticity field through an integral of $\mathcal{V}(k)$. As the values of n_2 increases, the contribution from $k > k_c$ to the vorticity field starts to get smaller. This suggests that the function $\mathcal{V}(k)$ can be approximated as a single power law with a cut at k_c, i.e. $\mathcal{V}(k > k_c) = 0$. This is shown later in section 6.10.

We show in Figures 6.11 to 6.15 detailed distributions for each galaxy in different regions. The diagonal plots show the marginalized distributions for each parameter. The off-diagonal plots on each Figure show two-dimensional histograms of the model parameters which help to visualize the correlation between them. We can see a negative correlation between λ_c and n_1, and also between λ_c and n_2 for low values of n_2. In Figure 6.11 we see that the distribution of n_2 peaks close to the lower limit imposed by our prior. This is also true for the annular regions 3-6 kpc in G2E1, 0-3 kpc in G1E1, and 3-6 kpc in G1E0.5. In these figures is notorious how the correlation between λ_c and n_2 disappears for $n_2 > 5$. As mentioned before this is consistent with a single power law with a cut at k_c which corresponds to the limit $n_2 \to \infty$.

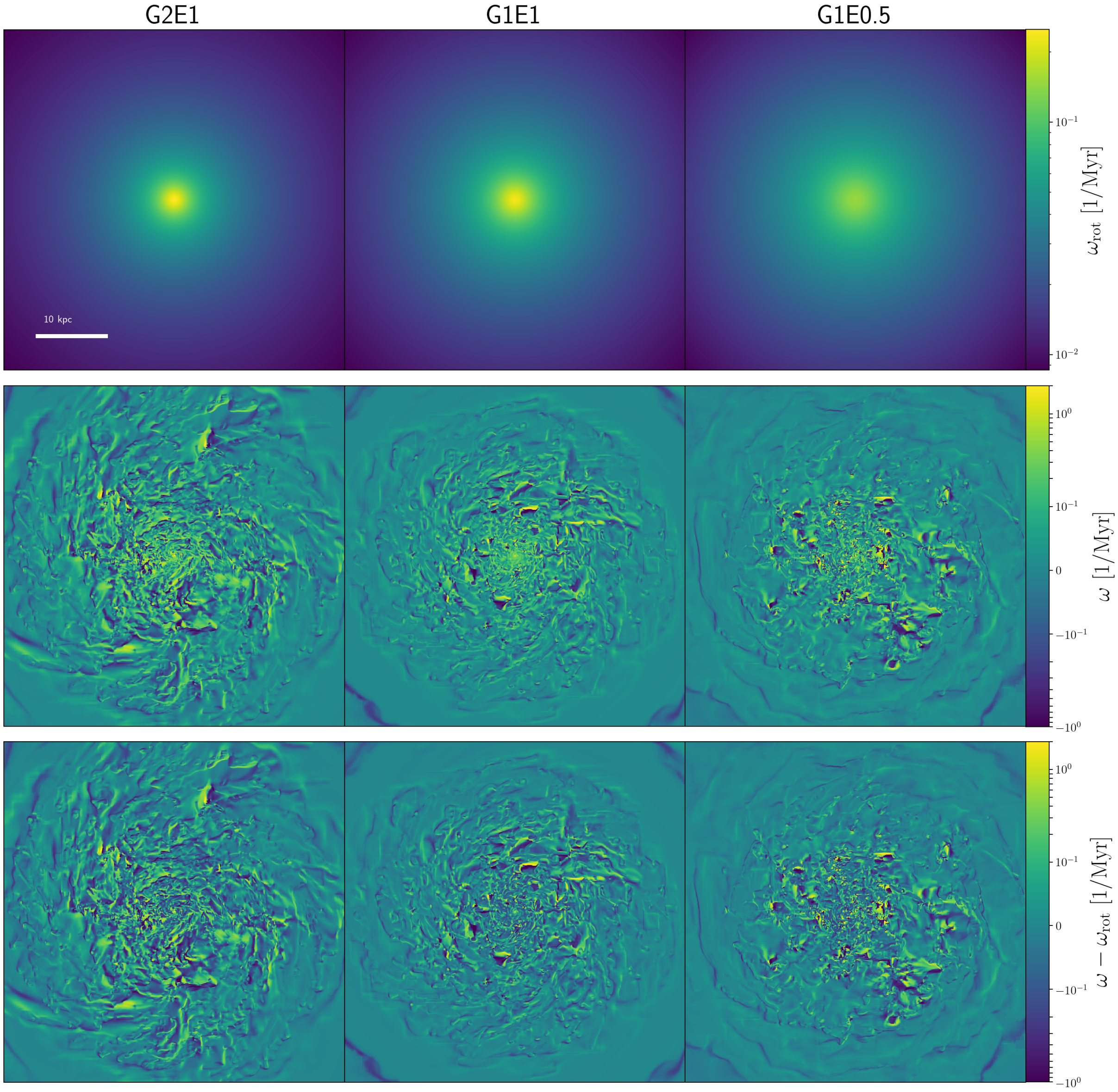

Figure 6.9: Vorticity maps of simulated galaxies for a region of 40 kpc x 40kpc. *Top:* Maps of the smooth component $\omega_{\rm rot}$. *Middle:* Maps of the measured vorticity ω. *Bottom* Maps of the difference between ω and $\omega_{\rm rot}$.

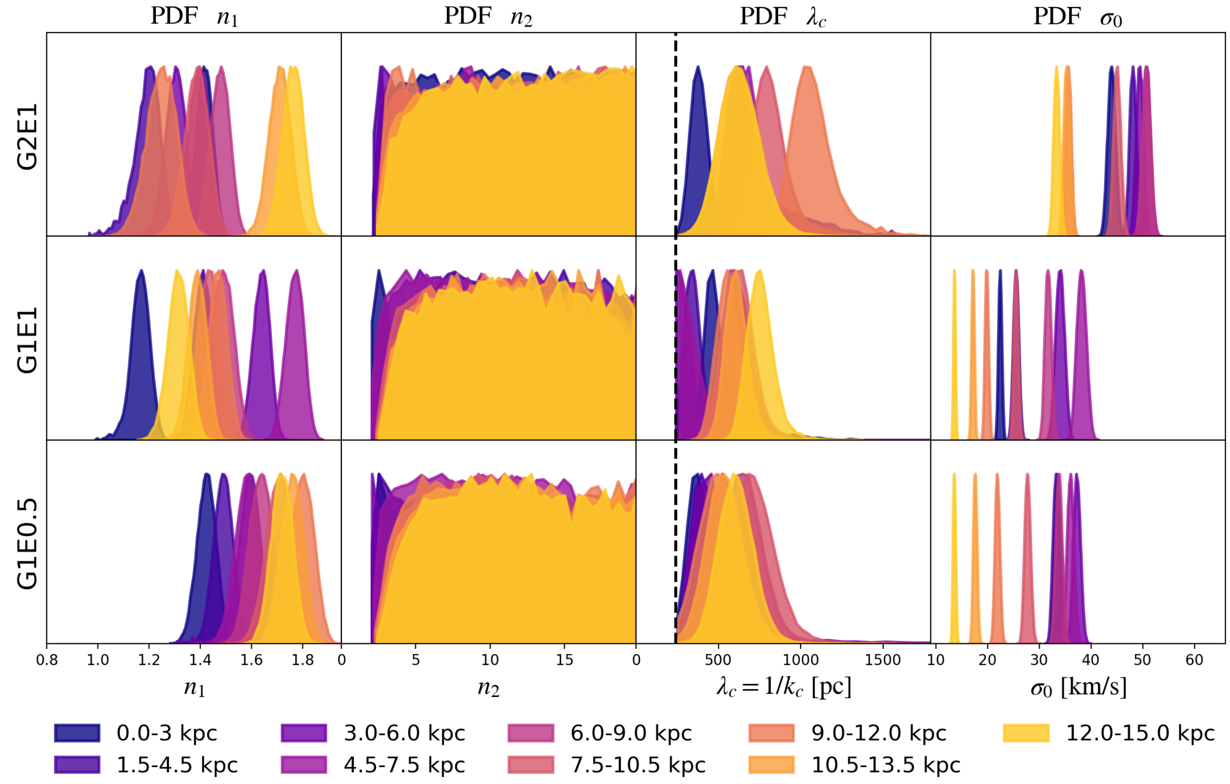

Figure 6.10: Posterior distributions of model parameters. From top to bottom we plot the distributions for each of the three simulations. From left to right we show normalized distributions of n_1, n_2,$\lambda_c = 1/k_c$, and σ_0. The distribution for each annulus is shown with a characteristic color, going from purple to yellow with increasing galactocentric radius. The vertical black dashed line in the distributions for λ_c corresponds to eight times the resolution of the simulations, the minimum allowed value for λ_c.

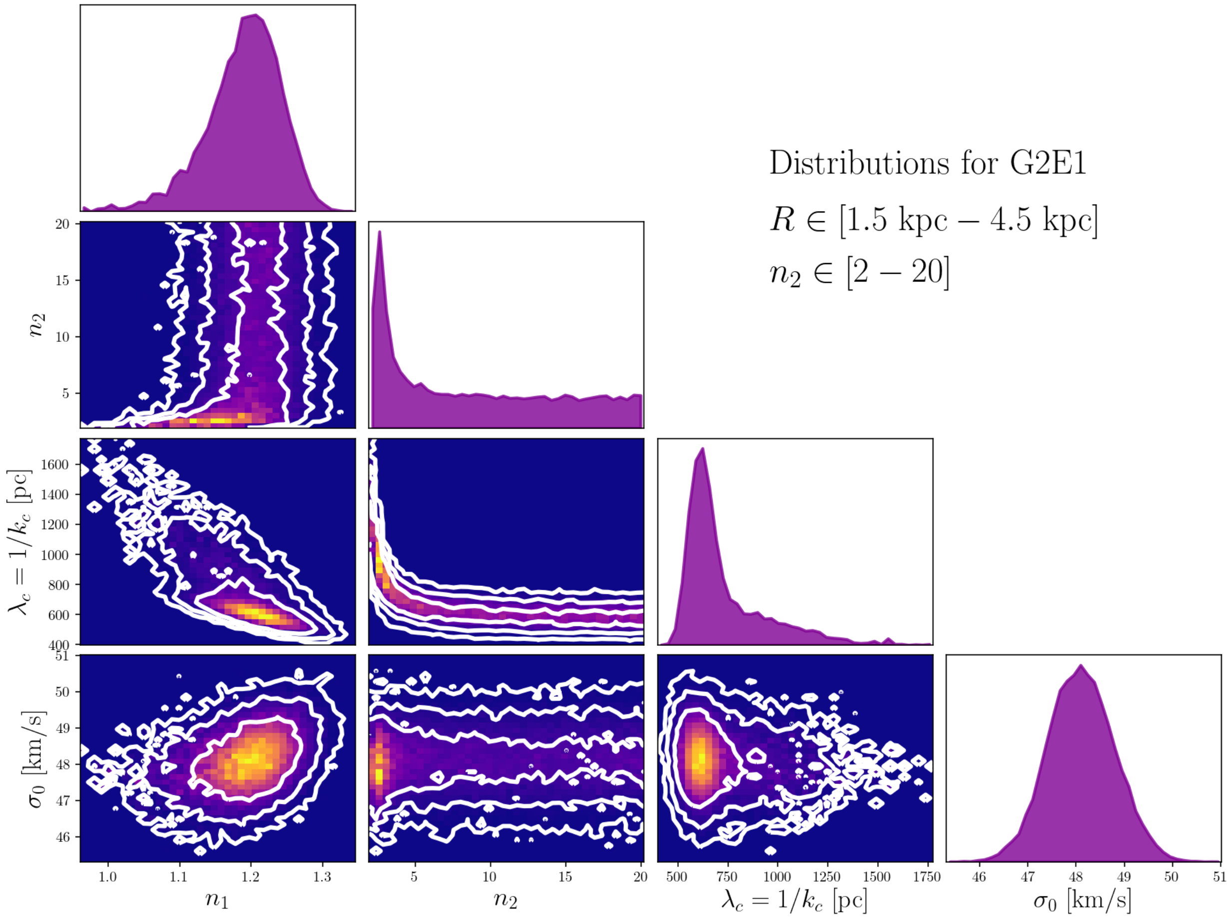

Figure 6.11: Distributions of parameters n_1, n_2, $\lambda_c = 1/k_c$, and σ_0 for run G2E1, in the radial annulus [1.5 kpc - 4.5 kpc]. Purple histograms in the diagonal show the marginal posterior distributions for n_1, n_2, $\lambda_c = 1/k_c$, and σ_0 in descending order. Off-diagonal plots show two-dimensional histograms of the model parameters. White contours show the 68 %, 95 %, and 99.7 % confidence intervals.

Figures 6.11, 6.14, and 6.15 show the distributions for each run at the same location on the galactic disk, between 6 and 9 kpc from the center. The three runs show the same behaviors in their distributions.

For an easier comparison between the parameters of each galaxy we create their corresponding radial profiles. Radial variations of the parameters are summarized in Figure 6.16. If we look at the first and second panels of Figure 6.16 we can see that n_1 and λ_c are anti-correlated for runs G2E1 and G1E1. This is also true for G1E0.5 but is not noticeable in Figure 6.16. G1E1 and G1E0.5 show similar values of σ_0 at large galactocentric radius besides having different rotation curves. They also show similar profiles of λ_c at large radii. Their profiles of σ_0 have large magnitudes compared to the velocity dispersion profiles measured in nearby galaxies from CO emission lines (Sun et al. 2018). For velocity dispersions derived from HI in Mogotsi et al. (2016) our profiles are also higher. However, derived velocity dispersion profiles in Romeo & Mogotsi (2017) for some nearby galaxies show similar magnitudes, reaching up

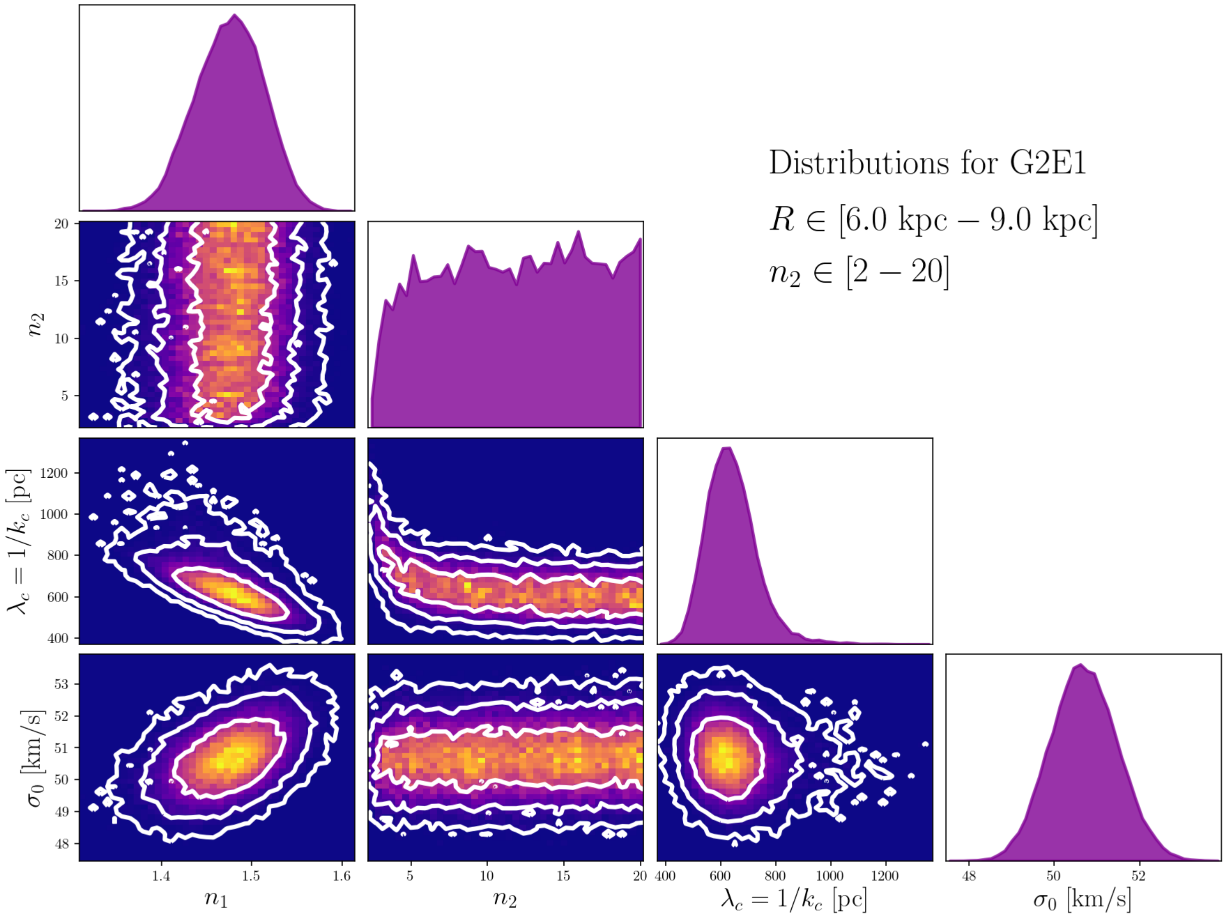

Figure 6.12: Distributions of parameters n_1, n_2, $\lambda_c = 1/k_c$, and σ_0 for run G2E1, in the radial annulus [6 kpc - 9 kpc].

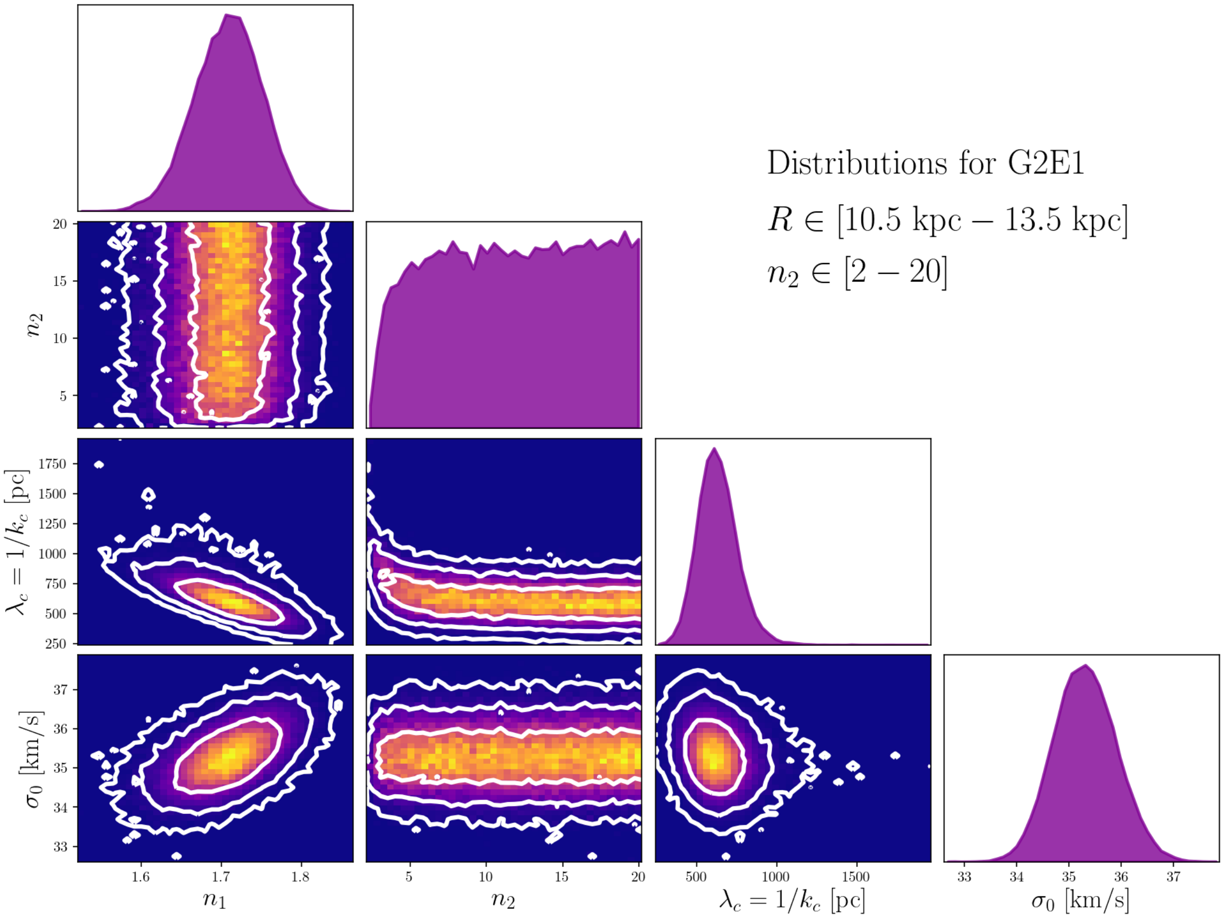

Figure 6.13: Distributions of parameters n_1, n_2, $\lambda_c = 1/k_c$, and σ_0 for run G2E1, in the radial annulus [10.5 kpc - 13.5 kpc].

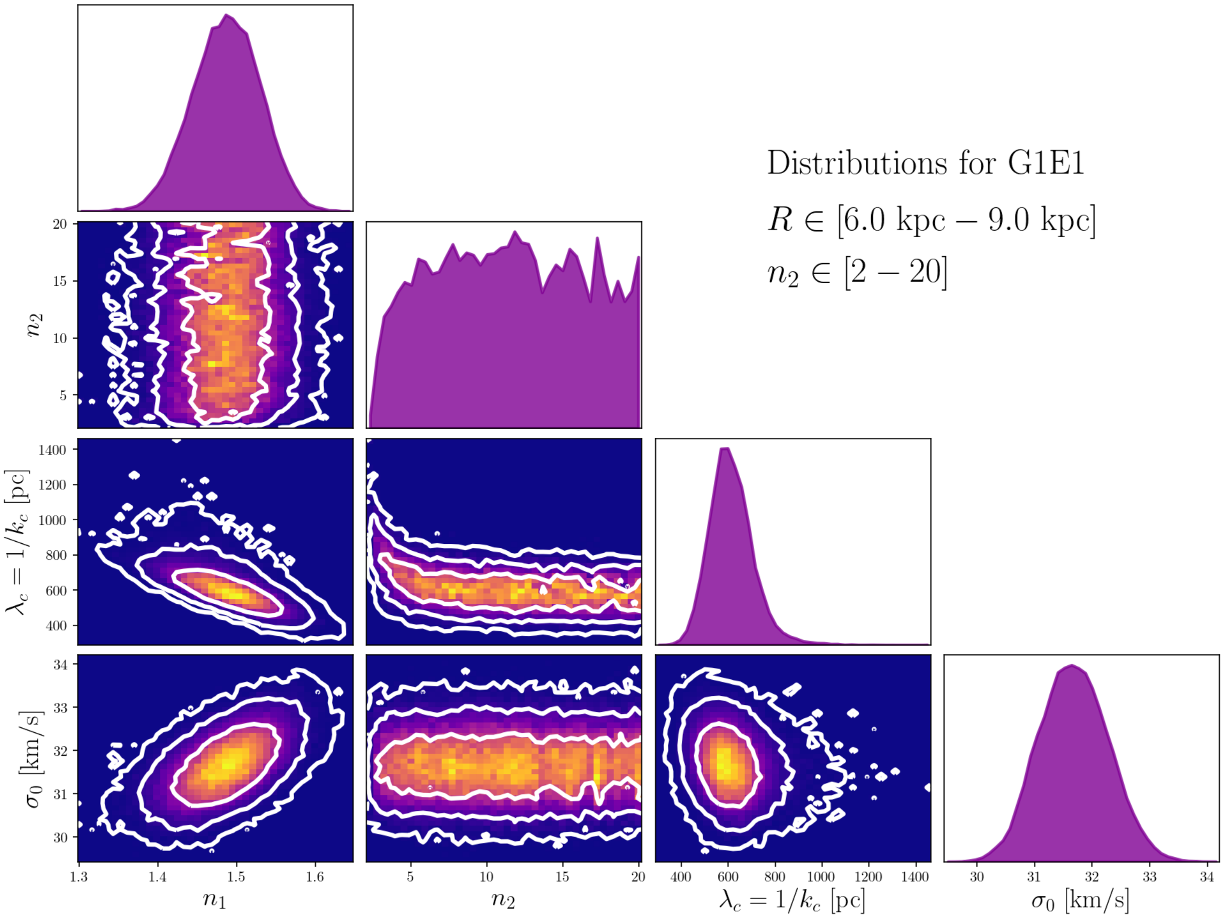

Figure 6.14: Distributions of parameters n_1, n_2, $\lambda_c = 1/k_c$, and σ_0 for run G1E1, in the radial annulus [6 kpc - 9 kpc].

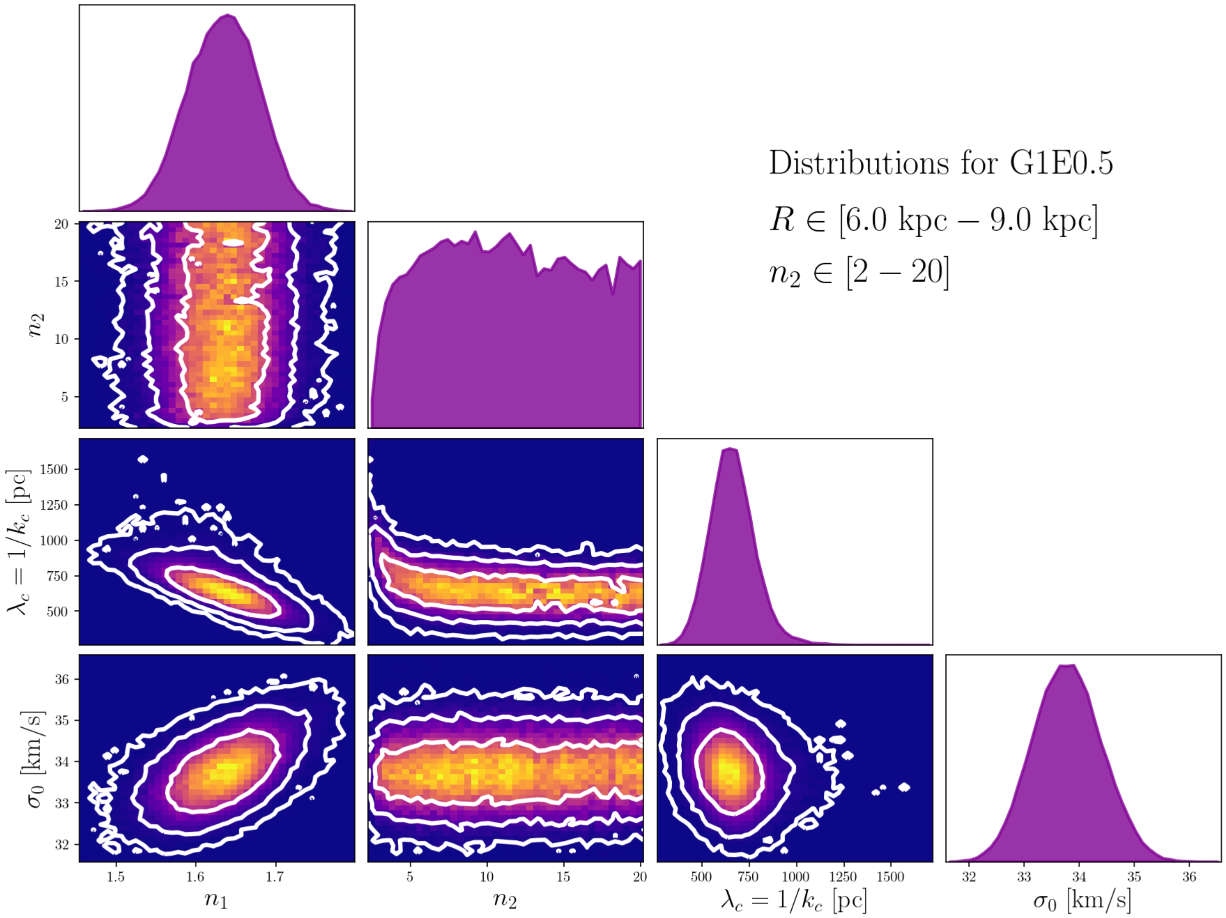

Figure 6.15: Distributions of parameters n_1, n_2, $\lambda_c = 1/k_c$, and σ_0 for run G1E0.5, in the radial annulus [6 kpc - 9 kpc].

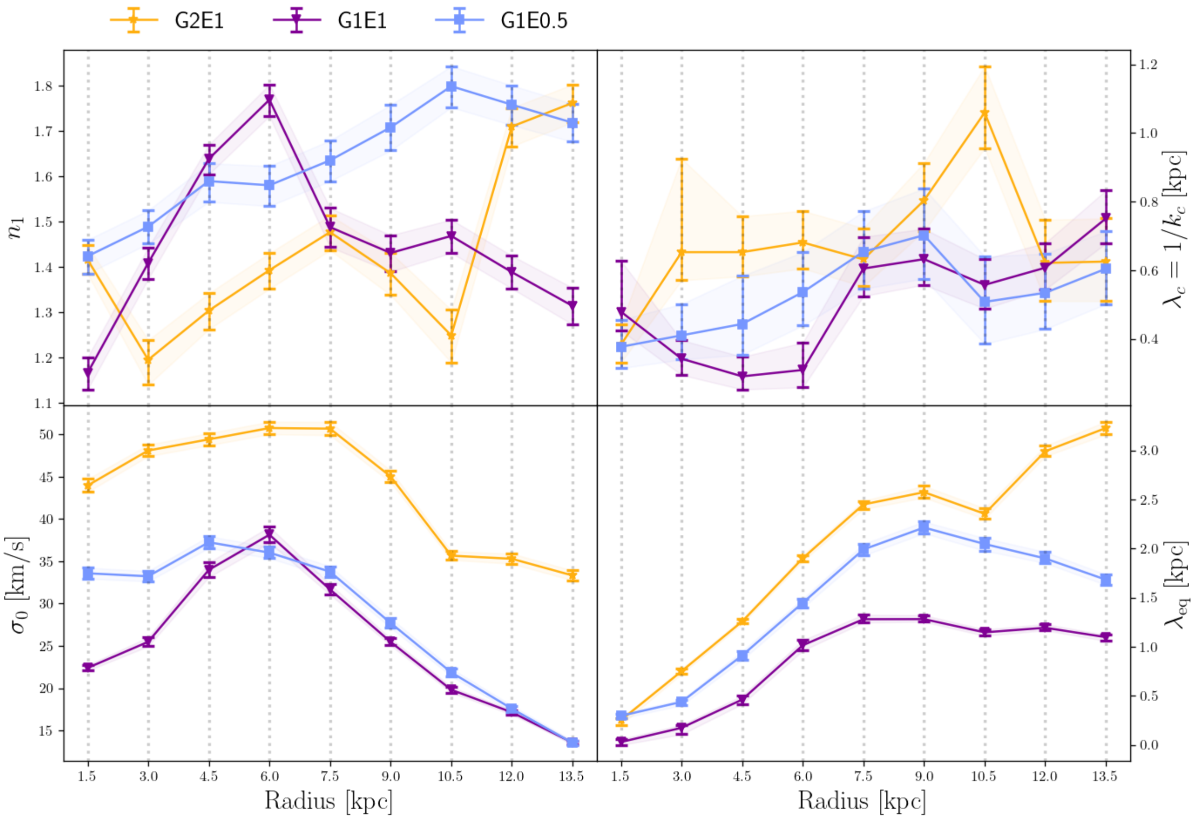

Figure 6.16: Radial profiles of the median values of the model parameters n_1, $\lambda_c = 1/k_\mathrm{c}$, σ_0 and λ_{eq}. Yellow, purple and blue colors represent runs G2E1, G1E1, and G1E0.5 respectively. Error bars represent the 16th - 84th percentile interval for each parameter.

to 50 km s^{-1} in HI and CO. In our model, σ_0 considers the velocity dispersion of the whole annular region, with velocities measured at the maximum resolution and without a density cut. Then, σ_0 has not to be understood as the average velocity dispersion for clouds in an annular region. In addition, σ_0 sets the amplitude for each component of the velocity field. Therefore we expect that the velocity dispersion of our model is a factor 1.4 higher.

Let us discuss the behaviour of the exponents n_1 and n_2. The exponent n_1 shows how the circulation is distributed on larges scales down to the scale $\lambda_c = 1/k_c$. Beyond k_c, i.e. at scales smaller than λ_c, the function $\mathcal{V}(k)$ drops quickly showing values of n_2 with no apparent upper limits. As we will see in section 6.10, we get the similar results if $\mathcal{V}(k) = 0$ for scales larger than λ_c.

We have to point out that spatial correlations in the non-circular field are given by $\mathcal{V}(k)$, and GRFs have coherent substructures unlike white noise fields. The scale λ_c could be showing the size of the coherent structures in the velocity field (Musacchio & Boffetta 2017). Coherent structures are long lived structures that can be identified in the vorticity field (Ruppert-Felsot et al. 2005) which transport mass and energy accross different scales. For scales smaller than the size of these structures, i.e. $k > k_c$, the function $\mathcal{V}(k)$ decays quickly, meaning that there is little information about the circulation field. One interpretation is that circulation or rotation is transferred from large scales down to the scale λ_c. Below the scale λ_c the redistribution of circulation from large scales stops and the distribution of γ starts to converge. At these scales, the solenoidal component of the velocity field starts to show coherent structures that are decoupled from the random behavior of the non-circular component. An observational example of this scale might be found in Rosolowsky et al. (2003), where the velocity gradients of massive of clouds within regions 500 pc are preferentially aligned. In other words, Rosolowsky et al. (2003) showed an observational correlation in the velocity field for scales smaller than 500 pc, which is similar to the values we find for λ_c.

6.5. Scales at which gas dynamics transitions from galactic rotation to non-circular motions

Now that we have obtained the distribution of the parameter we can start to answer the main question we are attempting to answer. What is the role of galactic rotation on small scales? We want to know down to what scales galactic rotation still dominates the dynamics of gas, or even molecular clouds. In our framework, this information is encapsulated in the scale $\lambda_{\rm eq}$, the scale at which the contributions to the circulation field from galactic rotation and non-circular motions are roughly the same.

The right bottom panel of Figure 6.16 shows the radial profiles of $\lambda_{\rm eq}$. Within 8 kpc from the galactic center, $\lambda_{\rm eq}$ increases with galactocentric radius, and varies between the resolution limit of 30 pc to 3 kpc. This shows that, as we get farther from the galactic center, gas dynamics at the scale of clouds is predominantly dominated by non-circular motions.

In the radial annulus centered at 7.5 kpc, G2E1 and G1E1 have similar values of $\omega_{\rm rot}$, n_1, and λ_c while G2E1 has a higher $\lambda_{\rm eq}$ by about a factor of 2. They clearly differ in the magnitude of σ_0. This suggest that for the same rotation curve differences in $\lambda_{\rm eq}$ are mainly driven by differences in σ_0. Run G2E1 has the largest values of σ_0, and likewise it has the largest values of $\lambda_{\rm eq}$. The fundamental change between these two simulations is their gas surface density. Surface density can affect σ_0 in two ways: (i) increasing non-circular motions due to the stellar feedback, and (ii) making the gas disk more unstable against gravitational fragmentation, and gravitational instabilities inject more turbulence. On the other hand, G1E1 and G1E0.5 show similar profiles for σ_0 and λ_c at large radii but $\lambda_{\rm eq}$ is larger for G1E0.5. This illustrates the effect of the rotation curve, which for G1E0.5 has a lower magnitude. In the central region of G1E1, $\lambda_{\rm eq}$ goes to zero, below the resolution of our simulations. This means that $\lambda_{\rm eq}$ is not resolved in these regions and that galactic rotation is the dominant source of circulation down to the resolution limit.

6.6. Distribution of γ

Now we show how the measured distributions of γ change with spatial scale ℓ and how our model compares with them. Figure 6.17 shows percentiles of the circulation γ and the

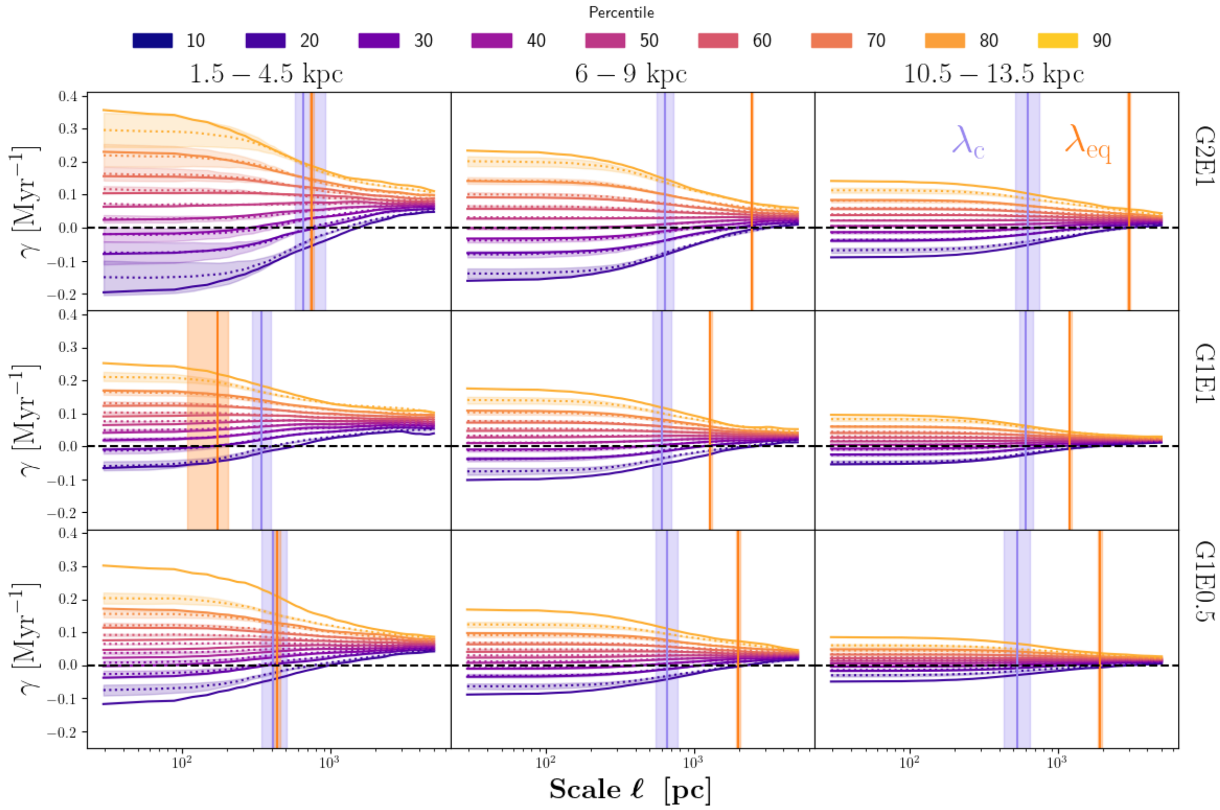

Figure 6.17: Percentiles of circulation γ at different annuli, as a function of scale ℓ for each simulation. Solid lines represent the percentiles of γ measured in the simulation. Each color shows a different percentile. Dotted lines show the percentiles of $\gamma_{\rm rot} + \gamma_{\rm nc}$ for the median values of n_1 , $\lambda_c = 1/k_{\rm c}$, and σ_0 . Shaded regions represent 1σ uncertainty intervals from the posterior distributions of the model parameters. Vertical purple and orange lines show the spatial scales $\lambda_c = 1/k_{\rm c}$ and $\lambda_{\rm eq}$ respectively, with their corresponding uncertainty illustrated by the shaded regions. Black-dashed horizontals lines represent $\gamma = 0$.

model $\gamma_{\rm rot} + \gamma_{\rm nc}$ as a function of scale for three of the nine annuli. We show the results for each individual run for all the annuli in Figures 6.18 to 6.20. Each percentile is shown with a different color. The percentiles of the measured circulation are shown as solid lines, while the models $\gamma_{\rm rot} + \gamma_{\rm nc}$ are shown by the dotted lines with their respective 1σ intervals.

Let us first discuss the general characteristics of these distributions. At the smallest spatial scale, γ is equal to the vorticity measured at the spatial resolution of the simulation. Near the galactic center the distributions of γ are much broader at every scale ℓ. This is also true for the large scale component of circulation, $\gamma_{\rm rot}$. As shown in Figure 6.8, the slope of $\omega_{\rm rot}$ decreases with radius, which means that within a annulus variations in $\omega_{\rm rot}$ also decrease with radius. We can see how the width of the distribution of γ changes from large to small scales: towards small scales it gets broader as the influence of non-circular motions becomes more important while above scales of hundreds of parsecs it starts to converge towards a constant level, set by the galactic rotation component. Figure 3.6 shows how the width of the distribution of γ looks for coherent rotation and a random field as a function of scale.

Figure 6.8 shows that ω_{rot} and consequently the probability density function of γ_{rot} are always positive, according to the chosen orientation of the z-axis. At galactic scales, γ is greater than zero since $\gamma \simeq \gamma_{\mathrm{rot}}$. On the other hand, the distribution of γ_{nc}, the GRF component, is half positive/half negative at any scale. At the scales where non-circular motions start to become important, γ starts to show negative values. This departure to negative values is not the same for every region, it depends on the magnitude of γ_{rot} and the dispersion of γ at the smallest scales, which depends on γ_{nc}. By looking at the percentile curves we see that the percentage of regions with retrograde rotation varies between 20 to 40 % at the smallest scales, with the highest fractions in G2E1. If we look at the individual distributions we can see how the fraction of regions with negative circulation at the smallest scales increases with radius until a distance of around 10 kpc, as shown in Figure 6.16 by λ_{eq}.

We show the scales λ_c and λ_{eq} in Figure 6.17. For scales smaller than λ_c the rate at which the distribution broadens starts to decrease until it stops. This is also illustrated in the examples of GRFs in Figure 3.4. With regard to λ_{eq}, we can see how λ_{eq} shifts from left to right depending on the average value of γ at large scales, and its variance at the largest and smallest scales.

We see that our model reproduces the shape of the distributions of γ as a function of ℓ, with some discrepancies at both extremes of the distributions. Figure 6.17 also displays 1σ uncertainties around the median value for our model of $\mathcal{V}(k)$. Best agreement is seen at large galactocentric radii where the distributions are better sampled since the number of cells in each annulus increases with radius. Near the galactic center we expect to observe large variations due to low sampling. In addition, it is more difficult to set a well defined center of rotation near the center of the galaxy, since the interactions with small structures can be comparable or greater than the large scale gravitational influence of the galaxy. Regardless, Figure 6.17 shows that our model can reproduce the trends in the measured distribution of $\gamma(\ell)$. This supports our assumption that the velocity field can be separated as the sum of large scale circular motions and a GRF representing non-circular motions.

Although we are able to capture the general behaviour of γ there are noticeable discrepancies. In Figure 6.17 we see a systematic discrepancy at the 90th percentile, with measured values greater than the model. In some regions we also see discrepancies at the 10th percentile. These discrepancies are more noticeable at small radii for runs G1E1 and G1E0.5 as shown in Figures 6.19 and 6.20.

In the first and second panels of Figures 6.19 and 6.20, we see a less symmetry with respect to the median, and a distribution that is broader than our model. This shows that the extreme values of γ coming from non-circular motions are not represented in our model. One possibility is that within an annulus the model parameters change quickly. In our model, we are assuming a unique Gaussian distribution for each radial bin instead of a superposition of Gaussian distributions for each radius. However, in this scenario, the distributions of γ should be more symmetric. In some regions the deviation from the model of the 90th percentile is higher compared to the 10th percentile. This asymmetry is likely to come from errors in our modeling of ω_{rot}. There may be other large scale motions driven by galactic rotation that would tend to present positive values of circulation. Some of the discrepancies could be explained by regions under collapse: when high density regions collapse, their vorticity ω

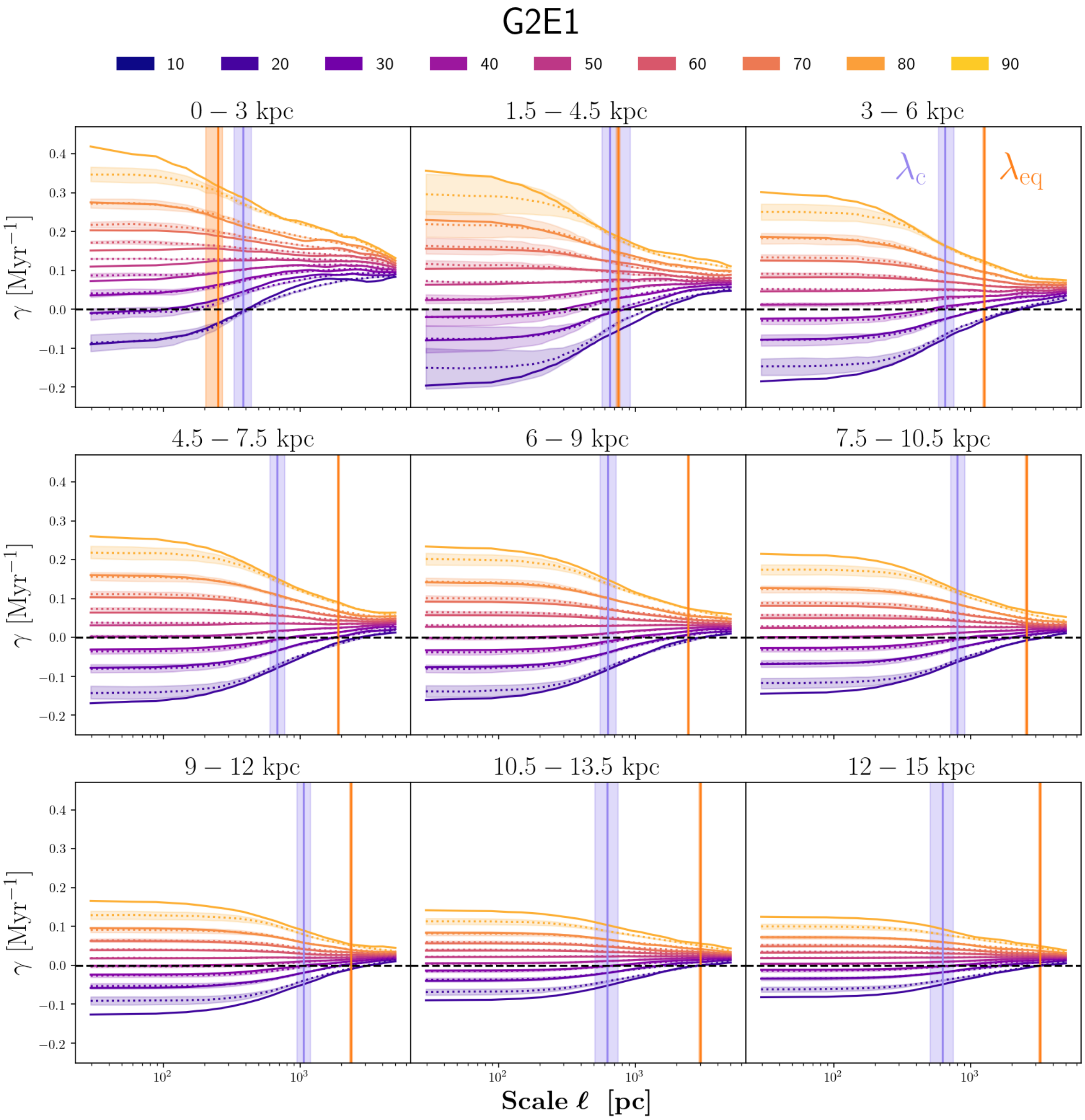

Figure 6.18: G2E1: Percentiles of circulation γ at each annuli, as a function of scale ℓ.

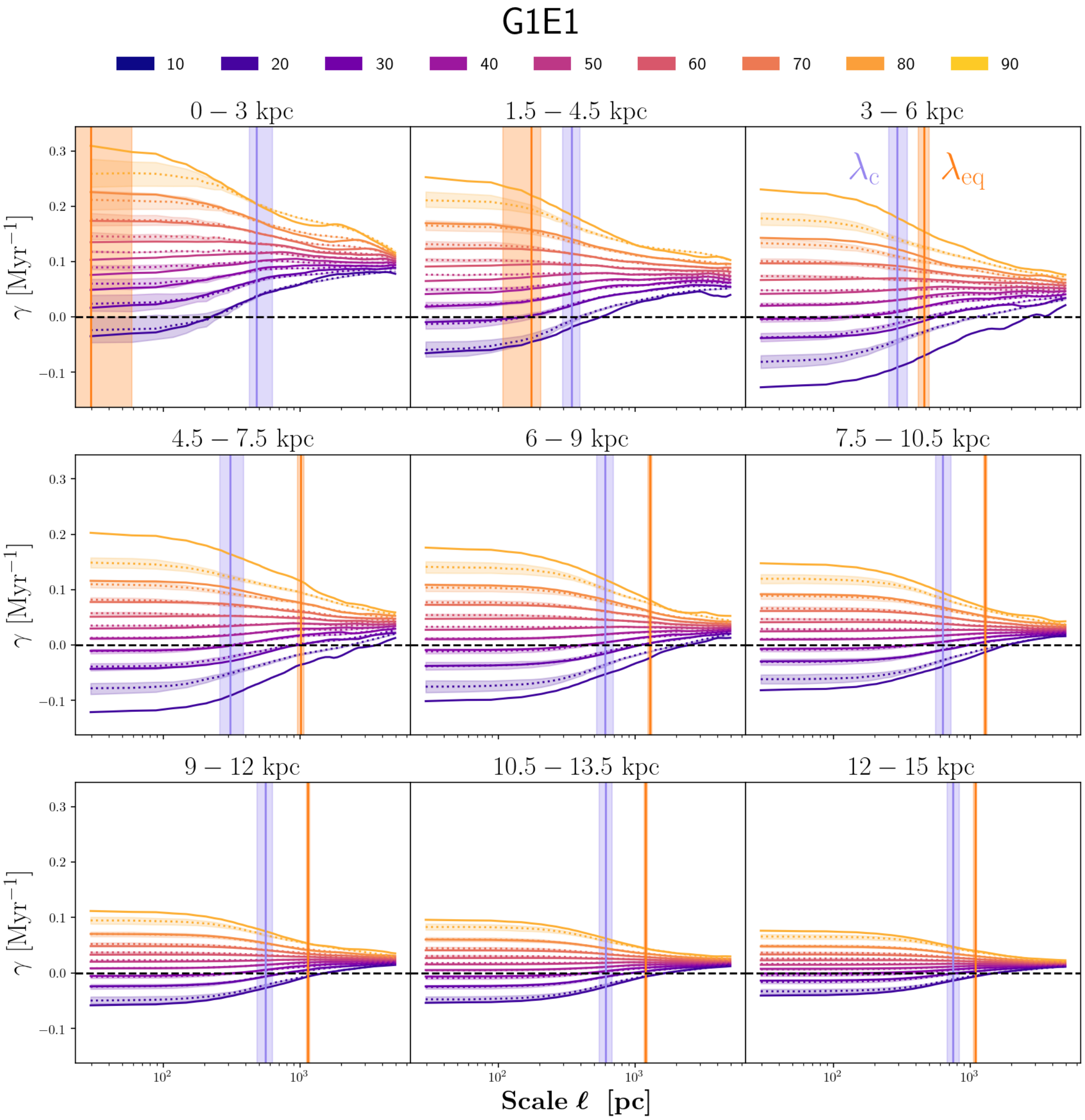

Figure 6.19: G1E1: Percentiles of circulation γ at each annuli, as a function of scale ℓ.

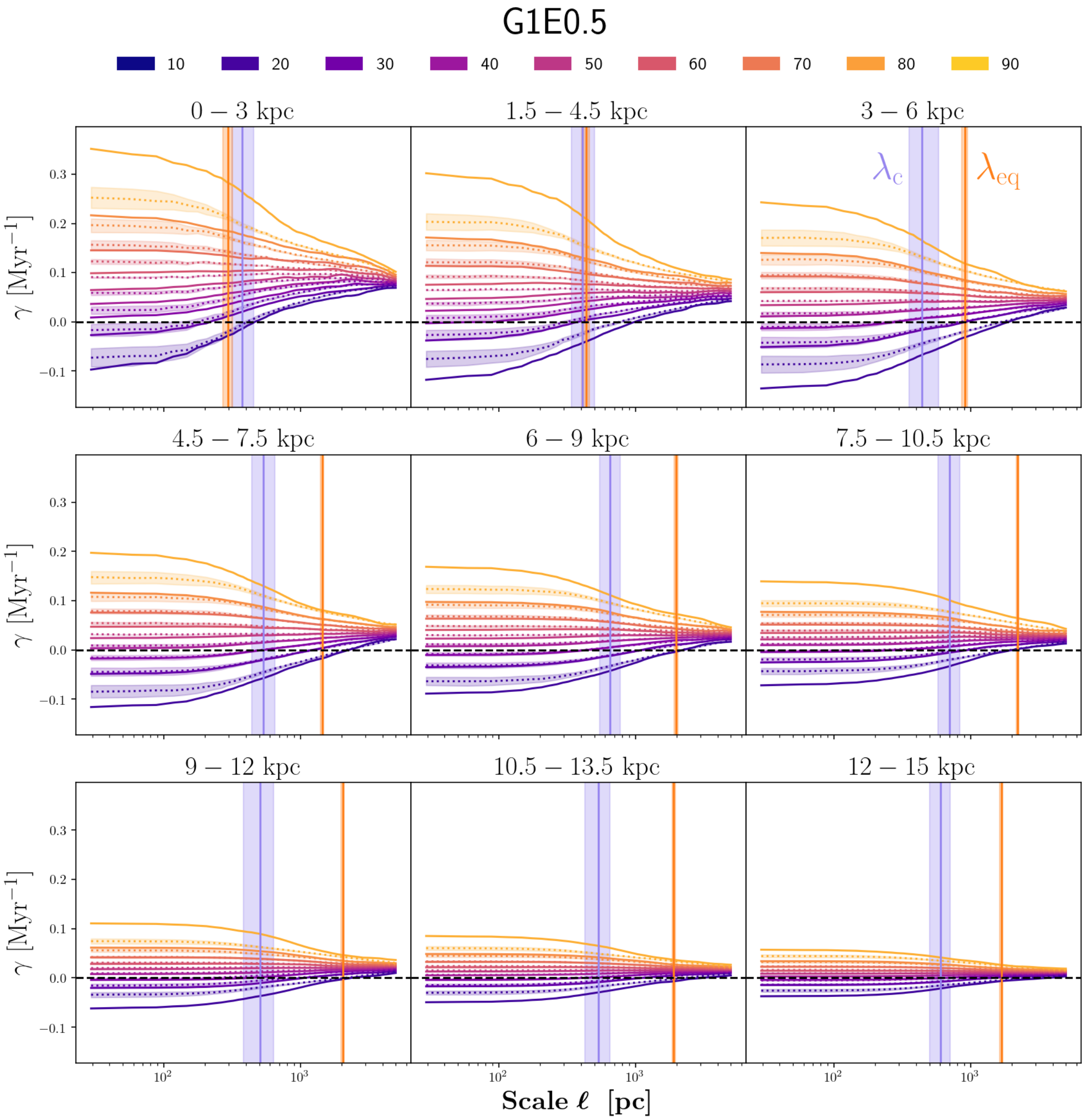

Figure 6.20: G1E0.5: Percentiles of circulation γ at each annuli, as a function of scale ℓ.

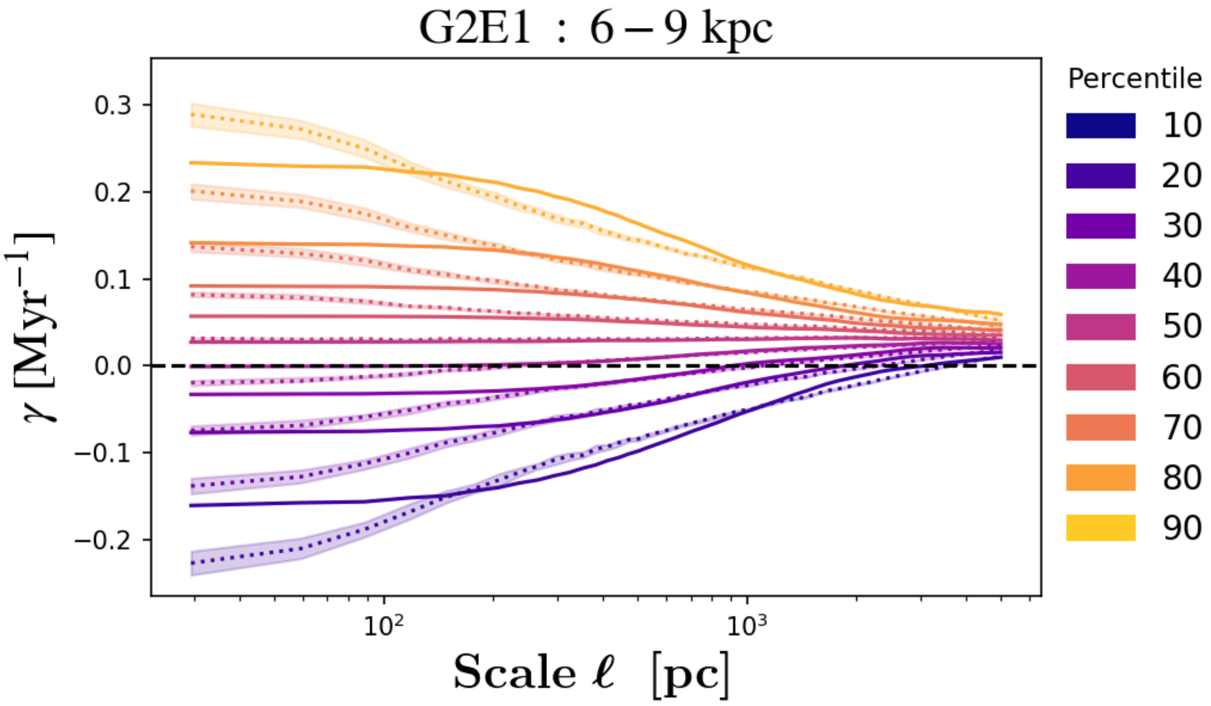

Figure 6.21: Percentiles of $\gamma = \gamma_{\rm rot} + \gamma_{\rm nc}$ as a function of the scale ℓ, for a single power law $\mathcal{V}(k)$ from $k_{\rm min} = 4/L$ to $k_{\rm max} = 1/4\Delta x$. Solid lines show the percentiles of γ measured in the simulations. Dotted lines show the percentiles of $\gamma_{\rm nc}$ and the shaded regions correspond to 1σ uncertainties.

increases in magnitude. Kruijssen et al. (2019) found that simulated molecular clouds with higher densities show higher velocity gradients. By checking the velocity divergence in the x-y plane, i.e. $\nabla_{xy} \cdot \vec{v} = \frac{{\rm d}v_x}{{\rm d}x} + \frac{{\rm d}v_y}{{\rm d}y}$, we find that between the percentiles 20 % to 80 % of ω the median value of $\nabla_{xy} \cdot \vec{v}$ is close to zero. However, at the extremes of the distribution of ω, $\nabla_{xy} \cdot \vec{v}$ drifts to negative values. Once a cloud of gas starts to collapse, $\nabla \cdot \vec{v} < 0$, the magnitude of ω increases. It might be possible to address this discrepancy by considering the conservation of angular momentum or the conservation of circulation, but that is beyond the scope of this work.

Interestingly, run G2E1, which has a higher gas content, shows more symmetric distributions of γ and less discrepancies between the observed and modeled distributions. One possibility is that in this galaxy deviations from the rotation curve are dominated by stellar feedback since it has a higher star formation rate. We expect the distribution of circulation, coming from this source of non-circular motions, to be more symmetric.

As mentioned before, our model captures the distribution of circulation at different spatial scales. One way to show this is to compare the measured distributions of γ assuming a different model of $\mathcal{V}(k)$. We show in Figure 6.21 an example of the percentiles obtained by using a function $\mathcal{V}(k)$ with a single power-law from $k_{\rm min} = 4/L$ to $k_{\rm max} = 1/4\Delta x$. We see that without the inclusion of the break at k_c or a variable $k_{\rm max}$ the model is unable to reproduce the plateau of the percentiles at the smallest scales.

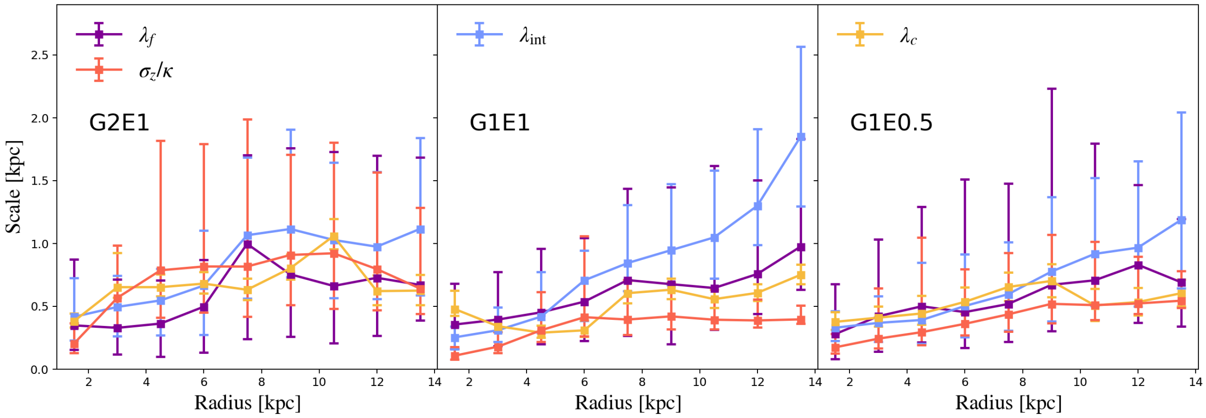

Figure 6.22: Comparison between λ_c and characteristic spatial scales of gas clumps measured in the simulations. The orange line shows the epicyclic scale as a function of galactocentric radius. The purple line represents the length scale of fragmentation $\lambda_f = (M_c/\Sigma_{\rm gas})^{1/2}$. The blue line shows the characteristic separation between clumps, $\lambda_{\rm int}$. Error bars represent the 16th - 84th percentile interval for each parameter.

6.7. Relation with other spatial scales

The next step is to link the structures in the velocity field with structures in the density field. One of the first scales that should affect the behavior of the velocity field is the scale height. However, the scale height of the gas density field for the three runs is of the order of 100 pc, which is usually smaller than λ_c by a factor of 4-5. We continue analyzing different structures that exist in the plane of galactic disks.

Let us assume that the scale λ_c is related with the fragmentation of gas with a characteristic scale λ_f. If $\Sigma_{\rm gas}(R)$ is the gas surface density profile we can estimate a characteristic mass for the fragments or clumps as $M_c \approx \pi\Sigma_{\rm gas}(\lambda_f/2)^2$, then the scale of fragmentation is approximated by:

$$\lambda_f \approx \left(\frac{M_c}{\Sigma_{\rm gas}}\right)^{1/2} \tag{6.10}$$

The scale λ_c could also be related with interactions between clumps (Dobbs & Pringle 2013). If cloud-cloud interactions play a role, it is worth studying the typical distance between clumps of gas at each radius.

To compute the two aforementioned scales we need to define a clump of gas. We use the following criteria to define a gas clump:

- Each cell in the clump has a number density above 100 cm^{-3}.
- Clumps are gravitationally bound.
- Clumps have a minimum of 20 cells (a $3 \times 3 \times 3$ cube without the corners has 19 cells).

The clumps identified by these criteria have typical sizes of 100 pc, while in nearby galaxies sizes range between 10 and 100 pc (Rosolowsky 2007; Heyer et al. 2009; Colombo et al. 2014). These sizes are of the order of the scale height across the disk for the three runs. We measure M_c as the total gas content in the clump. To compute the typical distance, we do the following: for each clump we average the distance to the three closest clumps and we average that quantity at each annulus. We refer to this scale as $\lambda_{\rm int}$.

We show λ_f and $\lambda_{\rm int}$ in Figure 6.22. For most regions, $\lambda_{\rm int}$ and λ_f are of the same order of magnitude and they appear to be correlated. The spatial scale λ_c seems to lie closer to λ_f. However, the scatter of these scales is too large to derive any strong conclusion. Each annulus has a characteristic $\Sigma_{\rm gas}$, Ω and σ_v, quantities that are dynamically correlated. In that regard it is not surprising that spatial scales defined by these quantities show similar behaviors.

Another scale related with a change of the behavior of the velocity field is the epicyclic scale σ_v/κ (Meidt et al. 2018), where σ_v is the velocity dispersion of a gas cloud, and κ is the epicyclic frequency. Epicyclic motions correspond to the evolution to small perturbations of circular orbits under the gravitational potential of the galaxy. Structures larger than their corresponding epicylic scale are ensured to be affected by the galactic potential. Figure 6.22 shows σ_z/κ as the orange solid line, where σ_z corresponds to the dispersion velocity in the z-axis in a radial bin. The choice of $\sigma_v = \sigma_z$ assumes that once a structure has formed its velocity dispersion is nearly isotropic. Like the scales λ_f and $\lambda_{\rm int}$, the epicyclic scale lies close to λ_c.

The physical correlations between all these scales and their level of uncertainty make difficult to compare them with λ_c. Therefore, we are not able to elucidate the fundamental physical origin of λ_c. We can only conclude that λ_c is related with the formation of structure in our simulations and that the details of gas dynamics below such structures do not significantly affect the overall circulation of gas.

6.7.1. Circulation scales: λ_c and $\lambda_{\rm eq}$

We start this section discussing the role that gravitational instabilities can play setting the distribution of circulation, particularly their effect in λ_c and $\lambda_{\rm eq}$. First, we recall the Toomre parameter, $Q = \kappa\sigma_v/\pi G\Sigma$, which for marginal stable systems ($Q \approx 1$). If we set κ at a fixed value κ_0, marginal stability requires $\sigma_v = \pi G\Sigma/\kappa_0 \propto \Sigma$. At the scales of clouds, the relevant parameter is the virial parameter $\alpha_{\rm vir}$, which for nearly spherical clouds can be expressed as (Sun et al. 2018)

$$\alpha_{\rm vir} = \frac{5\sigma_v^2 R}{fGM}. \tag{6.11}$$

where M is the cloud mass, R is the cloud radius, σ_v is the one-dimensional velocity dispersion, and f is a geometrical factor that quantifies the density structure inside the cloud. For clouds with $\alpha_{\rm vir} \approx 1$ we get

$$\sigma_v = \sqrt{\frac{f\alpha_{\rm vir}G\pi}{5}}\sqrt{R\Sigma}. \tag{6.12}$$

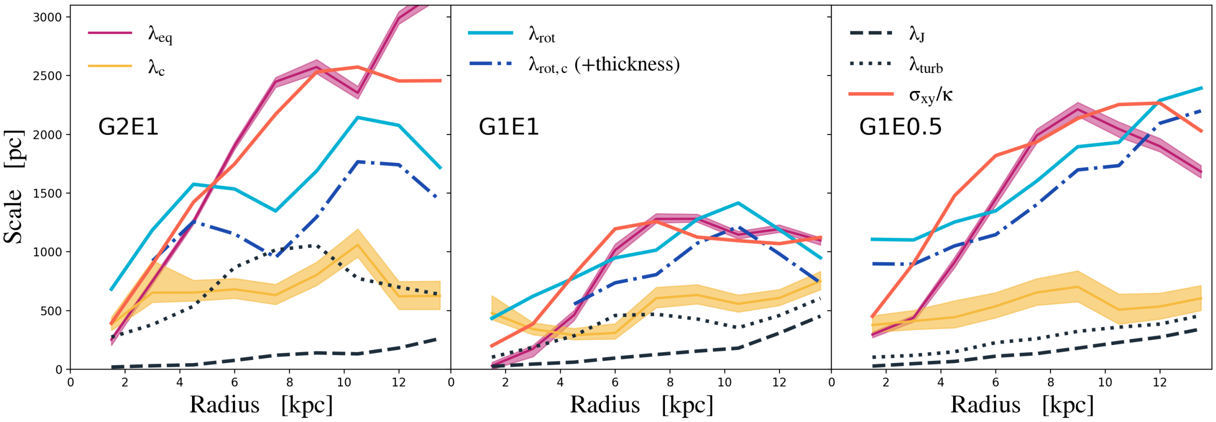

Figure 6.23: Spatial scales as a function of galactocentric radius: solid pink and yellow lines correspond to $\lambda_{\rm eq}$ and λ_c respectively. The shaded regions correspond to 1σ uncertainties. The classical instability scales for two dimensional disks, $\lambda_{\rm rot}$ and $\lambda_{\rm J}$, are shown as solid light-blue lines and black dashed lines respectively. The dot-dashed line shows the effective values $\lambda_{\rm rot}$ after adding the effects of resolution.

Therefore, for virialized clouds of constant size, we expect that σ_v grows with $\sqrt{\Sigma}$. For any of these two pictures, we expect that galaxies with higher column densities have more randomness in their velocity fields. This is illustrated by the run G2E1 in Figure 6.16, which shows higher values of σ_0 and $\lambda_{\rm eq}$ compared to the other runs.

Since we are dealing with galactic disks, the first step to visualize relations with gravitational instabilities is to compute $\lambda_{\rm rot}$, and the two-dimensional thermal Jeans scale $\lambda_{\rm J}$, given by $c_s^2/G\Sigma$, where c_s is the gas sound speed and Σ is the gas surface density. The thermal Jeans scale sets the size of the smallest structures that can be formed. Both length scales, $\lambda_{\rm rot}$ and $\lambda_{\rm J}$, are shown in Figure 6.23. Because the stability of a quasi two-dimensional fluid is affected by the disk thickness, or the resolution in the case of simulations, we have to consider the dispersion relation $\omega_p^2(k) = \kappa^2 - 2\pi G\Sigma|k|{\rm e}^{-k\epsilon}$, where ω_p is the frequency of perturbations and ϵ is the disk thickness with a minimum value set by the numerical resolution (Binney & Tremaine 2008, p. 552). Perturbations where $\omega_p^2(k) < 0$ correspond to instabilities. At the limit of marginal stability $\omega_p(k) = 0$, and $D(k) = \kappa^2 - 2\pi G\Sigma|k|{\rm e}^{-k\epsilon} = 0$. The function $D(k)$ is a convex function with its minimum value satisfying $\partial D(k)/\partial k = 0$. Assuming $k > 0$

$$\frac{\partial D(k)}{\partial k} = 0 \rightarrow k = \epsilon^{-1} \ . \tag{6.13}$$

The minimum value of $D(k)$ indicates the most unstable wavenumber k. For a disk to be stable, we need $D(\epsilon^{-1}) > 0$. This translates in the condition:

$$\epsilon > \frac{2\pi G\Sigma}{{\rm e}\kappa^2} = \frac{1}{2\pi{\rm e}}\lambda_{\rm rot}. \tag{6.14}$$

This means that a disk can be fully stabilized by rotation, and its resolution or disk thickness. To obtain the correct values of $\lambda_{\rm rot}$, that we call $\lambda_{\rm rot,c}$, we solve the equation $\omega_p^2(k) = 0$. We plot $\lambda_{\rm rot,c}$ in Figure 6.23 as the dot-dashed blue line. Once the disk thickness is considered, near the galactic centers equation 6.14 is fulfilled and any radial perturbation is stable against fragmentation. This means that in the inner regions of these galaxies gravitational instabilities are not resolved. At these scales we do not expect to see an important injection of energy due to gravitational instabilities. The effect of the disk thickness is more noticeable in our additional simulations in Figure 6.28: If $\lambda_{\rm rot,c}$ is not resolved $\lambda_{\rm eq}$ falls below the resolution of the simulations.

For this set of simulations, λ_c lies between $\lambda_{\rm J}$ and $\lambda_{\rm rot,c}$, that is, within the range of scales in which gravitational instabilities can exist, consistent with this scale being associated with scales of structure formation. For all runs we see that $\lambda_{\rm eq}$ is above $\lambda_{\rm J}$, it increases with radius, and in some regions is higher than $\lambda_{\rm rot,c}$. Since $\lambda_{\rm rot,c}$ is the maximum size of unstable perturbations, clouds formed in regions where $\lambda_{\rm eq} > \lambda_{\rm rot,c}$ will be predominantly dominated by non-circular motions.

For all runs we see that $\lambda_{\rm eq}$ can show values up to kiloparsec scales. For G2E1, $\lambda_{\rm eq}$ is higher than $\lambda_{\rm rot}$ in most regions. This is probably caused by the high star formation rate, due to its higher gas content densities, and associated increase in feedback-induced non-circular motions. In Figure 6.28, our simulations with only supernova feedback show values of $\lambda_{\rm eq}$ lower than $\lambda_{\rm rot}$ and lower than λ_c. This last point shows that only considering the difference in gas content between simulations without taking into account stellar feedback is insufficient to explain differences in $\lambda_{\rm eq}$ across the different runs. These additional simulations also show and apparent correlation between $\lambda_{\rm eq}$ and $\lambda_{\rm rot}$. However, once we use a more energetic type of feedback $\lambda_{\rm eq}$ grows and this apparent correlation disappears. This suggest that there might be two different regimes where the distribution of circulation is set by gravitational instabilities or by stellar feedback. This idea goes in line with results from numerical simulations and analytical models showing that turbulence can be powered by gravity or stellar feedback, and that the dominant driver of turbulence changes across the evolution of the Universe (Goldbaum et al. 2015; 2016; Krumholz & Burkert 2010; Krumholz et al. 2018)

Since we are discussing the turbulent behavior of gas and its dynamical stability, we can also discuss the relevance of the turbulent Jeans scale $\lambda_{\rm turb} = \sigma_v^2/G\Sigma$, with σ_v is the velocity dispersion of gas considering non-thermal motions. However, σ_v is a function of scale ℓ (Elmegreen & Scalo 2004; Romeo et al. 2010) and to properly take into account the effects of turbulence we need know how σ_v changes with ℓ. Here we take a first order approach considering $\sigma_v = (c_s^2 + \sigma_z^2)^{\frac{1}{2}}$, where σ_z is the mass-weighted vertical dispersion velocity in the disk of the galaxy. In this approximation, we are assuming that the velocity dispersion at the scale of the disk sale-height is a representative value of the velocity dispersion for bound structures in presence of turbulence. To compute $\lambda_{\rm turb}$ we use a temperature cut of $T < 5000$ K to avoid considering gas that is currently affected by stellar feedback. We show $\lambda_{\rm turb}$ in Figure 6.23. For runs G2E1 and G1E1 $\lambda_{\rm turb}$ is of the order of λ_c which suggest that λ_c could be tracing the scales at which turbulent structures are affected by their self-gravity. This is not shown by run G1E0.5, but we need to keep in mind that we are assuming that σ_z^2 is a good proxy for the turbulent velocity in the plane of the galaxy for self-gravitating structures.

In the field of fluid dynamics, it is known that in turbulent fluids coherent structures naturally arise, and that these structures are fundamental for the transport of angular momentum across different scales (Kraichnan 1967; Ruppert-Felsot et al. 2005). These studies motivates us to look for structures which can be defined by kinematics only. One alternative is to look for structures which behavior is defined by the ratio between the galactic angular velocity that traces the galactic potential, and the local non-circular motions at cloud scales. A spatial scale that goes in that direction and compares the magnitudes of the velocity dispersion of gas and the galactic potential is the epicyclic scale σ_v/κ (Meidt et al. 2018). However, as shown in Figure 6.22, if we use the velocity dispersion across the z-axis the epicyclic scale is of the order of λ_c, which in most regions is smaller than $\lambda_{\rm eq}$. Another approach is to consider the velocity dispersion in the $x-y$ plane, σ_{xy}, within a radial bin. To compute σ_{xy} we subtract the circular velocity model to the velocity field. The scale σ_{xy}/κ compares the energy in the non-circular velocity field with respect to epicyclic motions given by the galactic potential. We show the spatial scale σ_{xy}/κ in Figure 6.23 as the orange line.

Figure 6.23 shows that σ_{xy}/κ is similar to $\lambda_{\rm eq}$. This result would suggest that the ratio σ_{xy}/κ is a good proxy for $\lambda_{\rm eq}$. However, this might be valid only for our feedback prescription and for galaxies with an average star formation rate according to the Kennicutt-Schmidt relation (Kennicutt 1998; Daddi et al. 2010). For our second set of simulations with only SN feedback, the values of $\lambda_{\rm eq}$ are usually lower than σ_{xy}/κ and λ_c. This again shows the effect of using different feedback prescriptions. Momentum feedback prescriptions change the velocity field more aggressively, $\lambda_{\rm eq}$ shows large values and is similar to σ_{xy}/κ.

We can interpret this difference as differences in the sources of non-circular motions. Simulations with only thermal supernova feedback can lose this source of energy quickly due to our resolution of 30 pc, producing a lower effect in the velocity field. In this scenario, gravitational instabilities might become a relevant source of non-circular motions or turbulence. On the other hand, the stellar feedback prescription used in our main simulations changes explicitly the velocity field at the smallest scales and increases directly the magnitude of $\mathcal{V}(k)$. Feedback might erase the correlation between gravitational instabilities and the non-circular motions at small scales.

This point has implications for the analysis of star formation in numerical simulations. In simulations with mechanical stellar feedback, i.e. momentum injection, the velocity field is explicitly changed and the amount of kinetic energy at small scales increases. This reduces the coupling between the dynamics of clouds and galactic rotation, and also the coupling between the efficiency of star formation and the galactic environment. The magnitude of correlations between star formation and galactic properties found in simulations might depend on the specific stellar feedback prescription used.

Up to this point we have showed that the distribution of circulation is affected by stellar feedback and gravitational instabilities. It is interesting to discuss what other studies have shown respect to the distribution of circulation or rotation. Here we mention the works of Tasker & Tan (2009) and Ward et al. (2016), that used simulations to measure how the rotation of molecular clouds aligns with respect to the rotation of their galaxies. These simulations have similar surface gas densities and the same shape of the velocity curve, but with different magnitudes. Both simulations have weak forms of feedback; Tasker & Tan (2009) did not include stellar feedback in their simulations, and the simulations in Ward et al. (2016) had a reduced feedback efficiency of 10 %. Hence, we expect that their distribution of circulation is set by gravitational instabilities. For comparison, at a galactocentric radius of 8 kpc, $\lambda_{\rm rot} \simeq 2100$ pc in Tasker & Tan (2009), and $\lambda_{\rm rot} \simeq 1500$ pc in Ward et al. (2016).

In addition, the simulation of Ward et al. (2016) shows spiral structures while the density field in Tasker & Tan (2009) is more random. The simulation of Tasker & Tan (2009) is more unstable than the one from Ward et al. (2016) and consequently the former should have higher values of λ_{eq}, or a higher fraction of molecular clouds with retrograde rotation respect to their galaxy. These simulations effectively find different fractions of retrograde clouds, 30 % in Tasker & Tan (2009) and 13 % Ward et al. (2016) respectively. This shows that more unstable systems are more dominated by non-circular motions and have higher values of λ_{eq}. Tasker & Tan (2009) also analyzed the effects of resolution, which directly influences the size of molecular clouds and the stability of gas dynamics as shown by $\lambda_{\mathrm{rot,c}}$. Tasker & Tan (2009) show that as the resolution is increased more molecular clouds present retrograde rotation. In summary, these studies show that in the absence of strong feedback, gravitational instabilities play a role setting how circulation is distributed at smaller scales, and also show the relevance of the spatial resolution used in numerical simulations.

6.8. Power Spectrum

We can analyze the dynamics across different scales by means of the power spectrum $E(k)$. To compare our results with the findings of experimental studies of thin fluid layers, we compute the power spectrum of the two dimensional velocity field $\vec{V}(x,y) = u_{2D}(x,y)\hat{\imath} + v_{2D}(x,y)\hat{\jmath}$, obtained by

$$u_{2D}(x,y) = \frac{\int \rho(x,y,z)u(x,y,z)}{\int \rho(x,y,z)\mathrm{d}z} \quad \& \quad v_{2D}(x,y) = \frac{\int \rho(x,y,z)v(x,y,z)}{\int \rho(x,y,z)\mathrm{d}z}. \tag{6.15}$$

We obtain the Fourier transforms $\tilde{u}_{2D}(k) = \mathcal{F}(u_2D)$ and $\tilde{v}_{2D}(k) = \mathcal{F}(v_2D)$. The power spectrum $E(k)$ is defined as $\frac{1}{2}(\tilde{u}_{2D}(k)^2 + \tilde{v}_{2D}(k)^2)k$, such that $\int E(k)\mathrm{d}k$ is the average kinetic energy per unit mass of the two dimensional field.

We show the power spectrum for our simulations in Figure 6.24. We have normalized $E(k)$ by $k^{-5/3}$, that means that a curve with a slope close to zero in Figure 6.24 represents a $k^{-5/3}$ power-law. From 5 kpc to around 1 kpc $E(k)$ shows a slope consistent with the inverse energy cascade of two dimensional fluids. For scales lower than 500 pc $E(k)$ shows steeper power-laws. Run G1E0.5 shows a power-law k^{-3} down to 100 pc, while G2E1 and $G1E1$ fall more quickly. The curves of G1E1 and G1E0.5 in Figure 6.24 flatten towards scales smaller than 100 pc. This has been observed in the power spectrum of thin fluids, where at scales smaller than the thickness of the fluid layer an energy cascade with $E(k) \propto k^{-5/3}$ appears.

In this formalism, the inverse energy and the direct enstrophy cascade are represented by $n_1 = 4/3 \approx 1.33$ and $n_2 = 2$ for our function $\mathcal{V}(k)$. As shown in Figure 6.16, the distribution for the exponent n_1 ranges between 1.1 and 1.8. This exponent lies close to the expected values of both regimes. On the other hand, n_2 which should be associated with the enstrophy cascade has no upper limit in our model and the scale where $\mathcal{V}(k)$ breaks, λ_c, is of the order of 240 to 1 kpc. If we look the middle panel of Figure 3.5 in section 3.1.5, we see that for high values of n the distribution of γ starts to be less sensitive to changes in n. It is likely that most of the information of the distribution of γ is given by n_1 and k_c. If this is the case, k_c is related with the turbulent forcing scale k_f. Experiments of thin layer fluids show strong

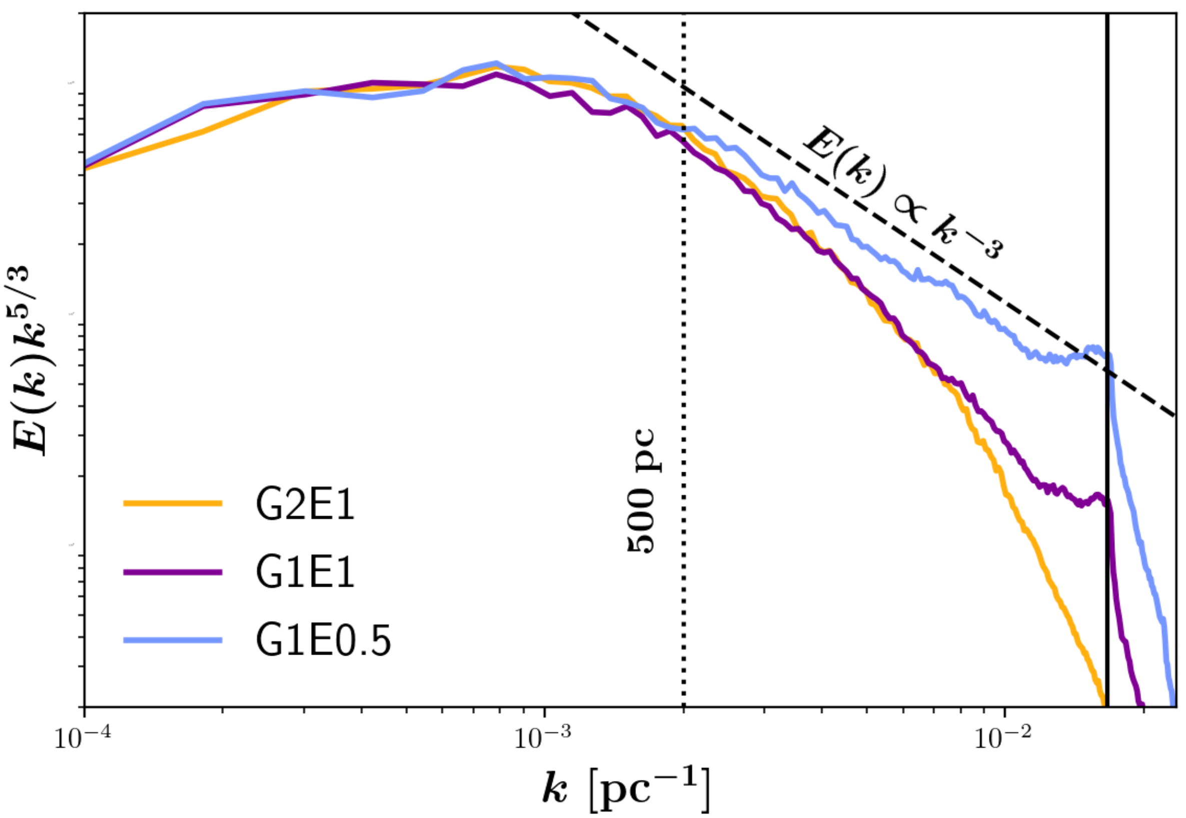

Figure 6.24: Kinetic energy power spectrum $E(k)$ normalized by $k^{-5/3}$. In this plot a flat curve represents the inverse energy cascade for two-dimensional turbulence. The black dashed line shows the slope of the expected enstrophy cascade. The black vertical line lies at $k = 1/(2\Delta x)$, where Δx is the spatial resolution.

long-lived vortices at the scale $\lambda_f = 1/k_f$ (Musacchio & Boffetta 2017). Then, the turbulent picture also suggest that λ_c might be related with the formation of structure in the turbulent velocity field.

6.9. Low feedback simulations

In this section we show the results for the simulations with supernova feedback only. Since these simulations have a lower stellar feedback we add the suffix "low"to distinguish them from the simulations presented in the main text.

These runs have a lower energy input coming from stellar feedback. Therefore, their SFR efficiency is higher and at the time of comparison the additional simulations have less mass in gas. Runs G2E1, G1E1, and G1E0.5 have 2.9, 1.3, and 1.4 times more gas than G2E1-low, G1E1-low, and G1E0.5-low respectively. Particularly, G2E1 has $1.8 \times 10^{10} M_\odot$ of gas in the disk, while all the other runs have below $1 \times 10^{10} M_\odot$ in gas. This makes G2E1 the most unstable disk at this point of time. This might explain why G2E1 shows the largest values

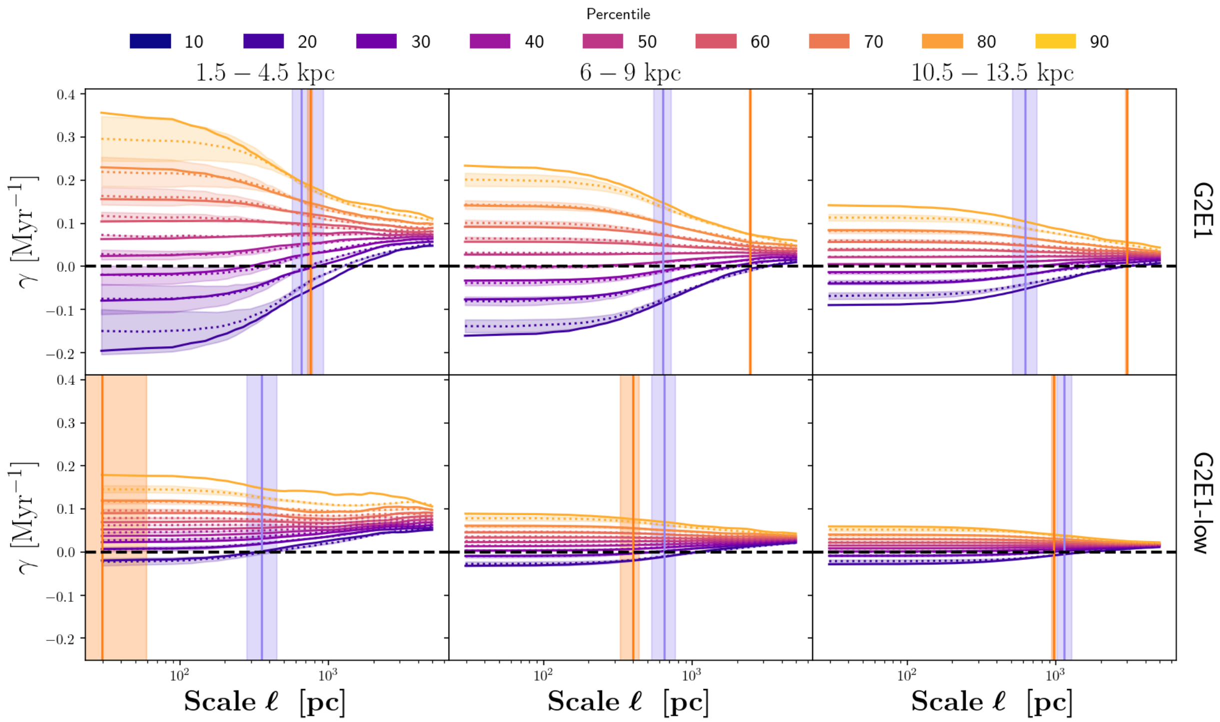

Figure 6.25: Percentiles of circulation γ within [1.5-4.5] , [6-9] and [10.5-13.5] kpc for G2E1 and G2E1-low, as a function of scale ℓ. Solid lines represent the percentiles of γ in the simulation while dashed regions represent 1σ uncertainty intervals for the model $\mathcal{V}(k)$ around the median values, showed as dotted lines. Vertical lines show the spatial scale $\lambda_c = 1/k_{\rm c}$ and its corresponding uncertainty illustrated by the dashed region. Black-dashed horizontals lines show $\gamma = 0$.

of σ_0 which translates into higher values of $\lambda_{\rm eq}$.

In Figures 6.25 to 6.27 we compare the distributions of γ for our main runs and their low stellar feedback counterparts. The former runs shows broader distributions of γ, and their fraction of regions with retrograde rotation slightly higher. However, as pointed out before, the comparison is not straightforward since the low-feedback runs have less mass in gas compared to the main runs. For these simulations we also see high discrepancies between our model and the measured distribution of γ in the central regions of galaxies. These deviations occur at the 90-th percentiles of γ.

We see slight changes of λ_c caused by changes in stellar feedback. The main difference is seen for $\lambda_{\rm eq}$. For all the regions shown in Figures 6.25-6.26 $\lambda_{\rm eq} < \lambda_c$. This implies that, without the proper treatment of stellar feedback, the kinematics of gas at scales smaller than the height scale of simulations are affected by the rotation curve or potential of the galaxy. For some of the regions $\lambda_{\rm eq}$ is not resolved.

In Figure 6.28 we show the scales $\lambda_{\rm eq}$, λ_c, and the scales of gravitational instability for G2E1-low, G1E1-low, and G1E0.5-low. Each galaxy shows a similar behaviour; at some particular radii R^*, $\lambda_{\rm eq}$ decreases beyond the resolution of the simulations. We see from 6.8 and

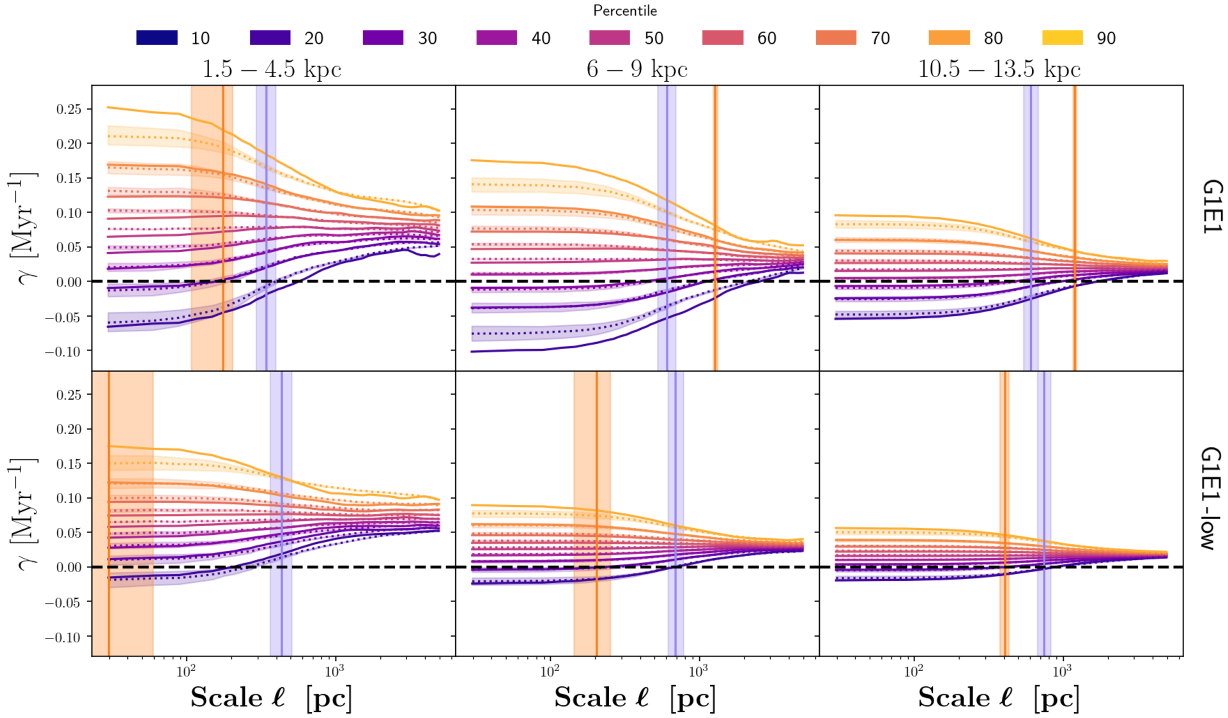

Figure 6.26: Percentiles of circulation γ within [1.5-4.5] , [6-9] and [10.5-13.5] kpc for G1E1 and G1E1-low, as a function of scale ℓ. Solid lines represent the percentiles of γ in the simulation while dashed regions represent 1σ uncertainty intervals for the model $\mathcal{V}(k)$ around the median values, showed as dotted lines. Vertical lines show the spatial scale $\lambda_c = 1/k_c$ and its corresponding uncertainty illustrated by the dashed region. Black-dashed horizontals lines show $\gamma = 0$.

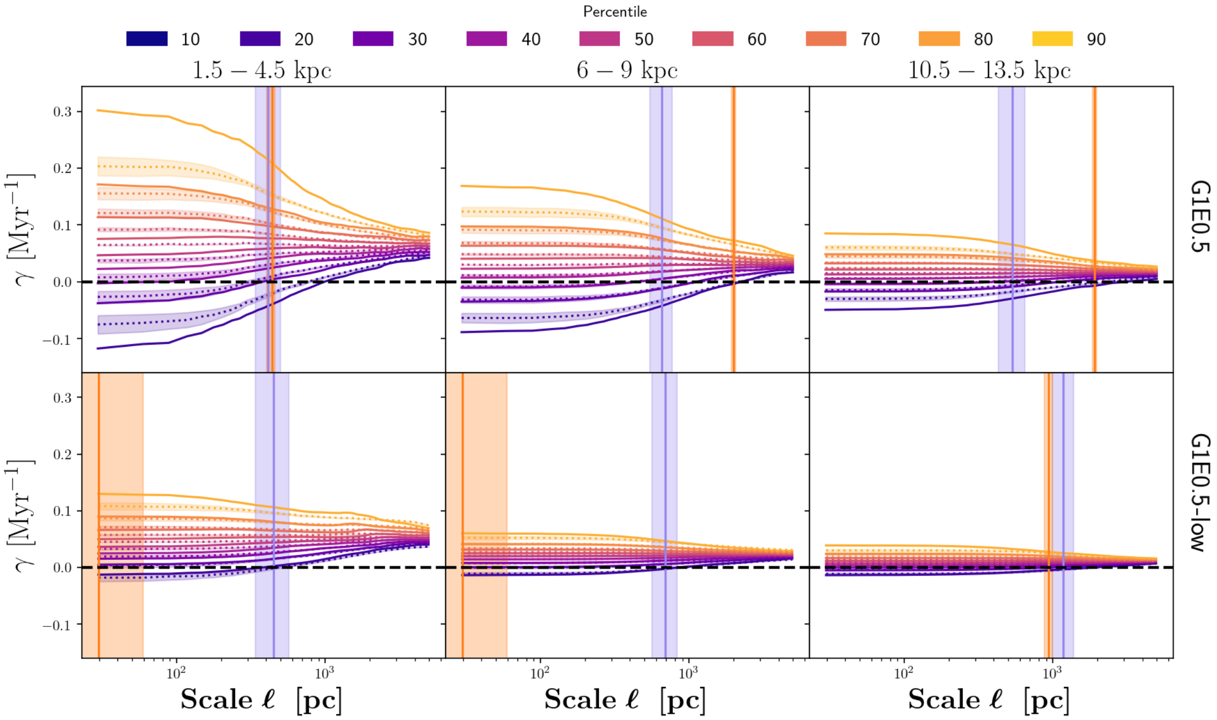

Figure 6.27: Percentiles of circulation γ within [1.5-4.5] , [6-9] and [10.5-13.5] kpc for G1E0.5 and G1E0.5-low, as a function of scale ℓ. Solid lines represent the percentiles of γ in the simulation while dashed regions represent 1σ uncertainty intervals for the model $\mathcal{V}(k)$ around the median values, showed as dotted lines. Vertical lines show the spatial scale $\lambda_c = 1/k_c$ and its corresponding uncertainty illustrated by the dashed region. Black-dashed horizontals lines show $\gamma = 0$.

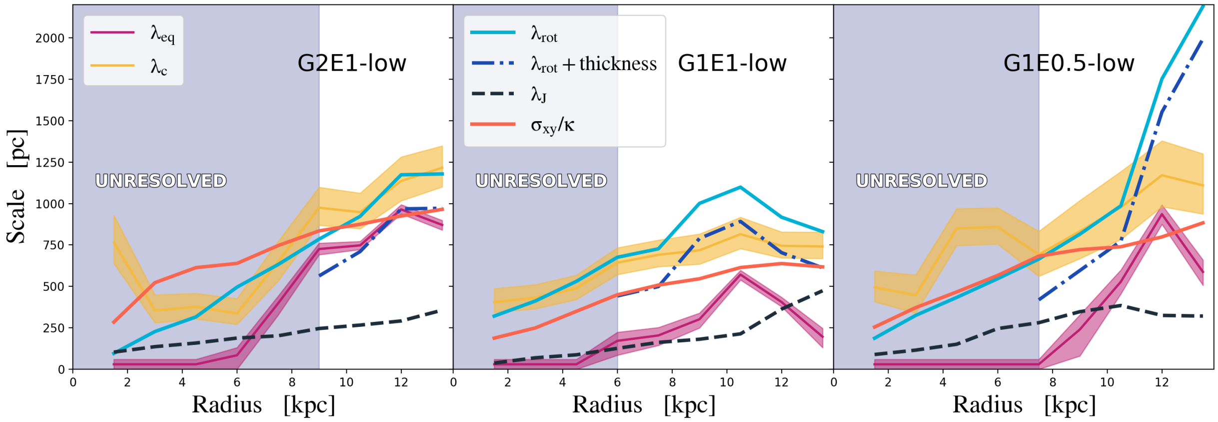

Figure 6.28: Spatial scales as a function of galactocentric radius for simulations without early stellar feedback. Solid pink and yellow lines correspond to λ_{eq} and λ_c respectively. The shaded regions correspond to 1σ uncertainties. The classical instability scales, λ_{rot} and λ_{J} are shown as a solid light-blue line and a black dashed line. The dot-dashed line shows the effects of the spatial resolution of the simulation on λ_{rot}.

6.16 that $\omega_{\rm rot}(R)$ decays exponentially while σ_0 decays somewhat linearly, which also holds for these simulations. At the center, where $\omega_{\rm rot}$ peaks, $\lambda_{\rm eq} << \Delta x$. Since $\omega_{\rm rot}$ decays faster, at some particular radius $\lambda_{\rm eq} \simeq \Delta x$, and $\lambda_{\rm eq}$ starts to be resolved.

Since these galaxies have a lower gas content at this point in time, they are more stable against gravitational collapse. In Figure 6.28 the shaded regions correspond to the regions where equation 6.14 is satisfied, and any axisymmetric perturbation is stable. The resolution of our simulations is not high enough to resolve $\lambda_{\rm rot}$. The regions where $\lambda_{\rm eq}$ is resolved overlap with the regions where $\lambda_{\rm rot}$ is resolved, once we consider the effect of the disk thickness. This shows that, $\lambda_{\rm rot}$ must be resolved in order to study $\lambda_{\rm eq}$ in simulations.

For these runs, $\lambda_{\rm eq}$ does not follow the curves of σ_{xy}/κ. On the other hand, the appear to have the same trends of $\lambda_{\rm rot}$ and λ_c at least where $\lambda_{\rm rot}$ is resolved. This could indicate that in these simulations, the major source of turbulence and non-circular motions are gravitational instabilities, whereas in our main runs non-circular motions are mainly originated from stellar feedback.

6.10. Effects of changing the model

We begin by analyzing the effects of changing our model of $\omega_{\rm rot}$. Our method to compute $\omega_{\rm rot}$, and consequently $\gamma_{\rm rot}$, is to measure a radial profile for the circular velocity field. The resulting radial profiles depends on the chosen size of the radial bins. In the main text we use the analytic function in equation 4.13 to compute $\gamma_{\rm rot}$. To test the sensitivity with respect to the chosen rotation curves, we calculate $\lambda_{\rm eq}$ for different velocity models. The simplest model corresponds to measuring the median values of the rotation curve at intervals of 500 pc. To compute the derivatives in equation 2.2 we fit a 4th order polynomial function to $\ln(v(R))$ as a function of $\ln(R)$. We show the resulting $\lambda_{\rm eq}$ as the blue line in the left panel of Figure 6.29. We see that this approach to model the rotation curve does not alter our results for $\lambda_{\rm eq}$.

We also test the effects of adding information in the azimuthal component by means of a Fourier series expansion, and include the radial component of the velocity field. The velocity field and its vorticity are given by:

$$v_\theta(R,\theta,m) = A_0 + \sum_{j=1}^{m=4} A_j\cos(j\theta) + B_j\sin(j\theta), \tag{6.16}$$

$$v_R(R,\theta,m) = C_0 + \sum_{j=1}^{m=4} C_j\cos(j\theta) + D_j\sin(j\theta), \tag{6.17}$$

$$\omega_z = \frac{1}{R}\left(\frac{\partial(Rv_\theta)}{\partial R} - \frac{\partial v_R}{\partial\theta}\right), \tag{6.18}$$

where the coefficients A_j, B_j, C_j, and D_j are functions of radius and m is the order of the expansion. We have considered terms up to the fourth order. To obtain $A_j(R)$, $B_j(R)$, $C_j(R)$, and $D_j(R)$ as functions of R we separate the disk in radial bins of constant width. We tested bin-widths of 200, 500 and 800 pc but they get almost the same results in $\lambda_{\rm eq}$. We show the

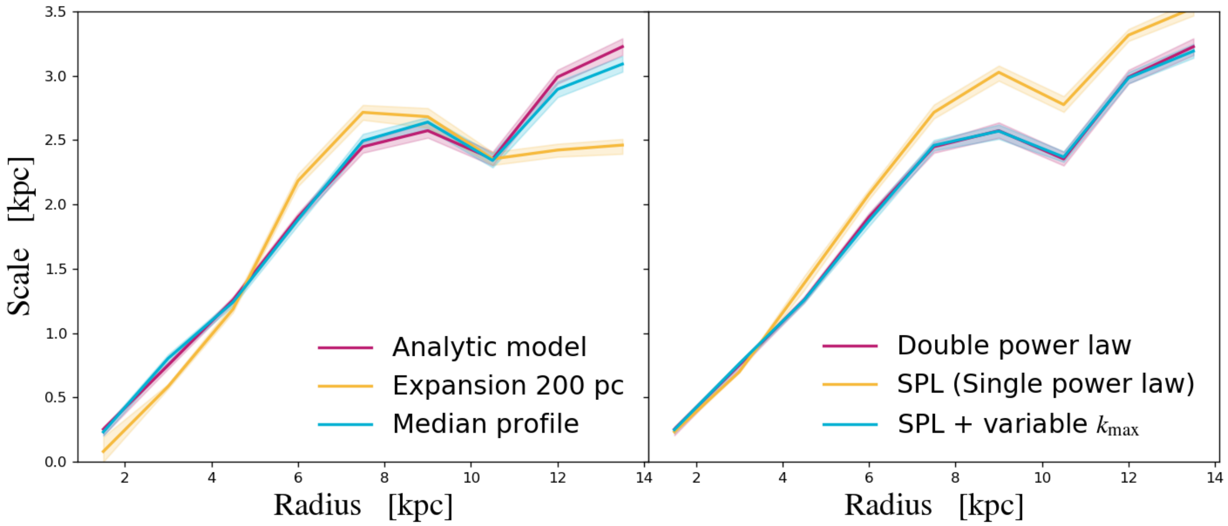

Figure 6.29: Radial profiles of λ_{eq} *Left:* Different choices of the large-scale velocity field. The magenta line shows λ_{eq} obtained in the main text with its respective 1σ uncertainties as a shaded region. The yellow line shows the resulting profile of λ_{eq} using a Fourier series expansion for the large scale velocity field with a radial bin of 200 pc. The blue line shows the results for the median rotation curve. *Right:* Different models for $\mathcal{V}(k)$. The magenta line corresponds to the model of $\mathcal{V}(k)$ used in the main text. The model with a unique power-law and fixed $k_{\max}$ is shown in yellow. The blue line corresponds to a single power-law and variable $k_{\max}$.

effect of this complex velocity field on λ_{eq} in the left panel of Figure 6.29 using a bin-width of 200 pc. We see that this choice for the model of ω_{rot} does not lead to major changes. At large galactocentric radius the estimation of λ_{eq} is a bit lower.

6.11. Different models for the random velocity field

Now we test how different models for $\mathcal{V}(k)$ change the resulting curves of λ_{eq}. For our model, the spatial scale λ_{eq}, at which large scale motions and non-circular motions contribute equally to the circulation of gas, depends on the function $\mathcal{V}(k)$. The first model of $\mathcal{V}(k)$ consist on a power law ($n_1 = n_2$), and the wavenumber k is bounded between the values $k_{\min} = 4/L$ and $k_{\max} = 1/4\Delta x$. The second model also consist on a single power law but allowing $k_{\max}$ to vary. We show these models in the right panel of Figure 6.29. We can see that the fiducial model used for $\mathcal{V}(k)$ shows similar results for λ_{eq} if we use a single power law with a variable $k_{\max}$. However, if we fix $k_{\max} = 1/4\Delta x$ the values of λ_{eq} are higher.

6.12. Limitations and Caveats

The work presented here is largely exploratory and aimed at establishing the basic concepts associated with modeling the spatially dependent distribution of gas circulation in disk galaxies. Here we discuss some of the limitations associated with this modeling. In a future work we expect to address several of these limitations in order to apply the presented methods to extract information from observed galaxy velocity fields.

6.12.1. Velocity model

The main assumption in our model is that the velocity field in the plane of the disk can be approximated by the contribution of two different fields: $\vec{V} = \vec{V}_{\mathrm{rot}} + \vec{V}_{\mathrm{nc}}$, where $\vec{V}_{\mathrm{rot}}$ corresponds to the galactic velocity curve and $\vec{V}_{\mathrm{nc}}$ to a Gaussian random velocity field. In real galaxies, we find other types of coherent motions which are different from galactic rotation and pure random motions. Among these, we find induced motions by galactic bars and spirals, and epicyclic motions. At the scale of epicycles, gas is still affected by the tidal forces exerted by the galactic potential (Meidt et al. 2018). According to Meidt et al. (2018), depending on the strength of self-gravity, the dynamical structure of clouds show preferred orientations in radial or azimuthal coordinates, which does not occur in our model of V_{nc}. In addition, galactic bars and spirals would also produce deviations from global galactic rotation which we are implicitly including in $\vec{V}_{\mathrm{nc}}$.

Figure 6.17 shows that our simple model can successfully fit the distribution of circulation across different spatial scales in general terms but there are some clear deviations in particular regimes (e.g., small scale, prograde rotating regions with high values of γ at intermediate galactocentric radii) which probably signal more complex types of motions not recovered by the model. Moreover, due to conservation of angular momentum, the vorticity in high density regions is enhanced. It is unclear how to statistically model these type of motions.

6.12.2. Full velocity field

In this work we have made use of isolated galaxy simulations whose rotation axis is aligned with the z-axis of the simulation box by default. To compute the circulation we use the two-dimensional velocity field $\vec{V}(x, y)$, the density weighted projection across the z-axis of the three-dimensional velocity field. We can separate the total circulation into two terms Γ_x and Γ_y:

$$\Gamma = \oint \vec{v} \cdot \mathrm{d}\vec{r} = \oint v_x \cdot \mathrm{d}x + v_y \cdot \mathrm{d}y = \Gamma_x + \Gamma_y \tag{6.19}$$

where x and y are coordinates on the plane of the disk. In observations we only have access to the velocity along the line of sight, which will be the sum of one of the velocities in the plane of the galaxy, v_x or v_y, and v_z, motions vertical to the disk midplane. Consider a disk with inclination i such that the line of sight lies in the x-z plane. The coordinates in the plane of the sky are $z' = z \sin i + x \cos i$ and $y' = y$. The axis of the line of sight is $x' = x \sin i + z \cos i$ and the velocity is $v_{\mathrm{LOS}} = v'_x = v_x \sin i + v_z \cos i$. On the midplane $z = 0$ and the projected position $z' = x \cos i$. From the observed quantities we can compute

$$\begin{aligned} \Gamma' &= \oint v_{\mathrm{LOS}} \mathrm{d}z' = \sin i \cos i \oint v_x \mathrm{d}x + \cos^2 i \oint v_z \mathrm{d}x \\ \Gamma' &= \sin i \cos i \Gamma_x + \cos^2 i K_{xz} \end{aligned} \tag{6.20}$$

where Γ_x is the component of Γ in the x-axis and K_{xz} is the sum of vertical motions along the x-axis. The term K_{xz} should be of the order of $\langle v_z \rangle \ell$. This component has to be treated as an additional term in the assumed decomposition of the velocity field. In this work we have assumed that the velocity field in the plane is the sum of galactic rotation plus a random component. For v_x this means $v_x = -\Omega y + \delta v_x$, where Ω is the galactic angular velocity and δv_x is the random velocity term. For v_z we can assume that $v_z = \delta v_z$. Then $\Gamma' \approx -\cos i [y \sin i \oint \Omega \mathrm{d}x + \ell(\langle v_x \rangle \sin i - \langle v_z \rangle \cos i)]$ At large scales $\langle v_x \rangle$ and $\langle v_z \rangle$ are approximately zero while at small scales both terms behave like random variables. The sum of these two terms would be the observed random component. Since we want to compare them with galactic rotation, the best inclination has to maximize the contribution of Ω to Γ' which occurs at $i = 45°$.

6.12.3. Surface brightness limits and recovery of velocity information

A major limitation comes from the observational detection limits for different transition lines which lead to an incomplete sampling of the velocity field. For example, the CO (1-0) transition has a critical density $\simeq 10^3 \mathrm{cm}^{-3}$, tracing the distribution of molecular gas in galaxies. This implies that we can only observe a small fraction of the velocity field at the scales of molecular clouds. Proper ways of dealing with noise and censored data in faint regions will also need to be implemented.

6.12.4. Simulations

In this paper we use hydrodynamical simulations of disk galaxies to test our method. The results presented here are valid to our set of simulations, with their defined prescriptions for star formation and stellar feedback. However, caution should be taken before directly extrapolating our findings to the environments of real galaxies. Here we list what we consider are the most important aspects at which our simulations and observed galaxies differ.

- Resolution: The maximum spatial resolution corresponds to 30 pc. In practice this means that we are able to resolve structures and instabilities of the order of 100 pc, corresponding to approximately four times our resolution. In nearby galaxies, the size of molecular clouds typically ranges from tens to hundreds of parsecs. Although we see formation of structures, this resolution is not enough to resolve the inner turbulence of molecular clouds, their gravitational collapse, and the interactions of clouds smaller than 100 pc. A higher resolution would imply more interactions and a higher velocity dispersion at the smallest scales studied here. Then, we might expect a change in the values of n_2 which sets the behavior of $\mathcal{V}(k)$ at large wavenumber k, i.e. at smaller spatial scales. Despite this caveat, $\lambda_{\rm eq}$ and λ_c are well resolved almost everywhere.

- Temperature: Gas is allowed to cool due to radiation down to a temperature of 300 K. This means that the smallest structures in our simulations are more similar to HI clouds. Also, this temperature floor sets a minimum Jeans scale as a function of gas surface density
$$\lambda_{J,\rm min} = \frac{5}{3}\frac{k_B T_{\rm min}}{\mu m_p}\frac{1}{G\Sigma_{\rm gas}} = 133{\rm pc}\left(\frac{\Sigma_{\rm gas}}{10{\rm M_\odot pc^{-2}}}\right)^{-1}, \quad (6.21)$$
assuming a mean molecular weight $\mu = 0.6$, according to the cooling curve of Rosen & Bregman (1995) that assumes a fully ionized disk. In local galaxies, the Jeans length is of the order of a few pc, about two orders of magnitude below the average Jeans scales found in our simulations. The temperature floor leads to an overestimation of the relevance of the Jeans scale. It is important to mention that to compute the radial profiles of $\lambda_{\rm J}$ showed here, we are considering all the gas in an annulus and its respective average temperature instead of the average $\lambda_{\rm J}$ for cold and dense gas. This makes sense for our analysis since we are computing the circulation for all the gas within the physical volume described in the paper. However, for regions with densities below $10{\rm M_\odot pc^{-2}}$ the minimum value for $\lambda_{\rm J}$ is larger than four resolution elements. Then, even for our resolution the values of $\lambda_{\rm J}$ are likely overestimated and should be considered as upper limits.
- Stellar feedback: In our recipe of stellar feedback, we include the direct injection of momentum from radiation pressure and stellar winds to the six nearest cells. Although the amount of added momentum $\vec{p}_\star$ does not explicitly change with spatial resolution, the typical masses, $m_{\rm cell}$, of cells around star particles do change with different spatial resolution. This translates in different magnitudes for the change of the velocity field around star particles, since the velocity $\vec{v}_\star = \vec{p}_\star/m_{\rm cell}$. We have not tested how sensitive to resolution is this feedback prescription.
- Spiral arms and bars : A relevant difference between observations, other simulations and our runs is that our simulated galaxies lack grand design spiral arms. The main difference is that the old stellar population in this work is represented by an external axisymmetric potential, whereas other studies use particles (Renaud et al. 2013) or spiral potentials (Dobbs et al. 2015). Only new stars are particles, hence only this stellar component can respond to perturbations making the stellar disk more stable. The impact of spiral arms and bars in our analysis can be separated by their effect on large and small scales. At large scales, the bulk motion $v_{\rm rot}$ must be a function of radius, and the azimuthal angle. At small scales, spiral and bars can induce vortex motions by Kelvin-Helmholtz, Rayleigh-Taylor instabilities or tidal fields (Dobbs & Bonnell 2006; Renaud et al. 2013). These structures create new sources of turbulence, therefore the velocity field at the scale of molecular clouds has different properties. In this work, we have divided disk galaxies in annular regions and measured radial profiles of the parameters that define the small scale velocity field $v_{\rm nc}$. To test the effect of spirals and arms we also need to separate regions according to their azimuthal distance to these structures.

Conclusions

In this thesis we have characterized the rotation of gas in galaxies at different scales by measuring the circulation Γ, a macroscopic measure of fluid rotation. We choose to measure this quantity since it let us compute the local degree of rotation for patches of gas of arbitrary size and shape. The circulation of a fluid also has the advantage that at small scales its distribution is given by the dynamics at small scales, while at large scales the behavior at small scales gets erased from the distribution of Γ, and it is dominated by large scale motions instead. This motivated us to develop a method to measure the contributions of large-scale motions, i.e. galactic rotation, and non-circular motions in the observed distribution of circulation at different spatial scales. Non-circular motions are modeled as Gaussian random velocity fields (GRF), described by a generating function in Fourier space $\mathcal{V}(k)$. We characterize how the parameters of GRFs give rise to velocity fields with different properties, and how the final distribution of Γ changes with these parameters. We also developed the mathematical formulation and algorithm to be applied in discrete velocity fields, that let us recover the parameters of the GRF. We use a Bayesian approach to recover the parameter distributions of the GRFs. Once we get these distribution we can show quantitatively down to what scales galactic rotation is still relevant. We apply this method on three hydrodynamical simulations of galactic disks, performed with the AMR code Enzo (Bryan et al. 2014) that includes star formation, supernova feedback, momentum feedback from stellar winds, and HII regions, and with a spatial resolution of 30 pc. For the stellar feedback recipes we implement analytic approximations to the tabulated results of STARBURST99 (Leitherer et al. 1999). Our simulations show star formation rates consistent with normal galaxies. We also run three additional simulations with only supernova feedback.

We summarize the major points of this work:

- We model the velocity field of galaxies with two components: a galactic component given by the circular velocity profile and a Gaussian random component. The random component is obtained from a function $\mathcal{V}(k)$ which functional form correspond to a broken power-law with exponents n_1, and n_2, transitioning at the wavenumber $k = k_c$. The amplitude of $\mathcal{V}(k)$ is defined by the characteristic velocity dispersion of the random field σ_0. We apply the model to hydrodynamical simulations and confirm that motions can be well modeled by two components with different circulation, as hypothesized. The model successfully reproduces the distribution of circulation as a function of scale, except when regions are under gravitational collapse.
- We find that a sharp transition in the behaviour of gas dynamics at the scale $\lambda_c = 1/k_c$ is necessary to fit the circulation distribution. This may correspond to the scale at which

kinematics transition from being coupled to the galaxy to more disordered motion, associated with feedback-driven turbulence or gravity-driven turbulence. However, the resolution of the current simulations limits our ability to probe this in greater detail.

- The scale λ_c is similar to the scale at which gas fragments, and to the epicyclic scale σ_z/κ that defines the scale at which self-gravity and the potential of the galaxy are equally important to determine the internal dynamics of clouds. The scale λ_c is also similar to the scale of fragmentation and the distance between clumps suggesting that λ_c shows the formation of structure in the density field.
- We introduce a dynamical spatial scale $\lambda_{\rm eq}$. At spatial scales similar to $\lambda_{\rm eq}$ the contributions of galactic circular motions and non-circular motions to the observed circulation or local rotation of gas are roughly the same. For regions larger than $\lambda_{\rm eq}$ galactic rotation dominates the circulation of gas and consequently the measured rotation. At these scales the distribution of circulation shows largely positive values which means that gas rotates in the same orientation of the galaxy. For patches of gas smaller than $\lambda_{\rm eq}$, non-circular and random motions start to dominate the observed circulation and retrograde rotating regions can be found.
- We find that $\lambda_{\rm eq}$ depends on the local properties of gas. From the center of the galaxies, $\lambda_{\rm eq}$ increases with galactocentric radius. This shows that the spatial scale at which gas dynamics is dominated by non-circular motions depends on the position in the galactic disk. We see different behaviors in the central regions and outskirts of galaxies. Galactic rotation shows to be more important or dominant towards the center of galactic disks.
- The scale $\lambda_{\rm eq}$ is similar to the ratio σ_{xy}/κ, as predicted by models about balance of rotation and turbulence, where σ_{xy} is the in-plane velocity dispersion of the two dimensional velocity field within a radial annulus and κ is the epicyclic frequency. However, when suppressing momentum-feedback in simulations, $\lambda_{\rm eq}$ can be lower than σ_{xy}/κ, and its radial profile might be correlated with the spatial scales of gravitational instabilities since self-gravity becomes a relevant source of turbulence.
- In some regions $\lambda_{\rm eq}$ is greater than $\lambda_{\rm rot}$. The formation of structures in such regions will be dominated by non-circular motions. Depending on the sources of feedback, turbulence, and local dynamics $\lambda_{\rm eq}$ can be larger or smaller than $\lambda_{\rm rot}$. Particularly, for strong modes of stellar feedback $\lambda_{\rm eq}$ can be larger than $\lambda_{\rm rot}$.
- Stellar feedback changes $\lambda_{\rm eq}$ by injecting momentum at smaller scales, increaing motions that do not follow galactic rotation. Different prescriptions of stellar feedback will produce different velocity fields that show different coupling between the dynamics of gas at small scales and the large scale galactic rotation. This can also produce changes in the coupling between star formation and galactic rotation.

This work shows that the characterization of the ISM circulation, from the modeling of velocity fields of galaxies, opens the possibility of directly measure scales associated with gravitational collapse and structure formation, and to study how these scales change with galactic environment. It also shows that rotation is dynamically important in some environments like the centers of galactic disks. However, there are many differences between our simulated galaxies and real ones that have to be addressed before extrapolating our results. For example, our resolution of 30 pc does not allow us to resolve the inner turbulence of molecular clouds, and with our temperature floor of 300 K we are unable to model molecular clouds and their interactions. Additionally, we have found that the gravitational collapse of gas clouds is not included in the characterization of the velocity fields, that our simulations show to be an important feature at the smallest scales. Additionally, for real galaxies we have to consider the effect of structures such as spiral arms or bars. On the other hand, interesting aspects may appear by measuring the circulation in observations. For example, future telescopes like the Square Kilometer Array will allow us to measure full velocity maps of HI and test this method without the problems that tracers of molecular gas show.

Bibliography

Agertz, O., Kravtsov, A. V., Leitner, S. N., & Gnedin, N. Y. 2013, ApJ, 770, 25

Binney, J., & Tremaine, S. 2008, Galactic Dynamics: Second Edition (Princeton University Press)

Bournaud, F., Elmegreen, B. G., Teyssier, R., Block, D. L., & Puerari, I. 2010, MNRAS, 409, 1088

Braine, J., Rosolowsky, E., Gratier, P., Corbelli, E., & Schuster, K. F. 2018, A&A, 612, A51

Bryan, G. L., Norman, M. L., O'Shea, B. W., et al. 2014, ApJS, 211, 19

Caldú-Primo, A., & Schruba, A. 2016, AJ, 151, 34

Cen, R., & Ostriker, J. P. 1992, ApJL, 399, L113

Colombo, D., Hughes, A., Schinnerer, E., et al. 2014, ApJ, 784, 3

Combes, F., Boquien, M., Kramer, C., et al. 2012, A&A, 539, A67

Courteau, S. 1997, AJ, 114, 2402

Couston, L.-A., Lecoanet, D., Favier, B., & Le Bars, M. 2019, arXiv e-prints, arXiv:1909.03244

Daddi, E., Elbaz, D., Walter, F., et al. 2010, ApJL, 714, L118

Dobbs, C. L., & Bonnell, I. A. 2006, MNRAS, 367, 873

Dobbs, C. L., & Pringle, J. E. 2013, MNRAS, 432, 653

Dobbs, C. L., Pringle, J. E., & Duarte-Cabral, A. 2015, MNRAS, 446, 3608

Druard, C., Braine, J., Schuster, K. F., et al. 2014, A&A, 567, A118

Elmegreen, B. G. 1997, in RMxAC, Vol. 6, Revista Mexicana de Astronomia y Astrofisica Conference Series, ed. J. Franco, R. Terlevich, & A. Serrano, 165

Elmegreen, B. G., & Scalo, J. 2004, ARA&A, 42, 211

Escala, A. 2015, ApJ, 804, 54

Escala, A., & Larson, R. B. 2008, ApJL, 685, L31

Freedman, D., & Diaconis, P. 1981, Wahrscheinlichkeitstheorie verw Gebiete, 57: 453

Girichidis, P., Walch, S., Naab, T., et al. 2016, MNRAS, 456, 3432

Goldbaum, N. J., Krumholz, M. R., & Forbes, J. C. 2015, ApJ, 814, 131

Goldbaum, N. J., Krumholz, M. R., & Forbes, J. C. 2016, ApJ, 827, 28

Heyer, M., Krawczyk, C., Duval, J., & Jackson, J. M. 2009, ApJ, 699, 1092

Hopkins, P. F., & Grudić, M. Y. 2019, MNRAS, 483, 4187

Hopkins, P. F., Kereš, D., Oñorbe, J., et al. 2014, MNRAS, 445, 581

Jeffreson, S. M. R., & Kruijssen, J. M. D. 2018, MNRAS, 476, 3688

Kafle, P. R., Sharma, S., Lewis, G. F., & Bland-Hawthorn, J. 2014, ApJ, 794, 59

Kannan, R., Marinacci, F., Simpson, C. M., Glover, S. C. O., & Hernquist, L. 2020, MNRAS, 491, 2088

Kennicutt, Jr., R. C. 1989, ApJ, 344, 685

Kennicutt, Jr., R. C. 1998, ApJ, 498, 541

Koch, E. W., Chiang, I. D., Utomo, D., et al. 2020, MNRAS, 492, 2663

Koch, E. W., Rosolowsky, E. W., Lockman, F. J., et al. 2018, MNRAS, 479, 2505

Koda, J., Sawada, T., Hasegawa, T., & Scoville, N. Z. 2006, ApJ, 638, 191

Kraichnan, R. H. 1967, Physics of Fluids, 10, 1417

Kritsuk, A. G., Lee, C. T., & Norman, M. L. 2013, MNRAS, 436, 3247

Kruijssen, J. M. D., Dale, J. E., Longmore, S. N., et al. 2019, MNRAS, 484, 5734

Krumholz, M., & Burkert, A. 2010, ApJ, 724, 895

Krumholz, M. R., Burkhart, B., Forbes, J. C., & Crocker, R. M. 2018, MNRAS, 477, 2716

Krumholz, M. R., Dekel, A., & McKee, C. F. 2012, ApJ, 745, 69

Lang, A., & Potthoff, J. 2011, arXiv e-prints, arXiv:1105.2737

Larson, R. B. 1981, MNRAS, 194, 809

Leitherer, C., Schaerer, D., Goldader, J. D., et al. 1999, ApJS, 123, 3

Leroy, A. K., Schinnerer, E., Hughes, A., et al. 2017, ApJ, 846, 71

Li, Y., Mac Low, M.-M., & Klessen, R. S. 2005, ApJL, 620, L19

Marinacci, F., Sales, L. V., Vogelsberger, M., Torrey, P., & Springel, V. 2019, MNRAS, 489, 4233

Matzner, C. D. 2002, ApJ, 566, 302

Meidt, S. E., Leroy, A. K., Rosolowsky, E., et al. 2018, ApJ, 854, 100

Miyamoto, M., & Nagai, R. 1975, PASJ, 27, 533

Mogotsi, K. M., de Blok, W. J. G., Caldú-Primo, A., et al. 2016, AJ, 151, 15

Murray, N., Quataert, E., & Thompson, T. A. 2010, ApJ, 709, 191

Musacchio, S., & Boffetta, G. 2017, Physics of Fluids, 29, 111106

Navarro, J. F., Frenk, C. S., & White, S. D. M. 1997, ApJ, 490, 493

Padoan, P., Haugbølle, T., & Nordlund, Å. 2012, ApJL, 759, L27

Padoan, P., Haugbølle, T., Nordlund, Å., & Frimann, S. 2017, ApJ, 840, 48

Paret, J., & Tabeling, P. 1998, Physics of Fluids, 10, 3126

Pedlosky, J. 1992, Geophysical Fluid Dynamics, Springer study edition (Springer New York)

Plummer, H. C. 1911, MNRAS, 71, 460

Pranav, P., van de Weygaert, R., Vegter, G., et al. 2019, MNRAS, 485, 4167

Renaud, F., Bournaud, F., Emsellem, E., et al. 2013, MNRAS, 436, 1836

Romeo, A. B., Burkert, A., & Agertz, O. 2010, MNRAS, 407, 1223

Romeo, A. B., & Falstad, N. 2013, MNRAS, 433, 1389

Romeo, A. B., & Mogotsi, K. M. 2017, MNRAS, 469, 286

Rosen, A., & Bregman, J. N. 1995, ApJ, 440, 634

Rosolowsky, E. 2005, PASP, 117, 1403

Rosolowsky, E. 2007, ApJ, 654, 240

Rosolowsky, E., Engargiola, G., Plambeck, R., & Blitz, L. 2003, ApJ, 599, 258

Ruppert-Felsot, J. E., Praud, O., Sharon, E., & Swinney, H. L. 2005, PhRvE, 72, 016311

Sarazin, C. L., & White, III, R. E. 1987, ApJ, 320, 32

Schruba, A., Kruijssen, J. M. D., & Leroy, A. K. 2019, arXiv e-prints, arXiv:1908.04306

Semenov, V. A., Kravtsov, A. V., & Gnedin, N. Y. 2016, ApJ, 826, 200

Shetty, R., Beaumont, C. N., Burton, M. G., Kelly, B. C., & Klessen, R. S. 2012, MNRAS, 425, 720

Silk, J. 1997, ApJ, 481, 703

Stinson, G. S., Brook, C., Macciò, A. V., et al. 2013, MNRAS, 428, 129

Sun, J., Leroy, A. K., Schruba, A., et al. 2018, ApJ, 860, 172

Tan, J. C. 2000, ApJ, 536, 173

Tasker, E. J., & Tan, J. C. 2009, ApJ, 700, 358

Toomre, A. 1963, ApJ, 138, 385

Toomre, A. 1964, ApJ, 139, 1217

Truelove, J. K., Klein, R. I., McKee, C. F., et al. 1998, ApJ, 495, 821

Truelove, J. K., Klein, R. I., McKee, C. F., et al. 1997, ApJL, 489, L179

Utreras, J., Becerra, F., & Escala, A. 2016, ApJ, 833, 13

Walch, S. K., Whitworth, A. P., Bisbas, T., Wünsch, R., & Hubber, D. 2012, MNRAS, 427, 625

Ward, R. L., Benincasa, S. M., Wadsley, J., Sills, A., & Couchman, H. M. P. 2016, MNRAS, 455, 920